Structural Characterization Studies on Semiconducting $ZnSnN_2$ Films using Synchrotron X-ray Diffraction

by

Nancy Senabulya

A dissertation submitted in partial fulfillment
of the requirements for the degree of
Doctor of Philosophy
(Applied Physics)
in The University of Michigan
2017

Doctoral Committee:
Professor Roy Clarke, Chair
Professor Steven M. Durbin
Assistant Professor Emmanouil Kioupakis
Professor Cagliyan Kurdak

nsenab@umich.edu
ORCID ID: 0000-0002-3394-5452

To Andrew, Jordan and Elise

ACKNOWLEDGEMENTS

I would like to thank my mom who sacrificed everything for my siblings and I to get the best education in Uganda. For some reason, she always believed I would get a PhD and I never believed her until now. Her love and support helping me look after our kids in the first six months of their lives, when I had them in graduate school is the reason I could complete this PhD in record time. My sister and friend Donna has been an important source of inspiration for me since childhood. Her passion for Math and Science and subsequent successful career in Telecommunications Engineering have allowed me to dream beyond my wildest dreams the things I could accomplish as a woman from a developing country. Thank you, Donna, for not allowing to be limited by circumstances. You worked hard and set a good example for all of us to follow. I am proud to be your sister. Diana, Ivan, Penny, Jenna, Martin, I love you guys so much. Thanks for rooting for me throughout this whole process, I have enjoyed our conversations on skype and been so proud of all you have accomplished the last few years.

I am indebted to my husband Andrew who has been so loving and a huge source of emotional support for me throughout this PhD. Thank you for watching the kids while I spent whole weeks out of town doing synchrotron experiments in Illinois and for being my biggest cheerleader on this journey. I would not have done this without your love, sense of humor and unwavering support.

My deepest thanks go to my advisor, Professor Roy Clarke. He is one of the best decisions I made in graduate school. His scientific knowledge and insight have been great sources for steering me in the right directions in my early research career, and he has strongly encouraged any research plans and ideas I came up with, providing firm support for every project I have participated in. Especially, whenever we encountered challenging situations during research, he has willingly and enthusiastically approached the issues. His passion helped me successfully overcome any hardships I faced, and I hope to follow his passion in the future.

I am also indebted to Dr. Christian Schlepütz and Dr. Yongsoo Yang for their strong support and help. They both provided tremendous guidance when I had just started my synchrotron x-ray diffraction studies and have continuously supported me as a beamline scientist at the synchrotron. All my technical skills and knowledge in crystallography and x-ray diffraction came from their guidance. Dr. Christian Schlepütz also generously provided all the data analysis tools he developed.

Collaborations with Professor Steven Durbin's and his group members, Nathaniel Feldberg, Robert Makin and Brian Durant have been a very enjoyable experience. They have worked tirelessly to grow the best samples for me to analyze and I have obtained invaluable new knowledge, skills and experiences during this collaboration. I also appreciate Professor Durbin for all the guidance he provided as a dissertation committee member.

I also thank Professor Cagliyan Kurdak and Professor Emmanouil Kioupakis for their insight and suggestions for this dissertation.

I appreciate my friends and colleagues Christina Jones, Heather Ferguson and James Mathis. Thank you, Christina, for sacrificing your time to go to Argonne with me so I could have help during the long hours at the beam time. Heather, we have been together since that dreadful first class in quantum mechanics. I am grateful to have had you by my side walking this rather challenging journey of graduate school and I appreciate your friendship very much. James, you are a calming presence in the office. I like that you don't panic under pressure and are a very humble person and such a good source of godly wisdom.

I am thankful for my friend Annie who I have only known for three years but it already feels like a lifetime. Thank you for watching Jordan when both Andrew and I have been out of town for work and for checking on me when Andrew was out of town to put Jordan to bed so I could have some down time or extra work time. I appreciate your friendship very much.

I am very grateful to my H20 church family that made Ann Arbor feel like home. You made me and my family feel safe in this foreign land and provided so much love and support to us. Cindy Fellows has been a dear friend and mentor and I am very thankful for her friendship and godly wisdom. The women in my small group; Furaha, Melissa, Joyce Lee, Kaitlin, Akima, Nee, Tricia, Joyce Gong and Lilo. It has been so much fun hanging out with you. I value your friendship.

I appreciate the excellent beam line support from the beamline staff at Argonne National Laboratory: Dr. Peter Eng and Dr. Joanne Stubbs (APS 13-BM-C), Dr. Christian Schlepütz, Dr. Zhan Zhang, Evguenia Karapetrova (APS 33-BM-C, 33-ID-D). All the data presented in this dissertation were obtained through their unrivaled support.

I am also very thankful for Cynthia McNabb the Applied Physics administrator and Lauren Segall and Charles Sutton who have been the applied physics coordinators during my PhD. Your support for all the students in the program is unparalleled and you are the reason we keep going when it gets hard. Thank you for your open-door policy that has made it easier for me to navigate the bureaucracies of the University institution.

The REFRESCH project which is part of the Third Century Initiative at the University of Michigan has been a huge source of financial support for me over the past three years and I am very grateful for the opportunity to have worked with all the talented people on this project. I am very grateful to Brenda Vyletel the project manager of REFRESCH for all her unwavering support.

This work was supported in part by the National Science Foundation Grant No. DMR-1410915

(Program Manager Charles Ying) and at UM by NSF Grant No. DMR 10006835. The DFT calculations were supported by the National Science Foundation CAREER award through Grant No.DMR-1254314. I acknowledge and greatly appreciate funding from the Schlumberger Faculty for the Future Grant. I also thank Dr. Vladimir Stoica for thoughtful discussions and help with experiments at APS. C. Jones acknowledges support by the National Science Foundation Graduate Research Fellowship Program through Grant No. DGE-1256260. X-ray diffraction experiments were performed at sectors 13-BMC (GeoSoilEnviroCARS), 33-IDD (XSD), and 33-BMC (XSD) at the APS. GeoSoilEnviroCARS is supported by the National Science Foundation - Earth Sciences (EAR-0622171) and Department of Energy – Geosciences (DE-FG02-94ER14466). The use of the APS was supported by the U.S. Department of Energy, Office of Science, Office of Basic Energy Sciences, under Contract No. DE-AC02-06CH11357. This research used resources of the National Energy Research Scientific Computing Center, a DOE Office of Science User Facility supported by the Office of Science of the U.S. Department of Energy under Contract No. DE-AC02-05CH11231.

TABLE OF CONTENTS

CHAPTER

LIST OF FIGURES

LIST OF TABLES

LIST OF ABBREVIATIONS

ZSN	Zinc Tin Nitride
LGO	Lithium Gallate
YSZ	Yttria stabilized zirconia
TEM	Transmission Electron Microscopy
LEDs	Light Emitting Diodes
MOCVD	Metal Organic Chemical Vapor Deposition
PAMBE	Plasma Assisted Molecular Beam Epitaxy
LDA	Local Density Approximation
GGA	Generalized Gradient Approximation
HTCs	Heterovalent Ternary Compounds
DFT	Density Functional Theory
APS	Advanced Photon Source
ANL	Argonne National Laboratory
3D-RSMs	Three-Dimensional Reciprocal Space Maps
RHEED	Reflection High-Energy Electron Diffraction
XRD	X-ray Diffraction
RTA	Rapid Thermal Annealing
ID	Insertion Device
BM	Bending Magnet
RF	Radio Frequency
VASP	Vienna Ab Initio Simulation Package
PBE	Perdew-Burke-Exchange
VLS	Vapor Liquid Solid synthesis

ABSTRACT

This work is motivated by the need for new visible frequency direct bandgap semiconductor materials that are earth abundant and low-cost to meet the increasing demand for optoelectronic device applications such as solid state lighting and photovoltaics. Zinc-Tin-Nitride ($ZnSnN_2$), a member of the II-IV nitride semiconductor family has been proposed as an alternative to the more common III-nitride semiconductors for use in optoelectronic devices. This material has been synthesized under optimized conditions using plasma assisted molecular beam epitaxy. Though a lot of research has recently been done computationally to predict the electronic and structural properties of $ZnSnN_2$, experimental verification of these theories in single crystal thin films is lacking and warrants investigation because the accurate determination of the crystal structure of $ZnSnN_2$ is a fundamental prerequisite for controlling and optimizing optoelectronic properties. In this synchrotron x-ray diffraction study, we present experimental validation, through unit cell refinement and 3d reciprocal space maps, of the crystal structure of single domain $ZnSnN_2$ films deposited on (111) Yttria stabilized zirconia (YSZ) and (001) Lithium gallate (LGO) substrates. We find that $ZnSnN_2$ films grown on (111) YSZ can attain both the theoretically predicted disordered wurtzite and ordered orthorhombic $Pna2_1$ structures under carefully controlled MBE growth conditions, while films grown on (001) LGO have the ordered $Pn2_1a$ orthorhombic crystal structure. Through a systematic annealing study, a temperature induced first order structural phase transition from the wurtzite to orthorhombic phase is realized, characterized by the appearance of superstructure reflections in θ-2θ measurements. This structural phase transition is directly correlated with the transition from a disordered cation sublattice to an ordered lattice and is

consequential for tuning the disorder dependent bandgap of $ZnSnN_2$ from 1eV to 1.8eV in disordered wurtzite and ordered orthorhombic films respectively, hence obviating the need for traditional alloying techniques commonly used to tune the opto-electronic properties in semiconductors. This thesis lays the groundwork for understanding the relationship between the structural properties of $ZnSnN_2$ and the heterovalent cation ordering in this semiconducting compound, and provides the first reported study of single crystal $ZnSnN_2$ films exhibiting the ordered orthorhombic crystal structure. This structure, obtained using heteroepitaxy, is a consequence of close coordination between MBE growth conditions and detailed x-ray characterization. The work described in this thesis shows that with improvements in material quality and further research into the electrical and optical properties, $ZnSnN_2$ has the potential to facilitate the production of cost-effective and scalable optoelectronic devices.

CHAPTER I

Introduction

1.1 X-ray Diffraction

X-rays were discovered in 1895 by Wilhelm Conrad Roentgen (1845-1923) who was a Professor at Wűrzburg University in Germany. [1,2] Working with a cathode-ray tube in his laboratory, Roentgen observed a fluorescent glow on a paper plate about two meters from the discharge tube. The tube that Roentgen was working with consisted of glass with positive and negative electrodes encapsulated in it. The air in the tube was evacuated, and when a high voltage was applied, the tube produced a fluorescent glow. Roentgen shielded the tube with heavy black paper, and discovered a green colored fluorescent light generated by a material located a few feet away from the tube. He concluded that the discharge must be emitting a form of invisible radiation that could pass through the glass and the surrounding black paper. Roentgen called this invisible radiation x-rays. [3] One of Roentgen's first experiments late in 1895 was a film of the hand of his wife, Bertha shown in Figure 1.1 which illustrated that x-rays could be used to investigate the internal structure of an object. [1,2] It is now well known that x-rays are electromagnetic radiation with short wavelength ranging from 0.1 to 100 Å. This very short wavelength makes it possible for x-rays to penetrate objects that visible light cannot. Since their discovery, x-rays have been used in diverse fields such as chemistry and biology to study proteins, medicine for medical imaging applications, physics and materials science to study the crystal structure of films, in the discovery of minerals and many other applications. [4] Due to the energetic nature of x-rays, this radiation has the power to break chemical bonds in materials and alter structure too: so-called radiation damage

Figure 1.1: Photograph of the bones in the fingers of a living human hand. The third finger has a ring on it. Reprinted from Röntgen's first x-ray paper [2] with permission

X-ray diffraction was discovered by Friedrich, Knipping, and Laue [5,6] in April 1912 [4]. The crucial finding in this experiment was that x-rays produced interference patterns when they impinged upon and were diffracted by a crystal. This experiment was thought to have proved the electromagnetic nature of x-rays but Laue, who received a Nobel Prize for the discovery, explained the particle and wave nature of x-rays using two models namely: electromagnetic radiation and the particle-like theory. [7] The first diffraction pattern ever recorded on photographic plates was that of a copper sulphate crystal. [4] Within a year of the discovery of x-ray diffraction, W. Bragg exploited the wave nature of x-rays to solve the first crystal structure and determined the rule governing the x-ray diffraction pattern from a crystal as:

$$n\lambda = 2dsin\theta \tag{1.1}$$

where d is the spacing between diffraction planes, θ is the angle of incidence, $\boldsymbol{\lambda}$ is the wavelength and n is any integer. Bragg and his father continued to succeed in describing very simple structures,

[8] e.g. rock salt (NaCl) and their work later led to corroborations of Bohr's atomic model and the concept of chemical bonding through the analysis of x-ray intensities reflected from crystals. [9] The seminal discoveries of Laue and Bragg established the new field of x-ray crystallography and x-ray spectroscopy. Bragg and his father Sir William Henry Bragg won a Nobel Prize in 1915 for their ground breaking work in the analysis of crystal structure using x-rays. [10]

The ability to investigate the detailed atomic structure of solids has enabled scientists to study essential materials such as semiconductors that have become the cornerstones of modern opto-electronic device applications e.g. light emitting diodes (LEDs), solar panels, cell phones and computers. X–ray diffraction techniques are currently used to study the crystal structure of bulk crystals, thin films and polycrystalline films.

Over the past few decades, physicists have relentlessly pushed the limits of x-ray diffraction technology and sought to discover novel techniques that can be used to investigate the intricate aspects of material systems. The advancement in synchrotron x-ray sources since the discovery of synchrotron radiation in 1947 [11] has led to new techniques for material characterization including anomalous scattering, surface crystallography, protein crystallography, microcrystal diffraction, time resolved studies, topography, small angle scattering, x-ray reflectivity studies of liquid surfaces and magnetic scattering. Synchrotron radiation sources are very powerful sources of x-rays that are designed to generate tunable beams of electromagnetic radiation from the far infrared to the hard x-ray regime with intensities ten orders of magnitude greater than those produced by conventional laboratory sources as shown in Figure 1.2. The development of free electron lasers [12] has increased the brilliance of synchrotron radiation even further, by another nine orders of magnitude from third generation synchrotrons.

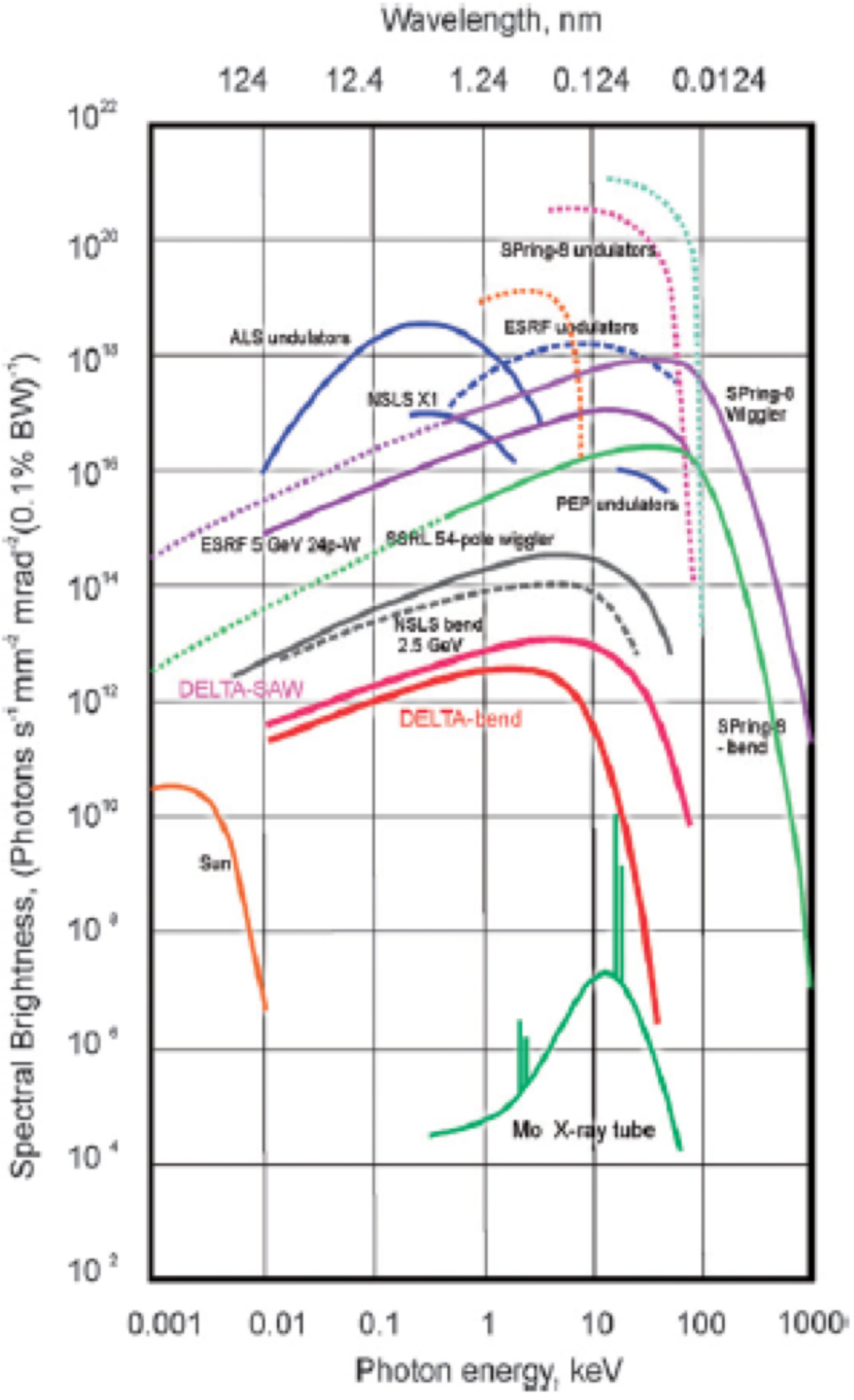

Figure 1.2: Spectral brilliance curves of devices commonly used in third generation synchrotrons [13]

1.2 II-IV Nitride Semiconductors

1.2.1 Need for New Earth Abundant Semiconductors

Semiconductors are widely used in everyday technological applications including photovoltaics, solid state lighting, water splitting, flat panel displays and high speed electronics. While silicon has dominated the photovoltaics industry because of its abundance and an established manufacturing infrastructure, its' shortcomings including an indirect bandgap and a non-ideal bandgap value (1.1eV) for peak absorption, have motivated the search for new materials for use in light harvesting. [14] Currently, high efficiency electronic applications are made with materials containing compounds such as gallium, selenium, cadmium, indium, and tellurium all of which are expensive and can be toxic to the environment. CdTe [15], CIGS [16] and GaAs have all been used to make solar cells while the LED solid state lighting industry has been revolutionized by Indium-based alloys of GaN and InN. These III-V nitrides have been very attractive in the opto-electronics industry due to their direct and tunable bandgaps through alloying. InN with an experimental bandgap of 0.7eV [17,18,19] has been investigated for use in near infrared applications. While a lot of success has been achieved in producing high efficient LED lighting technology using III-V nitrides, the cost of Indium has significantly increased due to scarcity perpetuated by the rapid adoption of Indium Tin Oxide (ITO) in flat panel display technology. In turn, large scale manufacturing of electronic devices and solar panels has significantly increased, largely driven by the global demand for clean renewable energy. Obviously, there is a real danger that the scarcity of raw materials might limit production and drive up their cost.

These drawbacks have motivated research into earth abundant semiconductors that present a cheap, non-toxic alternative to the expensive materials currently used for high efficieny optoelectronic applications. Materials in this category that are currently under investigation include sulfides (FeS_2 [20-22], SnS [23, 24],) nitrides ($ZnSnN_2$ [25,26], $CuTaN_2$ [27], phosphides (Zn_3P_2 [28,29], $ZnSnP_2$ [30,31]), oxides (Cu_2O [32,33]) and $CaZn_2N_2$, Zn_2PN_3 and Ca_2ZnN_2 [34]). The assimilation of these materials as alternatives for use in efficient high quality optoelectronic devices and solar energy conversion systems could potentially eliminate the high costs associated with end of life disposal of devices that require sophisticated and expensive recycling infrastructure. Earth abundant elements also have the potential to lower the production costs associated with large scale manufacturing and reduce the end user price of products. For example, the crustal abundance of tin is two orders of magnitude greater than that of indium which is approximately 0.25ppm [35,36] and that of zinc is three orders of magnitude greater. [37,38]

I.1.2. Zn-IV-N_2 Semiconductors

In 1957, Goodman proposed a broad class of heterovalent ternary materials that could be derived from the isovalent wurtzite III-V nitride family of compounds. [39] By systematically substituting pairs of column III cations with alternating column II and IV elements, a new class of II-IV-V_2 chalcopyrite materials was demonstrated. [39,40] The first phosphide and arsenide containing members of this family of materials were successfully grown in an evacuated silica tube and their measured band gaps were similar to those of the closely related III-V nitrides. [39] Figure 1.3 shows the close correlation between the bandgaps of Zn-IV-nitrides and their III-V counterparts, although Goodman et al. discovered that the band gaps of the II-IV nitride compounds were narrower due to the weaker IV-V bonds.

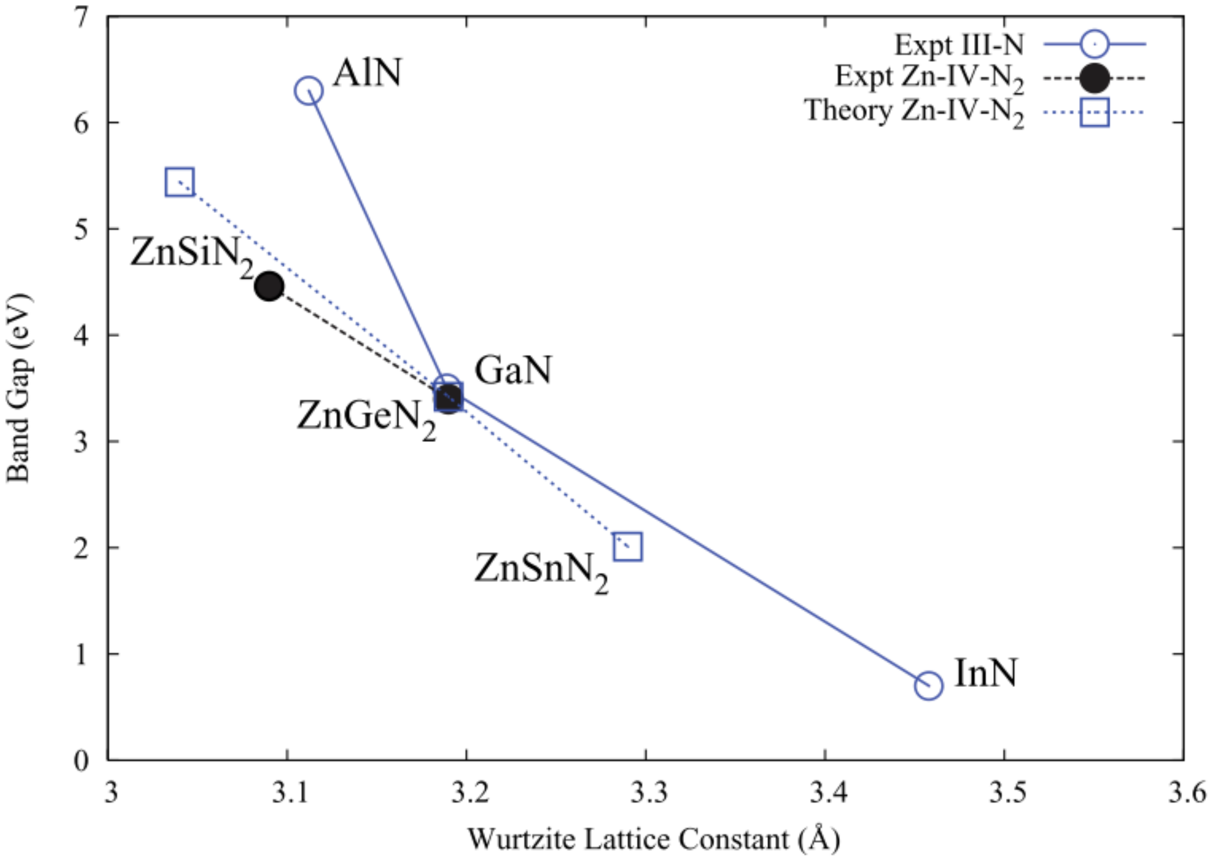

Figure 1.3: Comparison of experimental and theoretical values of bandgap for III-V and II-IV nitride semiconductors. Figure reprinted from [41]

In 1970, a report was published detailing the first successful growth of $ZnGeN_2$, a member of the Zn-IV-N_2 semiconductor family. [42] Density functional theory calculations by Lambrecht et.al later confirmed this experimentally reported structure [40] Subsequently, work on $ZnGeN_2$ focused on band gap tuning through alloying and some work on Mn doping was also reported. [43,44] Orthorhombic $ZnSiN_2$ was grown via high pressure annealing [45] resulting in polycrystalline films and epitaxial films were later grown on c-plane Sapphire and silicon carbide by metal organic chemical vapor deposition (MOCVD). [46] As of this writing, single domain $ZnSnN_2$ films have been successfully grown via plasma assisted molecular beam epitaxy (PAMBE) and through a systematic variation of growth parameters and choice of different substrates, both the predicted wurtzite and orthorhombic crystal structures for $ZnSnN_2$ have been experimentally validated. [47] Quayle et al. have also successfully grown $ZnSnN_2$ polycrystalline films using the vapor liquid solid synthesis technique by exposing a Zn-Sn melt held at temperatures ranging from 400°C to 560°C to a nitrogen plasma. [48]

1.2.3 Advances in Structural and Optoelectronic Characterization of II-IV Nitrides

Atoms are organized in a three-dimensional lattice in a crystal, where the same periodic structure is repeated over the space of the crystal. Group III-nitrides for example crystallize either in the hexagonal wurtzite or zinc blende structures. The structure of Zn-IV nitride compounds is derived from their III-V counterparts in the sense that their lattice structure is derived from the III-nitride wurtzite structure in which each pair of group III atoms is replaced by one Zn atom and one group IV atom as shown in Figure 1.4. The $ZnGeN_2$ structure shown in this figure represents a disordered cation sub-lattice characterized by random placement of Zn, Ge atoms on the cation sub-lattice. On the wurtzite sub-lattice, there is a ½ probability of each cation site being occupied by a group II or IV atom.

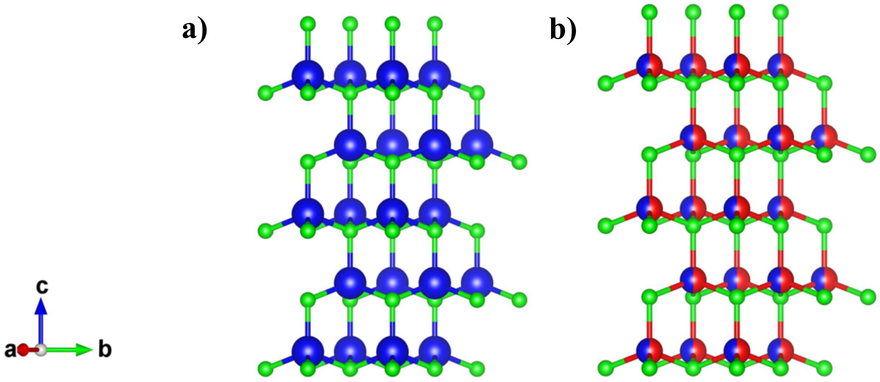

Figure 1.4: Atomic arrangement on cation sub lattice of a) GaN and b) $ZnGeN_2$ showing the relationship between the atomic structures of GaN and the wurtzite structure II-IV nitrides. Zn and Ge atoms are shown in blue and red respectively in the $ZnGeN_2$ structure while Ga atoms are shown in blue in the GaN structure.

The ordered structure found in II-IV nitrides is characterized by an ordered placement of II, IV atoms on the cation sub-lattice. This property of II-IV nitrides results in the well-studied phenomenon of tunable disorder that is responsible for bandgap engineering in semiconductors. [49] First principles calculations predict the most stable crystal structure of II-IV nitride semiconductors to be the orthorhombic β-$NaFeO_2$ (space group $Pna2_1$) which is related to the wurtzite structure of II-VI chalcopyrite compounds. This crystal structure can be viewed as a 2x√3x1 superstructure of the wurtzite structure along orthohexagonal axes as shown in Figure 1.5. [50]

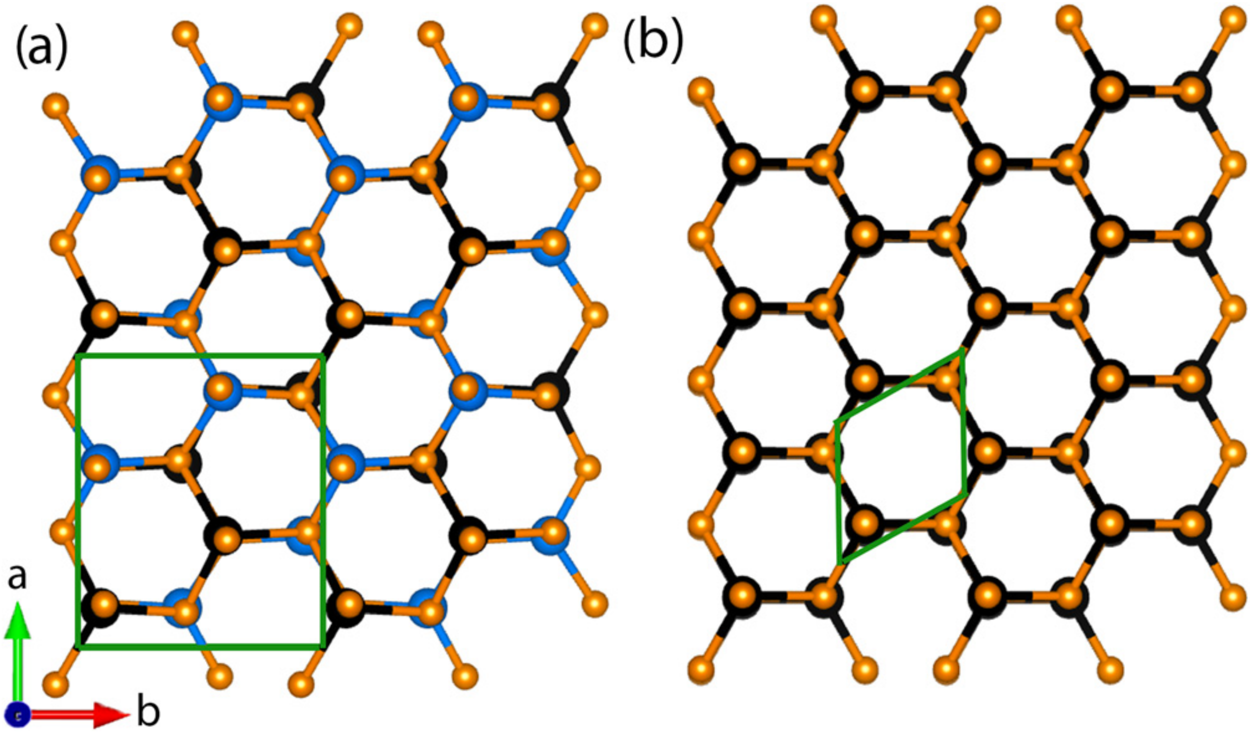

Figure 1.5: Lattice structure for $ZnSnN_2$: (a) orthorhombic ordered cation sublattice; Zn and Sn are represented by blue and black respectively. (b) Disordered cation sublattice; Zn and Sn are random and represented by the same color-black. In both images the small orange atoms are nitrogen. Figure reprinted from [50]

The lattice parameters are chosen to be $a_o = 2a_w$, $b_o \approx a_w\sqrt{3}$ and $c_w = c_o$ in the $Pbn2_1$ orthorhombic symmetry with a two-fold screw axis along the z direction with translation 1/ 2**c**, a diagonal glide plane n perpendicular to b with translations 1/ 2(**a** + **c**), and an axial glide plane perpendicular to the a axis with translation 1/ 2**b**. These symmetry elements of the Pbn2$_1$ space group are shown in Figure 1.6.

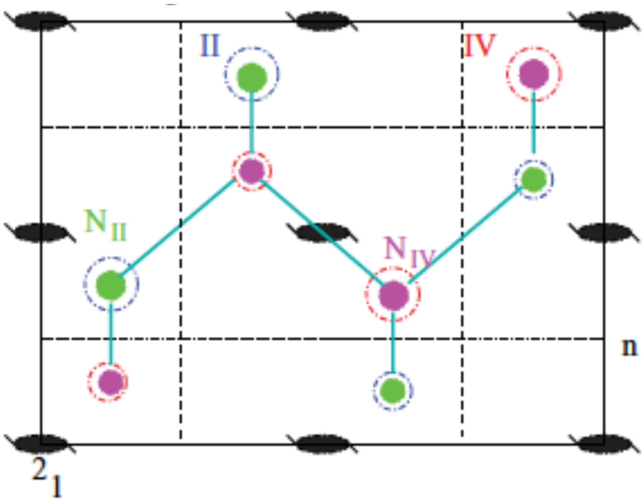

Figure 1.6: Projection of crystal structure of Zn-IV-N_2 compounds on c plane with symmetry elements. Figure reprinted from [41]

The lattice constants obtained by energy minimization in both Local Density Approximation (LDA) and Generalized Gradient Approximation (GGA) are represented in Table 1.1, showing considerable variation in calculated and experimentally measured unit cell lattice parameters for $ZnSnN_2$, $ZnSiN_2$ and $ZnGeN_2$ for the orthorhombic structure. The variations in experimentally determined lattice constants are attributed to differences in synthesis methods of the materials, resulting in epitaxial strain variation at the film substrate interface as discussed in Du et al. [51]. On the other hand, variation in calculated lattice constants are also associated with slight variations in specific computational methods. Differences in the lattice constants of structures calculated by specific computation methods such as LDA are also reported. It is well known for example that LDA slightly underestimates unit cell lattice constants while GGA overestimates the same parameters. Neither of the computational methods, GGA or LDA has shown any clear superior advantage to predicting a more accurate unit cell as both computation methods have shown that they can accurately predict lattice parameters in good agreement with experimental results.

Table 1.1: Comparison of calculated and experimentally determined lattice parameters a, b, and c (Å) and lattice volume V(Å^3) of $ZnSnN_2$, $ZnGeN_2$ and $ZnSiN_2$ films

Material		GGA[a]	LDA[a]	LDA-ABINIT [b]	Experiment [c]
$ZnSnN_2$	a	6.70	6.59	6.76	6.753
	b	5.80	5.70	5.85	5.842
	c	5.53	5.41	5.58	5.462
	V	214.89	203.21	220.67	215.48
$ZnGeN_2$	a	6.42	6.38	6.33	6.44
	b	5.54	5.45	5.36	5.45
	c	5.27	5.22	5.11	5.19
	V	187.44	181.50	173.38	182.16
$ZnSiN_2$	a	6.70	6.59	6.76	6.18
	b	5.80	5.70	5.85	5.35
	c	5.53	5.41	5.58	5.05
	V	214.89	203.21	220.67	166.97

[a] Reference [41]

[b] Reference [52]

[c] $ZnSiN_2$ [53], $ZnGeN_2$ [54], ZnSnN2[55]

Electronic band structures for $ZnSnN_2$, $ZnGeN_2$ and $ZnSiN_2$ have been calculated by various groups to date with bandgap predictions varying widely due to the differences in the computational models used in the studies. Figure 1.7 shows calculated direct band structures for $ZnSiN_2$, $ZnGeN_2$, and $ZnSnN_2$ using the LDA and QSGW functional. Other groups have also reported an indirect low energy band gap in $ZnSiN_2$ [41,56]. With reported bandgaps of 3.1-3.4 eV, [41,51,57,58,59] 4.4 eV, [41,57] and 2.0 eV, [41] for $ZnSiN_2$, $ZnGeN_2$, and $ZnSnN_2$ respectively, it is possible to create materials which completely span the visible spectrum with Zn-IV-nitride semiconductors. This feature is very attractive for photovoltaic and solid state lighting applications.

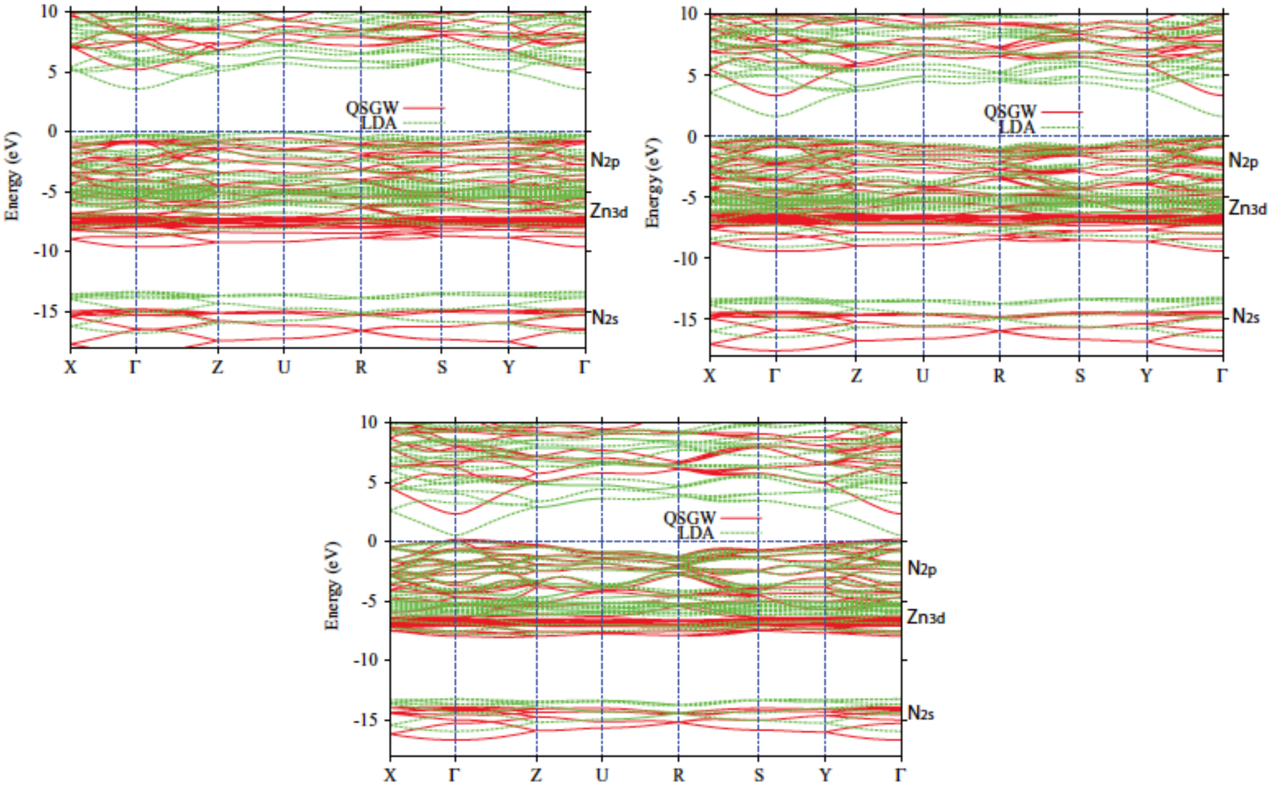

Figure 1.7: Electronic band structure for $ZnSiN_2$, $ZnGeN_2$ and $ZnSnN_2$. Figure reprinted from [41]

Selected theoretical values for the bandgap of Zn-IV nitride semiconductors are listed in Table 1.2. The high band gap values ~ 2eV given for $ZnSnN_2$ have been attributed to high carrier concentration in the films combined with a low conduction band effective mass that incurs a large Burstein Moss shift in the apparent optical gap. In this scenario, free electrons fill the bottom of the conduction band and pin the fermi level to energies well above the conduction band edge consequently blocking low energy excitations to yield a measured band gap that is much larger than the fundamental band gap of the material.

Table 1.2: Selected calculated electronic band gaps for Zn-IV nitride semiconductors. Band gap values are direct transitions unless otherwise stated and are given in units of electron volts. Bandgap values for ZnSnN2 correspond to the ordered orthorhombic phase.

Functional	$ZnSnN_2$	$ZnGeN_2$	$ZnSiN_2$
LDA [56]		2.04	
LDA [60]		2.8	
GGA [56]		1.67	3.32(indirect)
QSGW [41]			5.44(indirect)
QSGW [41]	2.02	3.42	5.66
PBE [50]	2.09		
HSE06 [25]	1.42		

1.2.4 Order and Disorder on the Cation Sublattice of II-IV Nitrides

Heterovalent ternary compounds (HTCs) offer a unique opportunity to tune their electrical properties through structural changes of the crystal lattice. Several materials are currently under investigation [61,62] for disordered photonics [63] and light trapping applications [64]. Specifically, in some HTCs, the band gap of the material can be controlled by introducing disorder into the cation sublattice. Disorder-induced band-gap tuning was experimentally first reported in $GaInP_2$ films where the introduction of Sb during growth led to the random placement of cations in the Ga-In sublattice, leading to an increase of up to 0.135 eV in the direct band gap.[65] Recently, theoretical calculations of the $ZnSnP_2$ band structure predicted a 0.95 eV reduction of the band gap, when the Zn-Sn sub-lattice is fully disordered.[66] This bandgap narrowing was attributed to crystal field splitting of the s-p valence band.[66] Experimentally, however, disordering of the cation sublattice has so far only achieved a 0.3 eV reduction in the band gap with the apparent differences in band-gap narrowing attributed to variations in cation-sublattice disorder and the possibility of partial disorder approximately 30% to 40% on the cation sublattice. Theoretical calculations predict a larger reduction in bandgap in fully disordered compounds. [66,67]

III–V isoelectronic alloys also form in a wide range of crystal structures with varying degrees of cation ordering. [68] In these alloys, cation ordering of CuPt type is typically observed, even though the cation disordered structure is a more stable state at room temperature. [69] Cation sublattice ordering leads to band structure modification and band gap variability of 0.2– 0.4 eV [70]. This is possibly related to differences in crystal structure in ordered and disordered materials coupled with variation in dislocation dynamics in the two crystal systems and resulting differences in the defect density of the materials.

In $ZnSnN_2$, DFT calculations predicted an orthorhombic structure in the $Pna2_1$ symmetry although experimental work has shown that these films can grow in both the wurtzite [42,51,59,71] and orthorhombic structures [61,72]. The wurtzite structure is a result of disorder on the cation sub lattice caused by random placement of Zn-Sn atoms on the cation sites. In this case, each nitrogen atom is no longer associated with two Sn and two Zn atoms leading to a violation of the octet rule [55]. Our experiments however have verified the existence of this wurtzite structure despite the octet rule violations. Another form of disorder that does not violate the octet rule was proposed by Quayle et al. that systematically stacks alternate layers of the $Pna2_1$ and $Pmc2_1$ structures normal to the basal plane. Alternatively, a completely ordered cation sublattice of $ZnSnN_2$ is predicted to form the orthorhombic $Pna2_1$ structure. Far from being detrimental, this order-disorder behavior has several potential effects on the structural, optical and electrical properties of $ZnSnN_2$. The bandgap of $ZnSnN_2$ for example is predicted to decrease from ~ 1.8 eV in the completely ordered orthorhombic structure to ~ 1 eV in the completely disordered wurtzite structure [50,73], a range that makes $ZnSnN_2$ a prime candidate for photovoltaic applications and light-emitting diode technology. This tuning of the bandgap through ordering variation on the cation sub-lattice eliminates the need for alloying commonly used to tune the opto-electronic properties of semiconductors while introducing unwanted defects in materials. Fang et al. also used DFT calculations combined with hybrid functional forms to investigate the electronic structure of ($ZnSnN_2$/ZnO) superlattices and found that the bandgap can be tuned by varying the thickness of both the $ZnSnN_2$ and ZnO layers. In this study, tensile strain increased the bandgap while compressive strain decreased the bandgap. This computational work shows that it is still possible to tune the bandgap of $ZnSnN_2$ using strain and film thickness. [74]

For these II–IV nitride materials, the ordered structures are the most thermodynamically stable and have the largest band gaps, contrary to observations in III-V nitride materials [75]. This is because of the fundamental difference in charge of group II and group IV cations, making the ordered and disordered materials have larger energy differences and larger variation in properties between their ordered and disordered structures than their III–V analogs. The degree of ordering in II–IV nitrides is described by the order parameter, $\boldsymbol{\eta}$, which is given by the formula:

$$\eta = r_a^{II} + r_b^{IV} - 1$$

where r_i^X is the actual occupancy of the group X element on the I site. Here, a refers to the group-II site and b is the group-IV site in the perfectly ordered structure. [76] Another parameter used to gauge the tendency of a material to disorder is the ratio of its melting point to its order/disorder transition temperature; $T_{melt}/T_{disorder}$. If the ratio is equal to one, it indicates that the material remains fully ordered until it melts. On the other hand, if this ratio is large, there is a larger temperature region between the two transition temperatures, meaning that the order parameter may be controllably varied within that region.

1.3 Dissertation Outline

The basic principles of x-ray scattering will be introduced in chapter II, followed by a description of the physical properties and potential applications of $ZnSnN_2$ in chapter III. This will also include a discussion on the relationship between cation sublattice ordering and the crystal structure of $ZnSnN_2$. Chapter IV will be focused on experimental techniques and data analysis methods used for synchrotron x-ray diffraction experiments and microscopy measurements.

Chapter V will address the results and discussions from structural investigations on $ZnSnN_2$ films grown on (001) $LiGaO_2$ and (111) Yttria stabilized zirconia substrates. Results showing the impact of cation ordering on the structure of $ZnSnN_2$ films will be presented as will the results and discussion from the systematic studies on the influence of molecular beam epitaxy growth conditions and annealing on the crystal structure of $ZnSnN_2$ films. Finally, the results from this dissertation will be summarized in Chapter VI with some outlook and future directions for continuing this work.

Bibliography

[1] W. C. Röntgen, “Über eine neue Art von Strahlen,” Sitzungsber. Der. Würzburger Physik-Medic. Gesellsch. 137, 132 (1895).

[2] W. C. Röntgen, “On a new kind of rays,” Nature 53, 274 (1896), [translated by A. Stanton].

[3] J. Maddox, “The sensational Discovery of X-rays,” Nature, 375, p. 183, 1995.

[4] A. Authier, Early days of X-ray crystallography (Oxford, U.K: Oxford University Press, 2013).

[5] W. Friedrich, P. Knipping, and M. von Laue, “Interferenz-Erscheinungen bei Röntgenstrahlen,” Sitzungsberichte der Kgl. Bayer. Akad. der Wiss. , 303 (1912).

[6] W. Friedrich, P. Knipping, and M. von Laue, “Interferenz-Erscheinungen bei Röntgenstrahlen,” Ann. Phys. 346, 971 (1913).

[7] Wheaton 1984

[8] 1915 physics Nobel laureates website

[9] Compton, A. (1917), "The Intensity of X-ray Reflection, and the Distribution of Electrons in Atoms", Physical Review, N. S., 9, 29-57

[10] W. L. Bragg, “The diffraction of short Electromagnetic Waves by a Crystal,” Proc. Cambridge Phil. Soc. A 17, 43 (1913).

[11] Elder et. al 1947

[12] Huang, Z.; Kim, K. J. (2007). "Review of x-ray free-electron laser theory". *Physical Review Special Topics - Accelerators and Beams*. **10** (3). Bibcode:2007PhRvS..10c4801H. doi:10.1103/PhysRevSTAB.10.03480

[13] A. V Bohlen, M. Tolan, Editorial for Synchrotron Radiation, J. Anal. At. Spectrom., 2008,23, 790-791, DOI: 10.1039/B804010A

[14] William Shockley and Hans J. Queisser, "Detailed Balance Limit of Efficiency of p-n Junction Solar Cells," Journal of Applied Physics 32 (3), 510-519 (1961).

[15] Philip Jackson, Dimitrios Hariskos, Erwin Lotter, Stefan Paetel, Roland Wuerz, Richard Menner, Wiltraud Wischmann, and Michael Powalla, "New world record efficiency for Cu(In,Ga)Se2 thin-film solar cells beyond 20%," Progress in Photovoltaics: Research and Applications 19 (7), 894-897 (2011).

[16] A. Romeo, M. Terheggen, D. Abou-Ras, D. L. Bätzner, F. J. Haug, M. Kälin, D. Rudmann, and A. N. Titwari, "Development of Thin-film Cu(In,Ga)Se2 and CdTe Solar Cells," Progress in Photovoltaics: Research and Applications 12, 93-111 (2004).

[17] K.S.A Butcher and T.L. Tansley, "InN, Latest development and a review of the band-gap controversy," Superlattices and Microstructures 38, 1-37 (2005).

[18] K. M. Yu, Z. Liliental-Weber, W. Walukiewicz, W. Shan, J. W. Ager, S. X. Li, R. E. Jones, E. E. Haller, Hai Lu, and William J. Schaff, "On the crystalline structure, stoichiometry and band gap of InN thin films," Applied Physics Letters 86 (7), 071910 (2005).

[19] V. Yu Davydov, A. A. Klochikhin, V. V. Emtsev, D. A. Kurdyukov, S. V. Ivanov, V. A. Vekshin, F. Bechstedt, J. Furthmüller, J. Aderhold, J. Graul, A. V. Mudryi, H. Harima, A. Hashimoto, A. Yamamoto, and E. E. Haller, "Band Gap of Hexagonal InN and InGaN Alloys," physica status solidi (b) 234 (3), 787-795 (2002).

[20] J.Puthussery,S.Seefeld,N.Berry,M.Gibbs,M.Law,Colloidalironpyrite(FeS2) nanocrystal inks for thin-film photovoltaics,J.Am.Chem.Soc.133(4)(2011) 716–719. http://dx.doi.org/10.1021/ja1096368arXiv:http://pubs.acs.org/doi/pdf/10.1021/ja1096368, URL: ⟨http://pubs.acs.org/doi/abs/10.1021/ja1096368⟩.

[21] R. Morrish, R.Silverstein,C.A.Wolden,SynthesisofstoichiometricFeS2 through plasma-assistedsulfurizationofFe2O3 nanorods, J.Am.Chem.Soc. 134(43)(2012)17854–17857. http://dx.doi.org/10.1021/ja307412earXiv: http://pubs.acs.org/doi/pdf/10.1021/ja307412e, URL: ⟨http://pubs.acs.org/doi/ abs/10.1021/ja307412e⟩.

[22] M.Cabn-Acevedo,M.S.Faber,Y.Tan,R.J.Hamers,S.Jin,Synthesis and properties of semiconducting iron pyrite(FeS2) nanowires,NanoLett.12(4) (2012)1977–1982. http://dx.doi.org/10.1021/nl2045364arXiv:http://pubs.acs. org/doi/pdf/10.1021/nl2045364. URL: ⟨http://pubs.acs.org/doi/abs/10.1021/ nl2045364⟩.

[23] P.Sinsermsuksakul,K.Hartman,S.BokKim,J.Heo,L.Sun,H.HejinPark, R. Chakraborty,T.Buonassisi,R.G.Gordon,Enhancing the efficiency of sns solar cells via band offset engineering with a zinc oxysulfide bufferlayer, Appl. Phys.Lett.102(5)(2013),doi:http://dx.doi.org/10.1063/1.4789855. URL: ⟨ http://scitation.aip.org/content/aip/journal/apl/102/5/10.1063/1.4789855⟩ .

[24] J.Vidal,S.Lany,M.d'Avezac,A.Zunger,A.Zakutayev,J.Francis,J.Tate,Band- structure, optical properties, and defect physics of the photovoltaic semiconductor sns,Appl.Phys.Lett.100(3)(2012),doi:http://dx.doi.org/10.1063/1. 3675880. URL: ⟨ http://scitation.aip.org/content/aip/journal/apl/100/3/10.1063/ 1.3675880⟩ .

[25] L.Lahourcade,N.C.Coronel,K.T.Delaney,S.K.Shukla,N.A.Spaldin,H. A.Atwater, Structural and optoelectronic characterization of rf sputtered ZnSnN2, Adv.Mater.25(18)(2013)2562–2566. http://dx.doi.org/10.1002/ adma.201204718 URL: http://dx.doi.org/10.1002/adma.201204718.

[26] P.C.Quayle,K.He,J.Shan,K.Kash,Synthesis,lattice structure,and bandgap of ZnSnN2, MRSCommun.3(2013)135–138. http://dx.doi.org/10.1557/mrc.2013.19.

[27] M.Yang,A.Zakutayev,J.Vidal,X.Zhang,D.S.Ginley,F.J.DiSalvo,Strongoptical absorption in cutan2nitridedelafossite,EnergyEnviron.Sci.6(2013) 2994–2999. http://dx.doi.org/10.1039/C3EE40621K.

[28] J.P.Bosco,S.B.Demers,G.M.Kimball,N.S.Lewis,H.A.Atwater,Bandalignment of epitaxialZnS/Zn3P2 heterojunctions,J.Appl.Phys.112(9)(2012),doi:http://

dx.doi.org/10.1063/1.4759280. URL: 〈 http://scitation.aip.org/content/aip/journal/jap/112/9/10.1063/1.4759280〉 .

[29] G.M.Kimball,A.M.Müller,N.S.Lewis,H.A.Atwater,Photoluminescence-based measurements of the energy gap and diffusion length of Zn3P2, Appl.Phys. Lett. 95(11)(2009),doi:http://dx.doi.org/10.1063/1.3225151. URL: 〈 http:// scitation.aip.org/content/aip/journal/apl/95/11/10.1063/1.3225151〉 .

[30] D.O.Scanlon,A.Walsh,Bandgap engineering of ZnSnP2 for high-efficiency solar cells,Appl.Phys.Lett.100(25)(2012),doi:http://dx.doi.org/10.1063/1. 4730375. URL: 〈 http://scitation.aip.org/content/aip/journal/apl/100/25/10. 1063/1.4730375〉 .

[31] Y.Hinuma,F.Oba,Y.Nose,I.Tanaka,First-principlesstudyofvalenceband offsets at ZnSnP2/cds, ZnSnP2/ZnS, and related chalcopyrite/ zinc blende hetero interfaces,J.Appl.Phys.114(4)(2013),doi:http://dx.doi.org/10.1063/ 1.4816784. URL: 〈 http://scitation.aip.org/content/aip/journal/jap/114/4/10. 1063/1.4816784〉 .

[32] Y.S.Lee,J.Heo,S.C.Siah,J.P.Mailoa,R.E.Brandt,S.B.Kim,R.G.Gordon, T.Buonassisi,Ultrathinamorphouszinc-tin oxide buffer layer for enhancing heterojunction interface quality in metal-oxide solar cells,EnergyEnviron.Sci. 6 (2013)2112–2118. http://dx.doi.org/10.1039/C3EE24461J URL: http://dx.doi. org/10.1039/C3EE24461J.

[33] T.Minami,Y.Nishi,T.Miyata,High-efficiency Cu2O-based heterojunctionsolar cells fabricatedusingaGa2O3 thin film asn-typelayer,Appl.Phys.Express 6 (4)(2013)044101. http://dx.doi.org/10.7567/APEX.6.044101 URL: 〈 http:// apex.jsap.jp/link?APEX/6/044101/〉 .

[34] Yoyo Hinuma, Taisuke Hatakeyama, Yu Kumagai, Lee A. Burton, Hikaru Sato, Yoshinori Muraba, Soshi Iimura, Hidenori Hiramatsu, Isao Tanaka, Hideo Hosono & Fumiyasu Oba, Discovery of earth-abundant nitride semiconductors by computational screening and high-

pressure synthesis, NATURE COMMUNICATIONS | 7:11962 | DOI: 10.1038/ncomms11962 |www.nature.com/naturecommunications

[35] A. C. Tolcin, Mineral Commodity Summaries 2013 (U.S. Geological Survey, Reston, Virginia, 2013), pp. 74–76.

[36] B. W. Jaskula, Mineral Commodity Summaries 2013 (U.S. Geological Survey, Reston, Virginia, 2013), pp. 58–60.

[37] A. C. Tolcin, Mineral Commodity Summaries 2013 (U.S. Geological Survey, Reston, Virginia, 2013), pp. 188–189.

[38] J. F. Carlin, Mineral Commodity Summaries 2013 (U.S. Geological Survey, Reston, Virginia, 2013), pp. 170–171.

[39] C. H. L. Goodman, "A New Group of Compounds with Diamond type (Chalcopyrite) Structure," Nature 179 (4564), 828-829 (1957).

[40] Walter R. L. Lambrecht, Erik Alldredge, and Kwiseon Kim, "Structure and phonons of ZnGeN2," Physical Review B 72 (15), 155202 (2005).

[41] Atchara Punya and Walter R. L. Lambrecht, Quasiparticle band structure of Zn-IV-N2 compounds, PHYSICAL REVIEW B 84, 165204 (2011)

[42] M. Maunaye and J. Lang, "Preparation et proprietes de ZnGeN2," Materials Research Bulletin 5 (9), 793-796 (1970).

[43] A. Osinsky, V. Fuflyigin, L. D. Zhu, A. B. Goulakov, J. W. Graff, and E. F. Schubert, "New concepts and preliminary results for SiC bipolar transistors: ZnSiN2 and ZnGeN2 heterojunction emitters", in High Performance Devices, 2000. Proceedings 2000 IEEE/Cornell Conference on (2000), pp. 168-172.

[44] Alexander Mintairov, James Merz, Andrei Osinsky, Vladimir Fuflyigin, and L. D. Zhu,

"Infrared spectroscopy of ZnSiN2 single-crystalline films on r-sapphire," Applied Physics Letters 76 (18), 2517-2519 (2000).

[45] T. Endo, Y. Sato, H. Takizawa, and M. Shimada, "High-pressure synthesis of new compounds, ZnSiN2 and ZnGeN2 with distorted wurtzite structure," J. Mater. Sci. Lett. 11 (7), 424-426 (1992).

[46] T. Cloitre, A. Sere, and R. L. Aulombard, "Epitaxial growth of ZnSiN2 single-crystalline films on sapphire substrates," Superlattices and Microstructures 36 (4–6), 377-383 (2004).

[47] N. Senabulya, N. Feldberg, R. A. Makin, Y. Yang, G. Shi, C. M. Jones, E. Kioupakis, J. Mathis, R. Clarke, S. M. Durbin, Stabilization of orthorhombic phase in single-crystal znsnn2 films, AIP Advances 6 (7) (2016) 075019.

[48] Paul C. Quayle, Grant T. Junno, Keliang He, Eric W. Blanton, Jie Shan, and Kathleen Kash Vapor–liquid–solid synthesis of $ZnSnN_2$, Phys. Status Solidi B, 1600718 (2017) / DOI 10.1002/pssb.201600718

[49] A. Mascarenhas, Spontaneous Ordering in Semiconductor Alloys (Plenum Pub Corp, 2002).

[50] Feldberg, N., et al., Growth, disorder, and physical properties of ZnSnN2. Applied Physics Letters, 2013. 103(4): p. 042109.

[51] K. Du, C. Bekele, C. C. Hayman, J. C. Angus, P. Pirouz, and K. Kash, "Synthesis and characterization of ZnGeN2 grown from elemental Zn and Ge sources," Journal of Crystal Growth 310 (6), 1057-1061 (2008).

[52] Paudel, T.R. and W.R.L. Lambrecht, First-principles study of phonons and related ground-state properties and spectra in Zn-IV-N2 compounds. Physical Review B, 2008. 78: p. 115204.

[53] Mintairov, A., et al., Infrared spectroscopy of ZnSiN2 single-crystalline films on r sapphire. Appl. Phys. Lett., 2000. 76: p. 2517-2519.

[54] Endo, T., et al., High-pressure synthesis of new compounds, ZnSiN2 and ZnGeN2 with distorted wurtzite structure. Journal of Materials Science Letters, 1992. 11(7): p. 424-426.

[55] Quayle, P.C., et al., Synthesis, lattice structure, and band gap of ZnSnN2. MRS Communications, 2013: p. 1-4.

[56] Shaposhnikov, V.L., et al., Structural, electronic and optical properties of II–IV–N2 compounds (II = Be, Zn; IV = Si, Ge). physica status solidi (b), 2008. 245(1): p. 142-148.

[57] K. Tsuchiya T. Misaki, D. Sakai, A Wakahara, H. Okada, A. Yoshida, "Growth and Characterizatino of ZnGeN2 by using Remote-Plasma Enhanced Metalorganic Vapor Phase Epitaxy," physica status solidi (c) 0 (1), 188-191 (2002).

[58] A. Osinsky, V. Fuflyigin, L. D. Zhu, A. B. Goulakov, J. W. Graff, and E. F. Schubert, "New concepts and preliminary results for SiC bipolar transistors: ZnSiN2 and ZnGeN2 heterojunction emitters", in High Performance Devices, 2000. Proceedings 2000 IEEE/Cornell Conference on (2000), pp. 168-172.

[59] S. Kikkawa and H. Morisaka, "RF-sputter deposition of Zn–Ge nitride thin films," Solid State Communications 112 (9), 513-515 (1999).

[60] Limpijumnong, S., S.N. Rashkeev, and W.R.L. Lambrecht, Electronic Structure and Optical Properties of ZnGeN2. MRS Internet J. Nitride Semicond. Res., 1999. 4S1: p. G6.11.

[61] "Disordered times," Nat Photon 7 (3), 161-161 (2013).

[62] "Random thoughts," Nat Photon 7 (3), 164-165 (2013).

[63] Diederik S. Wiersma, "Disordered photonics," Nat Photon 7 (3), 188-196 (2013).

[64] Mordechai Segev, Yaron Silberberg, and Demetrios N. Christodoulides, "Anderson localization of light," Nat Photon 7 (3), 197-204 (2013).

[65] J. K. Shurtleff, R. T. Lee, C. M. Fetzer, and G. B. Stringfellow, Applied Physics Letters 75, 1914–1916 (1999).

[66] D. O. Scanlon and A. Walsh, Applied Physics Letters 100, 251911 (2012).

[67] P. St-Jean, G. A. Seryogin, and S. Francoeur, Applied Physics Letters 96, 231913 (2010).

[68] A. Mascarenhas, Spontaneous Ordering in Semiconductor Alloys, Springer, US, 2012.

[69] S.-H. Wei, S. B. Zhang and A. Zunger, Phys. Rev. B: Condens. Matter Mater. Phys., 1999, 59, R2478–R2481.

[70] S.-H. Wei and A. Zunger, Phys. Rev. B: Condens. Matter Mater. Phys., 1998, 57, 8983–8988.

[71] W. L. Larson, H. Paul Maruska, and D. A. Stevenson, "Synthesis and Properties of ZnGeN2," Journal of the Electrochemical Society 121 (1974).

[72] N. Naghavi, S. Spiering, M. Powalla, B. Cavana, and D. Lincot, "High-efficiency copper indium gallium diselenide (CIGS) solar cells with indium sulfide buffer layers deposited by atomic layer chemical vapor deposition (ALCVD)," Progress in Photovoltaics: Research and Applications 11 (7), 437-443 (2003).

[73] T. D. Veal, N. Feldberg, N. F. Quackenbush, W. M. Linhart, D. O. Scanlon, L. F. Piper, S. M. Durbin, Band gap dependence on cation disorder in znsnn2 solar absorber, Advanced Energy Materials 5 (24).

[74] D. Q. Fang, Y. Zhang and S.L. Zhang, Bandgap engineering of ZnSnN2/ ZnO (001) short-period superlattices via built in electric field. Journal of Applied Physics **120**, 215703 (2016); doi: 10.1063/1.4971176

[75] A. Martinez, A. Fioretti, E. Toberer and A. Tamboli, Synthesis, structure, and optoelectronic properties of II–IV–V2 materials, Journal of Materials Chemistry A, DOI: 10.1039/c7ta00406k

[76] S. Nakatsuka and Y. Nose, J. Phys. Chem. C, 2016, 121(2), 1040–1046.

CHAPTER II

X-ray Scattering Theory

2.1 Introduction

The goal of this chapter is to review the basic principles of x-ray diffraction and single crystal x-ray diffraction in a qualitative manner and to educate the reader on the principles governing the calculation of x-ray diffraction intensity from a system with long range order such as a single crystal. Several publications, including the well-known condensed matter physics books by C. Kittel [1] and N. Ashcroft and N. D. Mermin [2], as well as many x-ray crystallography texts [3–9] describe the underlying theory of x-ray scattering in detail. While, x-ray diffraction data has been a very powerful source of structural information when applied to the study of bulk crystals in materials research across a variety of disciplines, the specific theory describing the scattering of x-rays from crystal surfaces has only been recently developed compared to its bulk counterpart, [9–13].

This chapter is presented as a detailed overview of the x-ray diffraction theory from bulk crystals for the novice crystallographer. It is a quick introductory summary to the basics of x-ray diffraction. In section 2.1, we shall present the diffraction theory for bulk crystals proceeding to discuss in relative detail the scattering from free electrons, charge distributions, isolated atoms and ideal bulk crystals in sections [2.1.1], [2.1.2], [2.1.3] and [2.1.4] respectively. Lastly, we shall discuss how x-ray diffraction intensities are computed in diffraction experiments and introduce the concept of the structure factor of a crystal.

2.2 X-ray Diffraction from Bulk Crystals

2.2.1 X-ray Scattering from a Free Electron

X-rays are electromagnetic radiation that manifest both wave and particle properties with wavelength and frequencies of the order of $\lambda = 1$ Å and $\omega = 2\pi c/\lambda$ where c is the speed of light. Due to the dualistic wave-particle nature of x-rays, there are two types of x-ray scattering of electrons i.e. Thompson scattering which is scattering due to electromagnetic waves and electron interactions, and Compton scattering due to photon and electron interactions. In classical electrodynamics, when a plane of electromagnetic radiation excites a charged particle, that particle is accelerated and consequently emits radiation in directions different from that of the incident wave [14]. If the energy of the scattered photon is conserved in the scattering process i.e. the emitted radiation has the same wavelength as the incident x-ray, this process is called elastic scattering or Thompson scattering. On the other hand, if part of the energy of the incident electromagnetic radiation is transferred to the scattering particle so that the scattered wave has less energy than the incident wave, the process is referred to as Compton scattering. For all practical purposes, only Thompson scattering is considered in our discussion here because the Compton scattering cross section is quite negligible compared to that for Thompson scattering for the wavelength range of most x-ray sources used for diffraction experiments [15]. The largest deviations from the Thompson scattering approximation occur when the incident x-ray energy is close to the x-ray absorption edges of the atom. The x-ray wavelengths used for crystallographic structure determination in this work are typically of a similar size to the dimensions of the atoms being investigated (~1 Å).

Let us consider a linearly polarized, monochromatic plane wave x-ray incident on a stationary free electron with charge e and mass m. The electric field of the incident plane wave is given as:

$$E_o(x) = \epsilon_o E_o e^{ik_o \cdot x} \tag{2.1}$$

where $k_o$is the propagation vector, $\epsilon_o$is the polarization vector and $E_o$is the amplitude of the electric field. From Newton's second law of motion, the equation of motion for the driven harmonic oscillation of the electron is given by:

$$m\ddot{a} = eE_o(x) \tag{2.2}$$

Therefore, a charged particle at a position r with charge e and mass m will experience an oscillating acceleration given by:

$$\ddot{a} = \frac{e}{m}\epsilon_o E_o e^{ik_o . r} \tag{2.3}$$

Since an accelerated particle emits electromagnetic radiation, the oscillating electron is essentially an x-ray source that radiates spherically in all directions and the scattered radiation has the same frequency as the incident x-rays. The electric field of the scattered wave propagating in the $\hat{k}$ direction at a distance R from the scattering particle is:

$$\mathrm{E} = \frac{1}{4\pi\varepsilon_o c^2}\frac{\hat{\mathrm{k}} \times (\hat{\mathrm{k}} \times \ddot{\mathrm{a}})}{\mathrm{R}} \tag{2.4}$$

However, $\ddot{a} = \frac{e}{m}\epsilon_o E_o e^{ik_o \cdot r}$

Therefore, the electric field of the scattered wave can be written as:

$$\mathbf{E} = \frac{1}{4\pi\varepsilon_o c^2}\frac{\mathrm{e}^2}{\mathrm{mc}^2}\frac{1}{\mathrm{R}}\mathrm{E}_o e^{ik_o \cdot r}\hat{k}\times(\hat{k}\times\epsilon_o) \tag{2.5}$$

where $|\hat{k}\times\epsilon_o|$ is the polarization factor. From equation 2.5 the electric field amplitude of the scattered wave is inversely proportional to the mass of the scattering particle and the scattering amplitude can be given as

$$E = E_o \frac{r_e}{R}|\hat{k}\times\epsilon_o|e^{i\mathbf{q}\cdot\mathbf{r}} \tag{2.6}$$

where $\mathbf{q} \equiv \vec{k} - \overrightarrow{\mathrm{k_o}}$ is the scattering momentum transfer and $r_e = \frac{1}{4\pi\varepsilon_o}\frac{e^2}{mc^2}$ is the electron radius.

2.2.2 Scattering from a Charge Distribution

In a spatial distribution of charges, the scattered wave is made up of contributions from the secondary waves emitted from each individual scattering center. Assuming N scatterers at positions $r_j \ (1 \leq j \leq N)$ from the reference point r, the total amplitude A_{tot} represents the coherent addition of all individual waves:

$$A_{tot} = \mathcal{K} \cdot \sum_{j=1}^{N} e^{iq(r+r_j)} = \mathcal{K} \cdot e^{iqr} \cdot \sum_{j=1}^{N} e^{iqr_j} \tag{2.7}$$

If the charge distribution is continuous, the summation over all individual scatterers is replaced by an integral over all space where the charge density $\rho(r')$ is non-zero.

$$A_{tot} = \mathcal{K} \cdot \int e^{i\mathbf{q}(\mathbf{r}+\mathbf{r}')\cdot} \rho(r') d^3r' \tag{2.8}$$

This equation is the very foundation of x-ray diffraction. It shows that the amplitude of the scattered wave is the Fourier transform of the electron distribution of the crystal system. Hence by studying the scattered waves for different values of the scattering wave vector **q**, it is possible in principle, with information about the phase of the scattered waves, to derive all the Fourier transforms of the electron distribution, and from those, the electron distribution itself.

2.2.3 X-ray Scattering from an Isolated Atom

In a single atom, electrons are localized around the nucleus and their distribution is described by an atomic charge density $\rho_a(r')$. From equation 2.7 above, the scattering amplitude from an isolated atom is given by:

$$A_a = \mathcal{K} \cdot \int e^{iq(r+r')\cdot} \rho_a (r') d^3r' = \mathcal{K} \cdot e^{iqr} \cdot \int_{atom} e^{iqr'} \cdot \rho_a(r') d^3r' \tag{2.9}$$

where

$$f_a(q) = \int_{atom} e^{iqr'} \cdot \rho_a(r') d^3r' \tag{2.10}$$

is the atomic form factor.

A look at the two limiting cases of the atomic factor yields:

$$f_a(q = 0) = \int \rho_a(r')d^3r' = Z \tag{2.11}$$

where Z is the atomic number.

The other scenario where $(q \to \infty)$ yields:

$$f_a(q \to \infty) = 0 \tag{2.12}$$

In this case the phase factor term $e^{iq(r')}$ oscillates with a frequency approaching infinity, making all scattering contributions cancel out on average.

Last, it is important to note that for isolated atoms, the atomic form factor is expressed as

$$f_a = f_o(\theta) + f'(\omega) + if''(\omega), \tag{2.13}$$

where θ is the scattering angle and ω is the frequency of the incident wave. The factor f' accounts for dispersion corrections while f'' accounts for absorption processes. For x-ray diffraction measurements, far away from any absorption edges, these corrections are very small and can be ignored. In that case $f_a = f_o(\theta)$. The values of f_o, f' and f'' are available in the International Tables for Crystallography. [16]

2.2.4 X-ray Scattering from ideal Bulk Crystals

When unit cells are arranged in a 3-dimensional lattice, a crystalline structure is formed. In this case the scattering from an entire crystal is obtained by summing up the scattering contributions from each unit cell. Consider a crystal consisting of unit cells N_1, N_2 and N_3 along a_1, a_2 and a_3 axes respectively. The amplitude A_c of the wave scattered by the whole crystal is given by the amplitude A_{uc} of the scattered wave from a single unit cell multiplied by the sum over the phase terms associated with the unit cell position in the crystal, $r_{uc} = j_1a_1 + j_2a_2 + j_3a_3$.

$$A_c = \mathcal{K} \cdot e^{iqr} \cdot F(q) \cdot \sum_{j_1=0}^{N_1-1} \sum_{j_2=0}^{N_2-1} \sum_{j_3=0}^{N_3-1} e^{iq\cdot(r_{uc})}$$

$$= \mathcal{K} \cdot e^{iqr} \cdot F(q) \cdot \sum_{j_1=0}^{N_1=0} e^{iq\cdot(j_1\cdot a_1)} \cdot \sum_{j_2=0}^{N_2=0} e^{iq\cdot(j_2\cdot a_2)} \cdot \sum_{j_3=0}^{N_3=0} e^{iq\cdot(j_3\cdot a_3)} \qquad (2.14)$$

2.2.5 Diffraction Pattern and Fourier Transform

X-ray diffraction theory suggests that the intensity of the scattered x-ray beam is proportional to the square of the magnitude of the Fourier transform of the electron density of the scattering system [17, 18, 19]. This definition is derived from the First-Born approximation which is based on the premise that in the absence of multiple scattering events, in other words, taking the kinematical approximation into consideration and neglecting the absorption of radiation with subsequent emission:

$$I(Q) \propto |F(Q)|^2 \qquad (2.15)$$

where I(Q) is the scattered Intensity and F(Q) is the structure factor of the crystal:

$$F(Q) = \frac{1}{(2\pi)^{3/2}} \int_{\infty} \rho(r) e^{-2\pi Q.r}\, d^3r \qquad (2.16)$$

where $\vec{Q} \equiv \overrightarrow{\mathrm{q_1}} - \overrightarrow{\mathrm{q_o}}$, the difference between the momentum transfer wave vectors of the incident and the diffracted beam respectively with an angle of 2θ between the two momentum transfer vectors [20]. It is worth noting that θ is the angle of incidence of the x-ray beam.

If we define a vector S whose magnitude $|S| \equiv 2\pi Q$, the Fourier transform is written as:

$$F(S) = \Im[\rho(r), S] \equiv \int_{\infty} \rho(r) e^{-2\pi S.r}\, d^3r \qquad (2.17)$$

where $\Im$ is a Fourier transform operator. [21]

2.2.6 Structure Factor of a Real Crystal

When the scattering system is a crystal, the electron density distribution is a periodic function that can be written as a convolution of the electron density distribution of the unit cell, $\rho_{cell}(r)$, and a lattice function, G(r) which is a summation of all δ functions on the lattice points:

$$\rho_{crystal}(r) = \rho_{cell}(r) \otimes G(r) \equiv \int_{\infty} \rho_{cell}(u) * G(r-u) d^3 u \qquad (2.18)$$

where $G(r) = \sum_L \delta(r-L)$.

The vectors L are characterized by $L = l_1 a_1 + l_2 a_2 + l_3 a_3$ in which the l_i are integers and the a_i are base vectors of the lattice. To calculate the Fourier transform of the crystal, $\rho_{crystal}$, we use the generally accepted theorem that the Fourier transform of a convolution of two functions is the product of the transforms of the separate functions. Per this theorem;

If $\Im[f] = F$ and $\Im[l] = L$ then the $\Im[f \otimes l] = F * L$ (2.19)

Since ρ_{cell} has periodic boundary conditions, one can write it as a Fourier series:

$$\rho_{cell}(r) = \frac{1}{V_c} \sum_H F_H \, e^{2\pi i H.r} \qquad (2.20)$$

in which $H = h_1 a_1^* + h_2 a_2^* + h_3 a_3^*$ with a_i representing the base vectors of the reciprocal lattice and h_i are integers. They are related to the basis vectors of the direct lattice by:

$$a_i^* \cdot a_j = \delta_{i,j} \qquad (2.21)$$

V_c corresponds to the volume of the unit cell.

The exponential functions of the Fourier summation are orthonormal and given by:

$$\frac{1}{V_c} \int_{cell} e^{2\pi i H.r} \, e^{-2\pi i H.r} d^3 r = \delta_{H',H} \qquad (2.22)$$

Accordingly, the Fourier coefficients are given by:

$$F_H = \int \rho_{cell}(r) e^{-2\pi i H.r} d^3 r \qquad (2.23)$$

Positions in the unit cell can be expressed with dimensionless fractional coordinates x_i:

$$r = \sum_i x_i\, a_i \tag{2.24}$$

The relation between structure factor and electron density is given by:

$$F_H = V_c \int_0^1 \rho(x) e^{-2\pi i h_i x_i}\, d^3x \Leftrightarrow \rho_{cell}(x) = \frac{1}{V_c} \sum_H F_H\, e^{2\pi i h_i x_i} \tag{2.25}$$

The Fourier transform of the electron density distribution of the unit cell is a continuous function that has the value of the structure factors at the lattice points of the reciprocal lattice:

$$F_{H'} = \Im[\rho(r), H'] = \frac{1}{V_c} \sum_H F_H \int_{cell} e^{-2\pi i H.r}\, e^{-2\pi i H'.r} d^3r = F_{H'} \tag{2.26}$$

To calculate the Fourier transform of the lattice sum $G(r)$, we consider an infinite crystal. In this case the transform is represented by:

$$\Im[G_\infty(r), S] = \sum_L^\infty \int_\infty \delta(r - L) e^{-2\pi i S.r} d^3\, r = \sum_L^\infty e^{-2\pi i S.L} = \frac{1}{V_c} \sum_H^\infty \delta(S - H) \tag{2.27}$$

However, real crystals are finite; hence we multiply $G_\infty(r)$ by the shape function of the crystal and obtain:

$$G(r) = G_\infty(r) * \Omega(r) \tag{2.28}$$

A rectangular crystal for example yields a shape function $\Omega(r) = 1$ for $|x| < a, |y| < b$ and $|z| < c$ and zero everywhere else. The transform in this case is given by:

$$8abc \frac{sin 2\pi S_1 a}{2\pi S_1 a} * \frac{sin 2\pi S_2 b}{2\pi S_2 b} * \frac{sin 2\pi S_3 c}{2\pi S_3 c} \tag{2.29}$$

where S_i are the components of $\boldsymbol{S}$.

The Fourier transform, Λ(S), of the function G (**r**) is then given by the convolution of the sum of δ-functions and the transform of the appropriate shape function. For finite crystals, a distribution about each lattice point is found in reciprocal space, becoming narrow with increasing size of the crystal:

$$\frac{sin 2\pi S a}{\pi S} \Rightarrow \delta(S) \tag{2.20}$$

For $S = 0$, we find $\Lambda(0) = N$, the number of lattice points in the finite crystal. We note here that we are not limited in our choice of unit cell if it yields the total electron density when convoluted with the lattice function $G(r)$. In this sense, we depict our unit cell as the sum of densities of atoms with their nuclei in the unit cell as:

$$\rho_{cell}(r) = \sum_{R_A \epsilon\ cell} \rho_A\,(r - R_A) \qquad (2.21)$$

Using the expression above, we get the expression for the structure factor:

$$F_H = \sum_{R_A \epsilon\ cell} f_A\,(H) e^{-2\pi i H.R_A} \qquad (2.22)$$

with $f_A(H)$ the Fourier transform of the electron density of atom A for $S = H$.

Bibliography

[1] C. Kittel, Introduction to Solid State Physics, 8th ed. (John Wiley & Sons, Inc., 2004).

[2] N. W. Ashcroft and N. D. Mermin, Solid State Physics (Thomson Learning, Inc., 1976).

[3] A. Authier, U. Bonse, R. Feder, W. Graeff, W. Hartmann, S. Kozaki, H. J. Queisser, E. Spiller, and M. Yoshimatsu, X-ray optics: applications to solids, edited by H. J. Queisser (Berlin; New York: Springer-Verlag, 1977).

[4] D. W. Bennett, Understanding single-crystal x-ray crystallography (Weinheim: Wiley-VCH, 2010).

[5] D. Liang, Fundamentals of x-ray crystallography, 2nd ed. (Beijing: Science Press ; Oxford, UK: Alpha Science International, 2011).

[6] G. H. Stout and L. H. Jensen, X-ray structure determination: a practical guide, 2nd ed. (John Wiley & Sons, Ltd, 1989).

[7] B. E.Warren, X-ray Diffraction (Addison-Wesley Publishing Company, Reading, Massachusetts, 1969).

[8] C. Giacovazzo, H. L. Monaco, G. Artioli, D. Viterbo, M. Milanesio, G. Ferraris, G. Gilli, P. Gilli, G. Zanotti, and M. Catti, Fundamentals of Crystallography, 3rd ed., edited by C. Giacovazzo (Oxford University Press, USA, 2011).

[9] C. M. Schlepütz, Systematic Structure Investigation of YBCO Thin Films with Direct Methods and Surface X-ray Diffraction, Ph.D. thesis, Mathematisch naturwissenschaftliche Fakultät, Universität Zürich (2009), doi: 10.6084/m9.figshare. 942424.

[10] I. K. Robinson, "Crystal truncation rods and surface roughness," Phys. Rev. B 33, 3830 (1986).

[11] I. K. Robinson and D. J. Tweet, “Surface X-ray diffraction,” Rep. Prog. Phys. 55, 599 (1992).

[12] E. Vlieg, J. V. D. Veen, S. Gurman, C. Norris, and J. Macdonald, “X-ray diffraction from rough, relaxed and reconstructed surfaces,” Surf. Sci. 210, 301 (1989).

[13] S. K. Sinha, E. B. Sirota, S. Garoff, and H. B. Stanley, “X-ray and neutron scattering from rough surfaces,” Phys. Rev. B 38, 2297 (1988).

[14] J. D. Jackson, Classical Electrodynamics, 3rd ed. (JohnWiley & Sons, Inc., 1999).

[15] P. Willmott, An Introduction to Synchrotron Radiation: Techniques and Applications (John Wiley & Sons, Ltd., 2011).

[16] E. Prince (Editor): International Tables for Crystallography, Vol. C, Mathematical, physical and chemical tables. International Union of Crystallography, Chester, online edition (2006).

[17] R. W. James, "The optical principles of the diffraction of X-rays", Bell, London (1965)

[18] D. Feil, Isr. J. Chem. 16, (1977), 149

[19] O. K. Ersoy, Diffraction, Fourier Optics and Imaging (John Wiley & Sons, Inc.,

[20] This choice of the sign of the exponent is consistent with the quantum theory of diffraction: D. Feil, Isr. J. Chem. 16, (1977), 149 J. J. Sakurai, Advanced Quantum Mechanics, Addison Wesley, Reading MA., USA, (1967)

[21] G. B. Arfken and H. J. Weber, Mathematical Methods for Physicists 6th ed. (Elsevier Inc., 2005). 2007).

CHAPTER III

Investigated Materials

3.1 Zinc Tin Nitride ($ZnSnN_2$) Thin Films

3.1.1 Introduction

In heterovalent ternary compounds (HTCs) [1] the cation or anion sublattice of a wurtzite or zincblende binary semiconductor is replaced by an ordered sublattice of two different atom types such that the average number of valence electrons stays the same. Crystallographically, the structure of these materials evolves from the tetrahedral diamond structure with the Group V atom surrounded by two Group II and two Group IV atoms and the Group II or IV atom surrounded by four Group V atoms tetrahedrally with covalent atomic bonding. The transfer from III-V to heterovalent II-IV-V_2 compounds brings about interesting and potentially useful differences in optical and electrical properties in comparison to the binaries. Because of the reduced symmetry due to superlattice formation, heterovalent ternary semiconductors can have high nonlinear optical coefficients [2]. Their more complicated lattices also offer opportunities for doping strategies, and defect and band structure engineering [2]. Furthermore, the degree of ordering on the cation sublattice can be used as a tuning parameter since it can change the optical properties, vibrational properties, and lattice parameters of the material. For example, one experimental report found that the band gap of $ZnSnP_2$ changed by 0.3 eV when the ordering parameter was changed [3]. In that study chalcopyrite ordering was confirmed by the appearance of sphalerite-disallowed superstructure reflections. Chalcopyrite II-IV arsenide and II-IV phosphide compounds are relatively extensively investigated in search of superior thermoelectric and non-linear optic materials [4]. An outstanding achievement in chalcopyrite research is the nonlinear optical applications of $ZnGeP_2$ and $CdGeAs_2$ [4]. The research on Il-IV-N_2 films has been hampered by the need for high temperature and pressure for synthesis [5,6] leading to the growth of mostly polycrystalline films. Table 3.1 shows experimental lattice parameter values for $ZnSnN_2$ obtained by various groups.

Table 3.1: Experimentally determined lattice constants for $ZnSnN_2$ films

Structure	a (Å)	b (Å)	c (Å)
Wurtzite [18]	3.395	3.4	5.434
Wurtzite [17]	3.375(1)	3.376(1)	5.532(3)
Wurtzite [17]	3.383(4)	3.379(3)	5.567(6)
Orthorhombic [12]	5.842(7)	6.753(6)	5.462(3)

The goal of this thesis is therefore an exploration of single crystalline $ZnSnN_2$ films, composed entirely of earth abundant elements. We perform structural characterization via synchrotron x-ray diffraction techniques to validate both the theoretically predicted wurtzite and orthorhombic structural phases in single crystalline films and to study the effect of molecular beam epitaxy growth and processing conditions on the ordering of the $ZnSnN_2$ cation sublattice. The hope is that the trends shown here may guide the understanding of the synthesis and characterization of $ZnSnN_2$ films and pave a way for achieving superior optoelectronic properties suitable for use in electronic devices.

3.1.2 Ordering Phenomena in $ZnSnN_2$

The nature of disorder in the heterovalent ternary semiconductors and in particular $ZnSnN_2$ films, is of both fundamental and practical interest but it is not yet well understood. One model for disorder assumes the random placement of atoms on the mixed cation sublattice. In this model, there are varied instances where local charge neutrality is destroyed and the so- called octet rule is violated [7]. These defects disrupt the electronic structure of the material, sometimes substantially reducing the bandgap. For example, a recent theoretical study on $ZnSnN_2$ by Veal et. al, predicts that random placement of Zn and Sn atoms on the cation sublattice shrinks the band gap from 2.18 eV in the cation ordered orthorhombic $Pna2_1$ structure to 1.12eV in the cation disordered wurtzite structure [8] as shown in Figure 3.1.

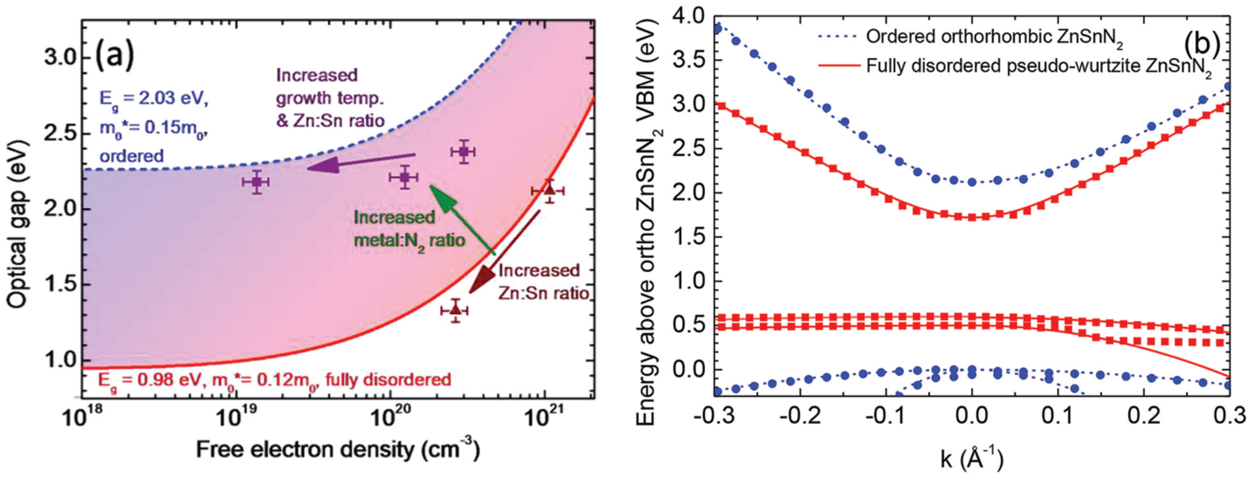

Figure 3.1: a) Optical absorption edge versus free electron density for $ZnSnN_2$ films. b) DFT band structure and k.p fitting for cation ordered orthorhombic and SQS cation disordered pseudo wurtzite $ZnSnN_2$. Figure reprinted from [8]

Quayle et al. also reported that in the $Pm3_1$ space group, where each nitrogen atom is bound to either three Zn atoms and one Sn atom, the band gap disappears completely. [9] This structure, of course, consists entirely of octet rule violations. There is another model for disorder on the cation sublattice that does not produce octet rule violations. In $ZnSnN_2$ and other wurtzite- based heterovalent ternary semiconductors, there are two ways of ordering the cation lattice that preserve the octet rule. One configuration has the space group $Pna2_1$, shown in Figure 3.2. The orthorhombic unit cell has sixteen atoms while the wurtzite unit cell has four [10] with a structural relationship as follows:

$$a_o = 2a_w;\ b_o = \sqrt{3}a_w;\ c_o = c_w$$

Another model of ordering has the $Pmc2_1$ space group and an eight-atom unit cell [11].

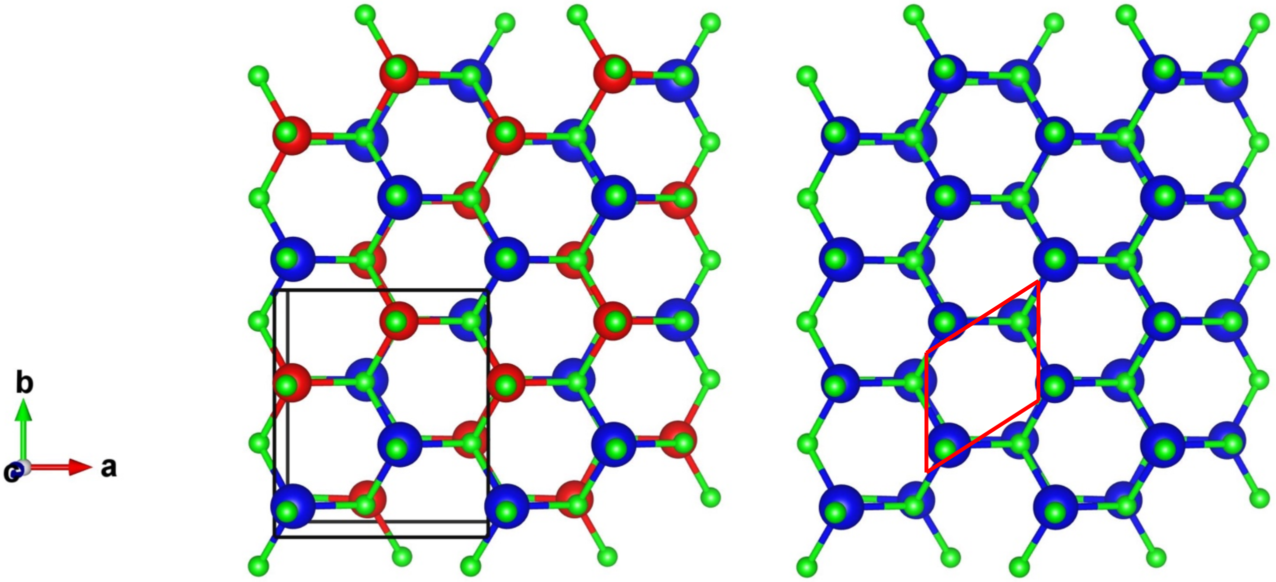

Figure 3.2: a) The unit cell of the orthorhombic $Pna2_1$ structure of $ZnSnN_2$. Green spheres are nitrogen atoms; red spheres are tin and blue spheres are zinc. b) The unit cell of the wurtzite structure of $ZnSnN_2$. Zn and Sn are random and represented by the same color-blue. Unit cells are outlined.

Quayle et al. have proposed another model of disorder that involves randomly stacking $Pna2_1$ and $Pmc2_1$ layers in the crystal's y direction, without producing any octet-rule violations [9]. This alternative model of cation disorder could explain why $ZnSnN_2$ films grown by Quayle et al. are observed to be wurtzite, as evidenced by XRD, but also have a band gap, measured by photoluminescence excitation spectroscopy and by photoluminescence spectroscopy, that is consistent with that predicted for perfectly ordered $ZnSnN_2$ [9, 12]. Similarly, there are two ways of ordering zincblende-based heterovalent ternary compounds, and a similar model of disorder has been presented for these materials [13,14].

A recent study of ordering in polycrystalline $ZnGeN_2$ films [15] found that the degree of ordering from disordered, wurtzite-like x-ray diffraction spectra to orthorhombic, with space group $Pna2_1$, increased with increasing growth temperature, as evidenced by the appearance of superstructure peaks and peak splitting in the diffraction patterns. Annealing disordered, low-temperature-grown $ZnGeN_2$ at 850 °C, however, resulted in increased cation ordering. Growth of $ZnGeN_2$ on a liquid Sn-Ge-Zn alloy at 758 °C also showed an increase in the tendency for cation ordering at a lower growth temperature. A recent study on the effect of varying growth conditions on band gap tuning showed band gap variation from 1.33 to 2.38 eV. As depicted in Figure 3.3

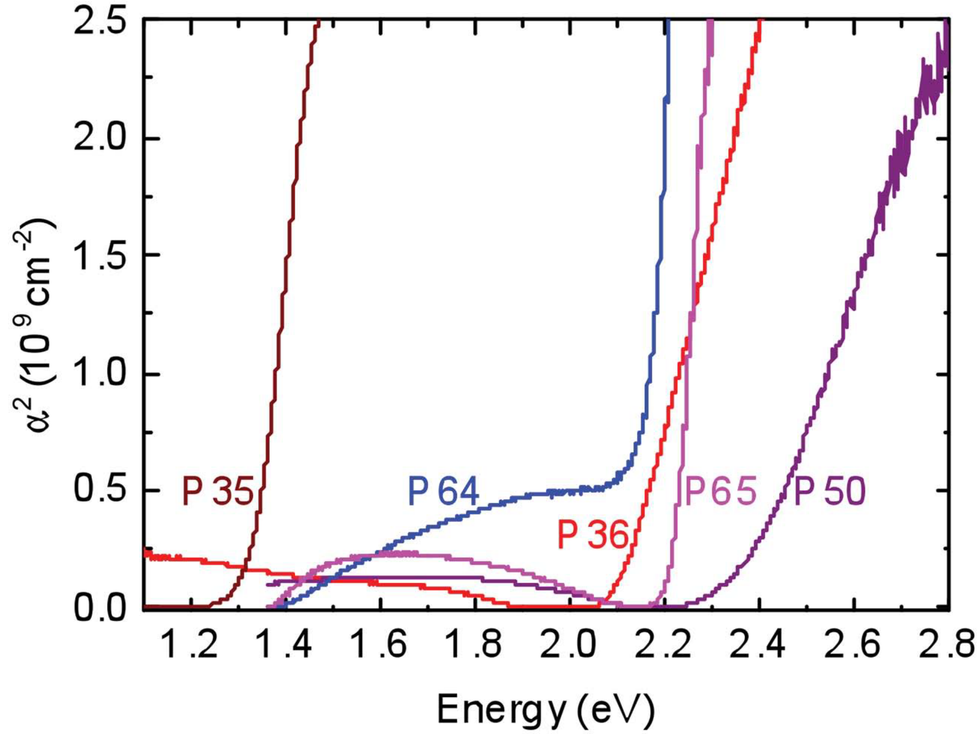

Figure 3.3: Optical absorption spectra from $ZnSnN_2$ films grown under different MBE conditions. Figure reprinted from [8]

The films in this study with growth conditions shown in Table 3.2 were grown using plasma assisted molecular beam epitaxy, a non-equilibrium growth technique where the substrate temperature and Zn: Sn flux ratio have a profound influence on how atoms incorporate into an epitaxially driven crystal system. It is therefore expected that higher growth temperature is likely to produce a more ordered film than a lower growth temperature since kinetic processes dominate low temperature MBE as previously observed for the related material $ZnSnP_2$. [16]

Table 3.2: MBE growth conditions and bandgap values for $ZnSnN_2$ films. Data taken from [8]

Sample	Growth temperature [°C]	Zn: Sn flux ratio	N_2 pressure [Torr]	Optical gap [eV]	Free electron density, n [cm^{-3}]
P35	400	39	2×10^{-5}	1.33	2.7×10^{20}
P36	400	36	2×10^{-5}	2.12	1.1×10^{21}
P50	400	36	1×10^{-5}	2.38	3.0×10^{20}
P64	500	55	1×10^{-5}	2.18	1.4×10^{19}
P65	450	55	1×10^{-5}	2.21	1.2×10^{20}

Based on this background, the $ZnSnN_2$ films in this study were carefully studied to determine the crystal structure of as grown films and thereafter, disordered wurtzite films were subjected to annealing at high temperatures to determine whether a structural phase transition from the wurtzite to orthorhombic phase was possible. This phase transition is directly linked to the variation from a disordered to an ordered cation sublattice and is important for tuning of optical and electrical material properties in $ZnSnN_2$ films that have direct consequences to the viability of this material for use in optoelectronic applications.

3.1.3 Spontaneous Polarization in $ZnSnN_2$

II-IV-N_2 materials like the group III nitrides are polar materials, which indicates that they can exhibit spontaneous polarization. In III nitrides for example, spontaneous polarization has played a critical role leading to surface charge density at the interface between two nitrides. This leads to an electric field in quantum wells made of different III-N semiconductors. The electric field is used to provide confinement in a two-dimensional electron gas at the heterojunction. On the other hand, this spontaneous polarization can have detrimental effects as in optoelectronic devices causing the separation of electrons and holes hence reducing the overlap of their wave functions and the optical oscillator strength of excitons. The spontaneous polarization values of Zn-IV-N_2 and III-N materials are shown in Table 3.3.

Table 3.3: Spontaneous polarizations in III nitrides and Zn-IV-N_2 materials.

Material	Polarization (C/m2)
[a]GaN	-0.029
[a]InN	-0.042
[a]AlN	-0.090
[b]$ZnSiN_2$	-0.022
[b]$ZnGeN_2$	-0.023
[b]$ZnSnN_2$	-0.029

[a] Data taken from [19]
[b] Data taken from [20]

3.2 Sample Growth and Characterization

The structural studies on $ZnSnN_2$ (ZSN) films grown on Lithium gallate (LGO) and Yttria stabilized zirconia (YSZ) substrates were carried out in collaboration with the Durbin group at Western Michigan University. All the $ZnSnN_2$ films used in this project were either grown at University at Buffalo, The State University of New York or at Western Michigan University.

Single-crystal thin films of $ZnSnN_2$ were grown on (001) LGO and (111) YSZ substrates, which were cleaned prior to growth via a standard three-step solvent cleaning sequence consisting of trichloroethane, acetone, and methanol. The films were grown in a Perkin Elmer 430 molecular beam epitaxy (MBE) system using conventional effusion cells for Zn and Sn evaporation; the Zn and Sn fluxes were measured using a quartz crystal microbalance. Active nitrogen was created using an Oxford Applied Research HD25 inductively-coupled RF plasma source equipped with a 256-hole aperture plate, with electrostatic ion removal. The film growth was monitored In situ using a 20 kV Staib Instruments reflection high-energy electron diffraction (RHEED) system along with a KSA 400 image acquisition and analysis package. Ex-situ experiments included x-ray diffraction and transmission electron microscopy. The substrate temperature, Zn: Sn flux ratio and the N_2 pressure were adjusted to vary the degree of cation disorder in the $ZnSnN_2$ films to experimentally test the theoretical predictions.

Structural characterization involved unit cell refinement to determine the film crystal structure and 3D reciprocal space map reconstruction was employed to determine the exact symmetry of the film unit cell. Annealing measurements were done to determine the possibility of a structural phase transition from the wurtzite to the orthorhombic phase and obtain the exact temperature at the transition. Transmission electron microscopy measurements were performed to determine the film morphology and structure. All x-ray diffraction experiments were carried out at the Advanced Photon Source (APS), Argonne National Laboratory (ANL) at sectors 13BMC, 33IDD and 33BMC while annealing was done both at APS and in the clean room on the University of Michigan North Campus complex. TEM measurements were performed at the Michigan Center for Material Characterization.

Bibliography

[1] C.H.L. Goodman, Nature, 179, 828 (1975).

[2] W. R. L. Lambrecht, A. Punya, Heterovalent ternary II-IV-N2 compounds: perspectives for a new class of wide-band-gap nitrides, in: B. Gill (Ed.), III-Nitride Semiconductors and their Modern Devices, Oxford University Press, 2013, pp. 519{585. doi:10.1093/acprof:oso/9780199681723.001.0001.

[3] P. St-Jean, G. Seryogin, S. Francoeur, Band gap of sphalerite and chalcopyrite phases of epitaxial znsnp2, Applied Physics Letters 96 (23) (2010) 231913.

[4] J.L. Shay and J.H. Wernick, Ternary Chalcopyrite Semiconductors: Growth, Electronic Properties, and Applications, Pergamon Press, 1975.

[5] M. Maunaye et J. Lang, Mater. Res. Bull., 5, 793 (1970).

[6] T. Endo, Y. Sato, H. Takizawa, M. Shimada, J. Mater. Sci. Lett., 11, 424 (1992).

[7] M. Buerger, The temperature-structure-composition behavior of certain crystals, Proc. Natl. Acad. Sci. 20 (1934) 444.

[8] T. D. Veal, N. Feldberg, N. F. Quackenbush, W. M. Linhart, D. O. Scanlon, L. F. Piper, S. M. Durbin, Band gap dependence on cation disorder in $ZnSnN_2$ solar absorber, Advanced Energy Materials 5 (24).

[9] P. C. Quayle, E. W. Blanton, A. Punya, G. T. Junno, K. He, L. Han, H. Zhao, J. Shan, W. R. L. Lambrecht, K. Kash, Charge-neutral disorder and polytypes in heterovalent wurtzite-based ternary semiconductors: The importance of the octet rule, Phys. Rev. B 91 (2015) 205207. doi:10.1103/PhysRevB.91.205207. URL http://link.aps.org/doi/10.1103/PhysRevB.91.205207

[10] A. Punya, W. R. L. Lambrecht, M. van Schilfgaarde, Quasiparticle band structure of zn iv-n2 compounds, Phys. Rev. B 84 (2011) 165204. doi:10.1103/PhysRevB.84.165204. URL http://link.aps.org/doi/10.1103/ PhysRevB.84.165204

[11] L. Garbato, F. Ledda, A. Rucci, Structural distortions and polymorphic behavior in abc 2 and ab 2 c 4 tetrahedral compounds, Progress in crystal growth and characterization 15 (1) (1987) 1{41.

[12] P. C. Quayle, K. He, J. Shan, K. Kash, Synthesis, lattice structure, and band gap of $ZnSnN_2$, MRS Communications 3 (03) (2013) 135{138.

[13] S.-H.Wei, L. . G. Ferreira, A. Zunger, First-principles calculation of the order-disorder transition in chalcopyrite semiconductors, Physical Review B 45 (5) (1992) 2533.

[14] S.-H. Wei, S. Zhang, A. Zunger, Band structure and stability of zinc-blende-based semiconductor polytypes, Physical Review B 59 (4) (1999) R2478.

[15] Eric W. Blanton, Keliang He, Jie Shan, Kathleen Kash, Characterization and control of ZnGeN2 cation lattice ordering, arXiv:1610.03512 [cond-mat.mtrl-sci]

[16] S. Francoeur, G. A. Seryogin , S. A. Nikishin , H. Temkin , Appl. Phys. Lett. 2000, 76 , 2017 .

[17] Feldberg, N., et al., Growth, disorder, and physical properties of ZnSnN2. Applied Physics Letters, 2013. 103(4): p. 042109.

[18] Feldberg, N., et al., ZnSnN2 A New Earth-Abundant Element Semiconductor for Solar Cells. Proc. of the 38th IEEE Photovoltaic Specialists Conference, 2012: p. 2524-2527.

[19] Fabio Bernardini, Vincenzo Fiorentini and David Vanderbilt. Spontaneous polarization and piezoelectric constants of III-V nitrides. Phys. Rev. B,56(16):R10024-R10027, Oct 1997.

[20] Tula R. Paudel and Walter R. L. Lambrecht, First-principles calculations of elasticity, polarization-related properties, and nonlinear optical coefficients in Zn-IV-N2 compounds, PHYSICAL REVIEW B 79, 245205 2009, DOI: 10.1103/PhysRevB.79.245205

CHAPTER IV

Experimental Setup and Analysis Methodology

4.1 Introduction

In this chapter, we shall discuss the experimental setup used for the acquisition of structural data in synchrotron x-ray scattering experiments. The analytical methodology for acquired data will also be introduced. An overview of the synchrotron x-ray sources and beamline optics will be discussed in section 4.1 as well as the techniques used for sample alignment at the beam line. This will be followed by an account of the data acquisition techniques for x-ray diffraction and 3D-reciprocal space maps (RSMs) and post beam time data analysis involving 3D-RSM reconstruction from area detector measurements and calculations.

4.2 Experimental Setup

4.2.1 Synchrotron X-ray Sources

Synchrotron radiation is electromagnetic radiation emitted by electrons moving at relativistic velocities that are forced to change the direction of their motion under the effect of applied magnetic fields (perpendicular to the direction of their motion) along a curved trajectory. Due to the large radius of curvature of this trajectory, quantum effects are negligible. The unique characteristics of synchrotron radiation, particularly its spectral distribution as shown in Table 4.1, have made it a very powerful tool for investigating the properties of matter in several fields such as molecular and atomic physics, chemistry, engineering, technology, biology and medical science. A typical electron accelerator emits synchrotron radiation in a broad spectrum of photon energies ranging from microwave to hard x-rays, and wavelengths ranging from 10^3 to 10^{-1} Å. Note that the sizes of atoms and molecules fall in the same range as do the lengths of chemical bonds and inter-planar spacing within crystal lattices, hence the photons generated by synchrotron sources have the optimum wavelength for studying the atomic structure of solids and molecules. Some of the other advantages of synchrotron radiation are the high intensity photon beam that allows rapid experiments and the use of weakly scattering crystals, a highly collimated beam that is generated by a small divergence and is spatially coherent, high stability, both linear and circular polarization and a pulsed time structure. Three generations of synchrotron radiation have been developed over time and recently the fourth generation based on free electron lasers and a very long undulator in a high-energy electron linear accelerator has been developed. This free electron laser source has a peak brightness many orders of magnitude beyond that of the third- generation sources, as well as pulse lengths of 100 fs or shorter, and is fully coherent.

Table 4.1: Spectral Ranges Covered by Synchrotron Radiation

Photon Energy, hν (eV)	**Photon Wavelength, λ (Å)**	**Spectral Range**
$10^{-2} – 1.8$	$10^6 – 7 \times 10^3$	Infrared
$1.8 – 3.1$	$7 \times 10^3 – 4 \times 10^3$	Visible
$3.1 – 40$	$4 \times 10^3 – 3.1 \times 10^2$	Ultraviolet
$40 – 1.5\times 10^3$	3.1×10^2 - 8	Soft x-rays
1.5×10^3 - 10^5	8 – 0.1	Hard x-rays

The major components of the synchrotron storage ring are:

1) The injection system which generates electrons from a hot cathode (~ 1100° C), accelerates them to hundreds of millions of electrons volts' energy using a linear accelerator and then injects them into a vacuum chamber.
2) The vacuum chamber which is a metal tube in which the electrons circulate along a closed trajectory under ultra-high vacuum at pressures of $10^{-10} – 10^{-11}$ Torr.

3) The radio frequency cavity system which periodically acts on the circulating electrons and restores the energy they lose because of the emission of synchrotron radiation.
4) The dipole bending magnets which bend the trajectory of the electrons and force them to circulate in a closed orbit inside the vacuum chamber of the storage ring.
5) The insertion devices which consist of periodic arrays of magnets that modify the trajectory of the electrons in straight sections of the storage ring. This modification of the trajectory of electrons in straight sections of the ring results in highly intense radiation with minimized divergence.
6) The control systems which include one or more computers that monitor the status of the storage ring components and automatically make the necessary adjustments for the different phases of operation.
7) The radiation shielding system which plays the critical role of shielding users and staff in the facility from dangerous neutron and gamma radiation.

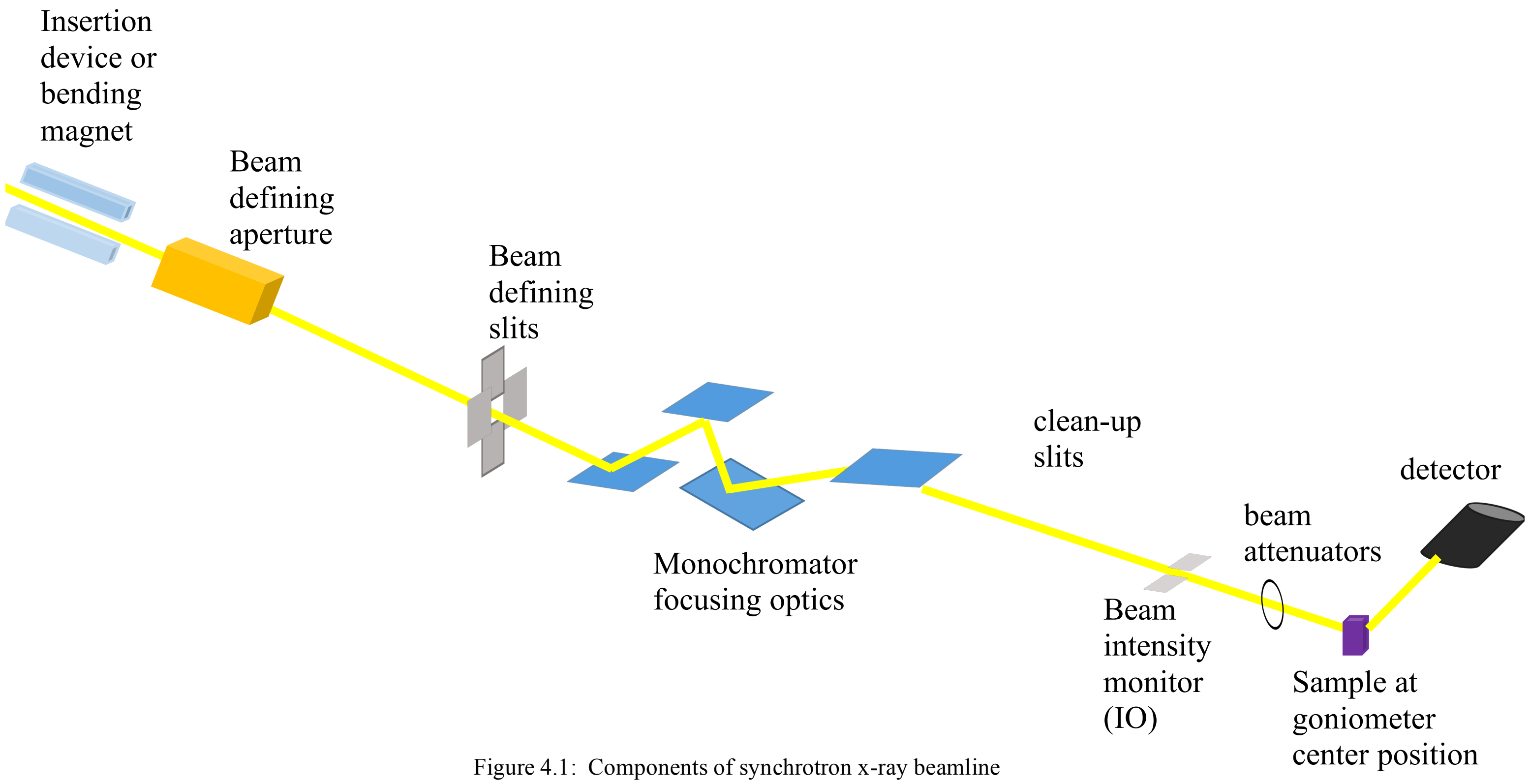

Figure 4.1: Components of synchrotron x-ray beamline

4.2.2 Beamline Optics

The beamline optics play the critical role of conveying the radiation emitted by the bending magnets and insertion devices to the user's experimental chamber. A layout of the beamline optics at a typical synchrotron is shown in Figure 4.1 above.

The user can also conveniently select a unique energy required for each experiment. The major components of the beamline are:

1) The monochromator which selects the desired photon energy by eliminating photons of all energies except those in a narrow band centered around the desired value.
2) The vacuum system which keeps the pressure in the beam line at levels compatible with its connection to the vacuum chamber of the storage ring.

3) The mirrors which focus and refocus the radiation along the beamline preserving the high optical quality of the photon beam.
4) Beamline control system operates the monochromator and monitors the status of the vacuum system
5) Filters, collimators, beam stoppers are all necessary for the reliable operation of the beamline.
6) The experimental chambers which are each designed for a specific line of experiments and equipped with their own data acquisition system.

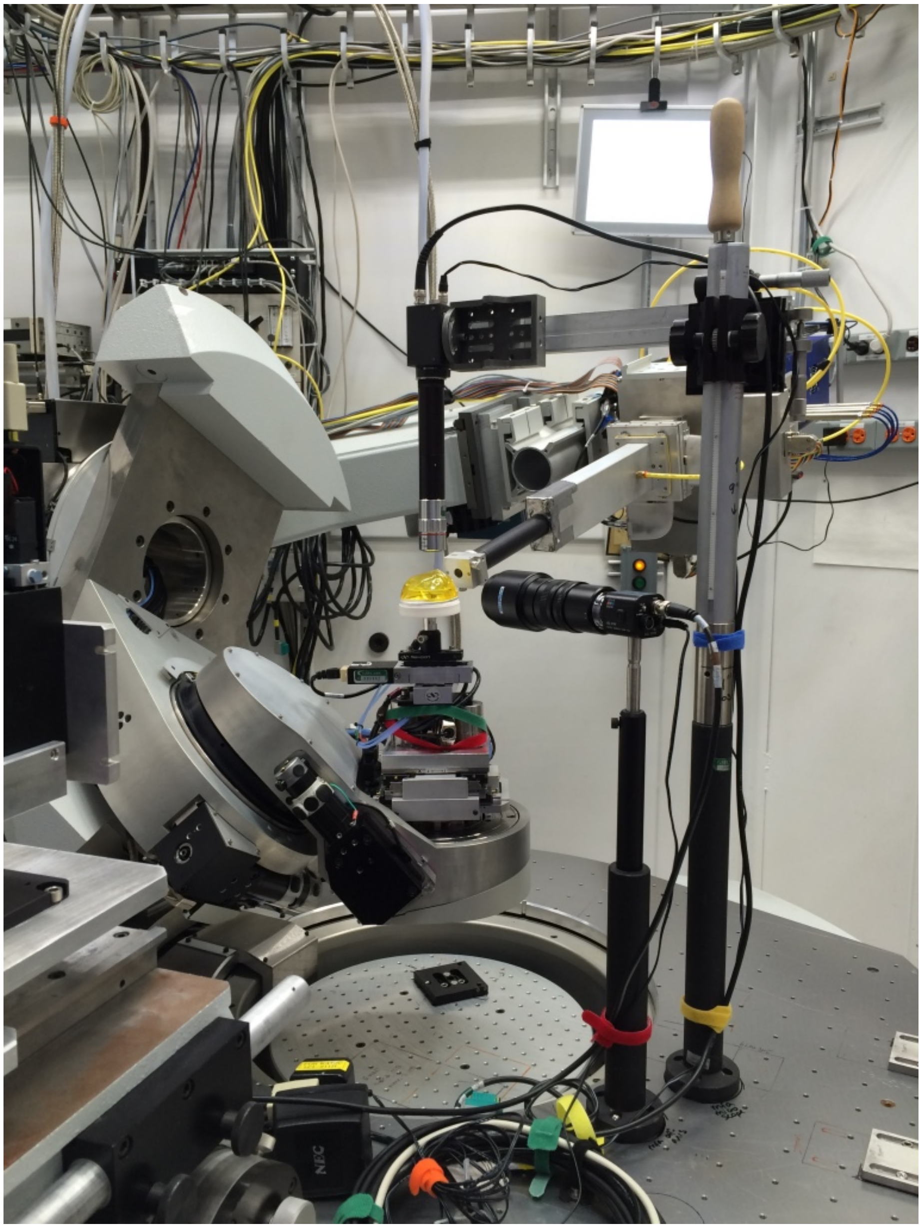

Figure 4.2: x-ray scattering beamline optics at sector 13BMC, Argonne National Laboratory

4.2.3 Detectors

The large variations in intensities recorded during x-ray scattering experiments greatly influences the detector requirements. To deal with the signals spanning several orders of magnitude in intensity, a large detector dynamic range is needed, in conjunction with excellent linearity. For one, the detector dead time should be high enough to account for the maximum count rate for strong signals. On the other hand, long exposure times are required for low signal intensities between strong Bragg peaks which strongly limits the acceptable amount of readout noise in the data and requires a good detector stability.

Point detectors have traditionally been used in x-ray scattering experiments and have offered many advantages including being very simple to operate and being light weight thus enabling high precision movements of the diffractometers. The drawback with point detectors though is that each measurement only provides a single intensity measurement making for very slow data acquisition since each detector position must be scanned to get meaningful diffraction features. To counter the slow data acquisition encountered when using point detectors, area detectors with extended peripheral vision have been employed. In this regard, 2D detectors have recently been developed to enhance the amount of information to be obtained from a single measurement [1].

PILATUS pixel detectors were first developed at the Paul Scherrer Institut in Switzerland to meet the stringent requirements of high-resolution protein crystallography [2, 3]. These detectors have an active area of 83.8×33.5 mm^2, consisting of a single monolithic silicon sensor bump-bonded to an array of 8×2 CMOS readout chips, comprising a total of $487 \times 195 = 94\,965$ pixels with 172×172 μm^2 pitch. The PILATUS detectors also employ single photon counting technology which essentially means that in principle they can perform a direct conversion of the x-rays incident on the detector to counts. This process is noise-free (no leakage currents, readout noise, etc.). Counter dead times ranging from 100 to 400 ns allow for maximum count rates of up to 2×10^6 photons/second/pixel. The readout time for the entire module is approximately 3.6 ms and frame rates up to 200 Hz can be achieved for single module detectors. These detectors can be used in experiments with energy requirements ranging anywhere from 3 to 40 keV with reasonable efficiency values attained.

All experiments in the framework of this thesis were performed using the PILATUS 100k single module detector. The reader who is interested in further details on PILATUS detectors can find it in the literature [2-5].

4.2.4 Sample Alignment for Single Crystal Diffraction Experiments

After going through all the beamline optics including monochromators, mirrors, and slits, a properly shaped and well-focused beam can be obtained. The beam and diffractometer positions are adjusted such that the beam goes through the origin of all diffractometer axes, and the beam propagation direction is parallel to the diffractometer y axis as shown in Figure 4.3. The experiments in this dissertation were performed at Sectors 13-BM-C, 33-BM-C, and 33-ID-D at the Advanced Photon Source, Argonne National Laboratory, USA. Sectors 13-BM-C and 33-ID-D are equipped with Newport 6- circle diffractometers using a kappa geometry [6], and sector 33-BM-C is equipped with a Huber 4-circle diffractometer with a Eulerian geometry [7].

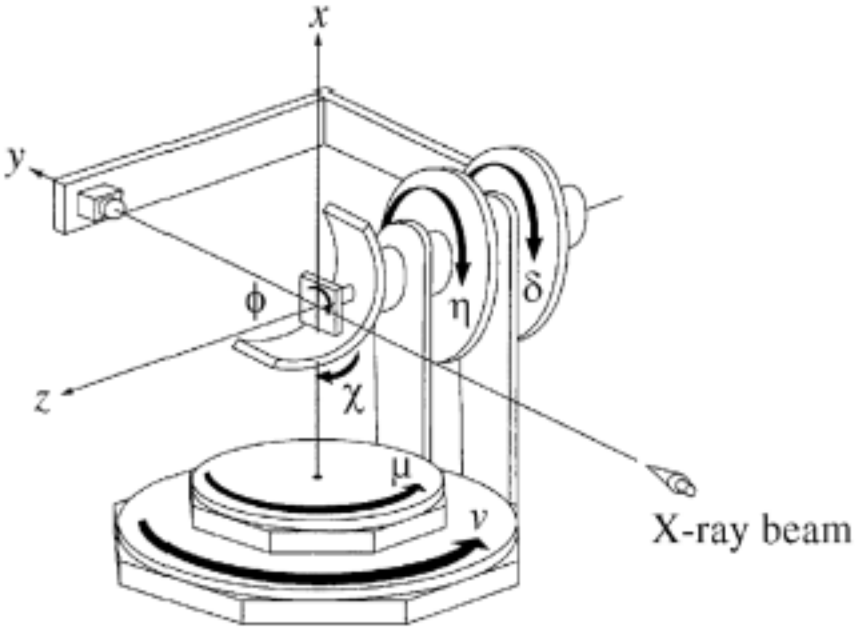

Figure 4.3: 6 circle diffractometer axes with all angles at their respective zero positions. Reprinted from [3] with permission (1999, International Union of Crystallography).

The investigated samples typically have a surface area of 2×2 to 5×5 mm^2 and a thickness of about 100nm. The samples are mounted on the diffractometer using brass pins glued to the back side of the sample with beeswax or silver paint. At the zero position of the diffractometer (Figure 4.3), the optical surface of the sample can be aligned perpendicular to the z axis of the diffractometer using a laser reflection. This is done by shining a laser beam on the sample surface, the rotation stage of the goniometer head or chi and phi angles (when using 6-circle diffractometer) can be adjusted until the laser reflection is stationary through a 180° rotation of the sample about the z axis. Once the sample surface is aligned, the sample is placed at the diffractometer center using sample translation stages (x and y). The monitoring of the diffractometer and sample positions during the experiment is usually done by cameras. The diffractometer center position for example is marked on the monitor screen, so that the adjustments for lateral position of the sample can be easily done by simply moving the sample to the marked diffractometer center position while monitoring the camera image. Lining up the optical surface of the sample with respect to the diffractometer center makes the optical surface of the sample parallel to the incoming x-ray beam propagation direction. The next step is to adjust the z height of the sample with respect to the surface normal direction until the sample surface lies at the diffractometer center. This step is important because diffractometer angle calculations assume that x-ray scattering occurs exactly at the diffractometer center and the incoming x-ray beam goes through the diffractometer center as well. In adjusting the z height of the sample, we aim to cut the x-ray beam in half when the sample surface is at the diffractometer center.

Last in the sample alignment procedure is finding the sample orientation matrix. Here, the unique directions of the sample crystallographic axes (a, b, and c) are found with respect to a known single crystal substrate. Once the orientation matrix is obtained, the diffractometer angles for any arbitrary reciprocal space position can be calculated. Note that the alignment procedure described above and all the data acquisition measurements are performed using a software called SPEC [8] as are the beam line components including the PILATUS area detector and the diffractometer.

4.3 $ZnSnN_2$ Measurements and Analysis

The symmetry of the diffraction pattern from a crystal is a good indication of the unit-cell symmetry of a crystal. By qualitatively examining the peak absences and the presence of various Bragg peaks with their corresponding diffraction patterns, the unit cell symmetry within a crystal can be obtained. The 3D-RSMs technique has been widely employed for the structural characterization of single crystal films and mixed phase polymorphs in thin films because it allows one to display the diffraction pattern in any direction in 3D reciprocal space. The RSMs can be efficiently measured at synchrotrons with the fast data acquisition process provided by current generation single photon counting area detectors. The conversion of pixel coordinates in the detector images taken during the experiment to momentum transfer coordinates is not trivial [9]. It is further complicated by the three reference geometries in the x-ray diffraction system: laboratory, detector, and sample. The laboratory coordinate system is the reference coordinate system. The sample coordinate system shares the same origin with the laboratory system but its basis can be oriented in a different way and the detector coordinates system is a two-dimensional system tied to the workings of the detector. All the systems are represented in the orthogonal Cartesian basis [10-13]. Data collection using an area detector means that each detector image represents a two-dimensional slice of reciprocal space hence any angular scan contains 3-dimensional information as a set of two-dimensional reciprocal space slices. The 2D reciprocal space slices are converted into 3D volumes by using fast gridding algorithms and eventually mapped onto a rectangular grid for easier data interpretation.

4.3.1 3D-RSM Measurements

The Pilatus 100k area detector is used to measure the intensity distribution around each peak in a series of single scans along the L-direction, or as rocking scans around the azimuthal rotation axis of the sample surface, or by a combination of these two. In this work, we employed both the '3D+1S' and '4D+2S' diffractometer geometries for reciprocal space map acquisition. 3D and 4D here mean three and four diffractometer circles used for detector orientation or moving the detector across the Ewald sphere respectively while 1S and 2S mean one and two sample geometries needed for orientation respectively. The 3D volume of a crystal can be sampled in three ways shown in Figure 4.4: rocking scans where the detector is kept stationery and the sample is rocked about its azimuth, detector scan in which the sample is kept stationery and the detector scans the Ewald sphere or the 2θ-ω scan where the detector and sample orientations are coupled. Figure 4.5 shows how the 3D-volume in reciprocal space can be sampled during a rocking scan with an area detector.

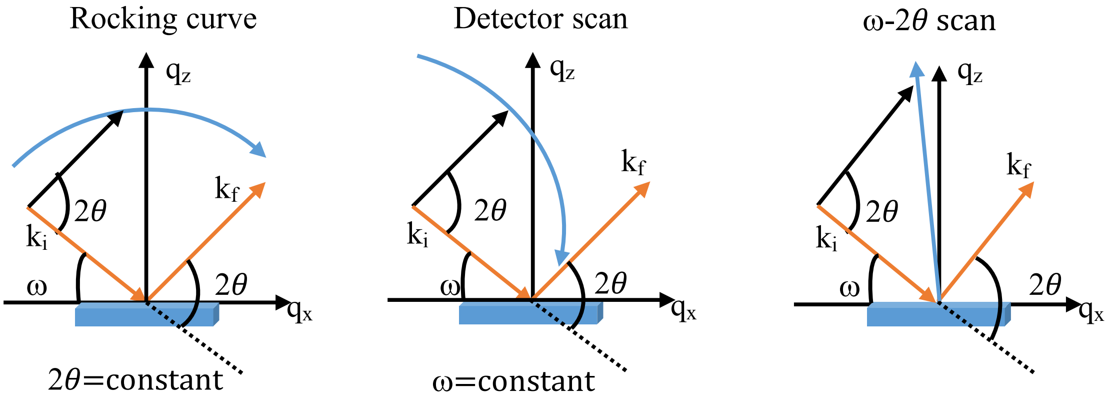

Figure 4.4: Examples of scans used to collect data at x-ray diffraction beamline

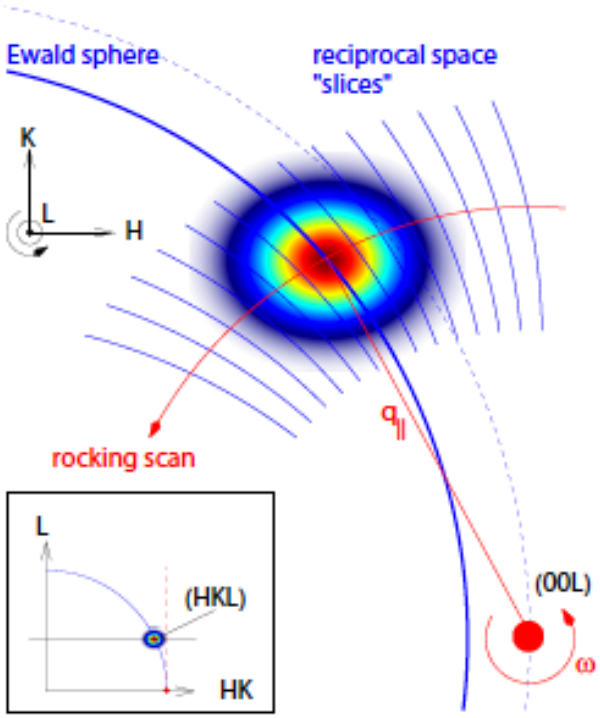

Figure 4.5: The 3-dimensional reciprocal space volume can be sampled by a single rocking scan with an area detector. Figure courtesy of Dr. Christian M. Schlepütz, Paul Scherrer Institut

The angular range required for capturing the reciprocal space volume at a given HKL position varies from Bragg peak to Bragg peak and therefore the scan range for each peak must be carefully assessed before taking a scan measurement to prevent the risk of recording incomplete data.

4.3.2 Reciprocal Space Volume Reconstruction

Detector images recorded by Pilatus during the various scans discussed in section 4.2.1 above contain diffractometer angular information. This angular information together with the intensity data needs to be converted to intensities in a 3D reciprocal space volume. The angular position of each pixel in diffractometer coordinates can be converted to a unique reciprocal space position [14]. The reciprocal space volume obtained from the scan is an irregular grid of reciprocal space coordinates and intensity values because the relationship between the diffractometer coordinate system and reciprocal space is non-linear. This irregular grid is interpolated to a rectangular grid so that it can be properly displayed as a map. Figure 4.6 describes an algorithm developed by Dr. Christian M. Schlepütz for converting the irregular grid intensity data to regular grid data.

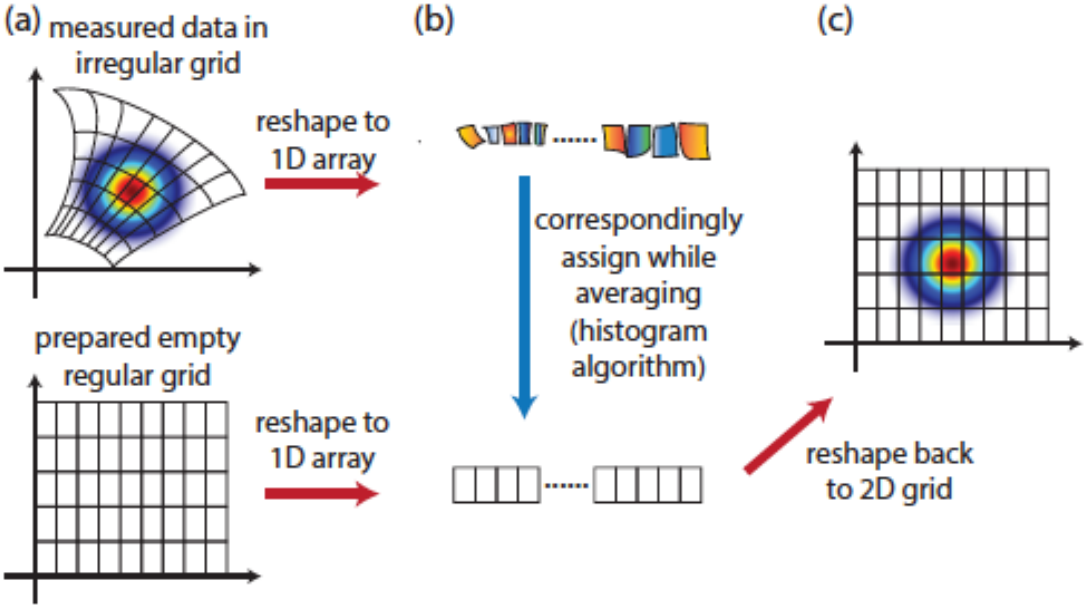

Figure 4.6: Typical procedure for reciprocal space reconstruction. (a) Measured intensity data on an irregular grid of reciprocal space and an empty rectangular grid. (b) Interpolation procedure employing a histogram algorithm. (c) Interpolated intensity data on the rectangular grid. Figure reprinted from [15]

First, an empty rectangular grid slightly larger than the irregular grid, is prepared for storing the intensity data [Figure 4.6 (a)]. The size of each voxel is arbitrarily determined depending on the desired resolution of the RSM but the regular grid voxel size should be larger than the largest voxel in the irregular grid to prevent the occurrence of empty voxels in the reconstructed intensity map. Next, the irregular intensity grid and the regular empty grid are converted to 1D arrays with the proper indices assigned to each array element. The indices are determined such that they represent the reciprocal space positions of the original voxels. A fast histogram algorithm is used to assign the intensity value of each element in the irregular 1D array to an element of the regular 1D array with the corresponding reciprocal space index. The desired 3D reciprocal space volume with a regular grid is obtained by re-shaping the regular 1D array to the original 3D grid size [Figure 4.6 (c)]. Note that if more than one intensity value falls into a single element of the regular grid, their averaged intensity is used instead as shown in Figure 4.6 (b).

4.3.3 Pole Figure Measurements

Structural anisotropy, for example film texture, dictates the physical properties of thin films including their magnetic, electrical and mechanical properties. Texture orientations which technically refer to the preferred orientation of a films' crystallites are observed using pole figures (Culity 1978). In this work, pole figure measurements were performed by mounting the sample on a six or four-circle diffractometer allowing for the necessary angular movements (Figure 4.6) of both the sample (azimuth (φ_s, elevation ψ_s and incidence ω) and the Pilatus 100k area detector (scattering angle $2\theta_{Bragg}$). The detector angle defines a family of crystalline planes {hkl} with interplanar spacing d_{hkl} via Bragg's law:

$$2d_{hkl}sin\theta_{Bragg} = n\lambda$$

where θ_{Bragg} is the Bragg angle, λ is the x-ray wavelength and n is an integer. The sample surface normal is set to coincide with the azimuthal rotation axis. The incident angle ω is set equal to θ_{Bragg} such as to have the normal to the sample surface coinciding with the scattering vector $k = k_f - k_i$. Here k_i and k_f are the incident and scattered wave vectors, with their directions fixed by the x-ray incident beam and the direction of the detector position respectively. Thus, for $\boldsymbol{\psi = 0}$°, the (hkl) planes probed are the ones oriented parallel to the surface of the sample as shown in Figure 4.7(a). The corresponding probed planes become perpendicular to the surface of the sample for $\psi = 90°$ as shown in Figure 4.7(b). The pole figure measurements are taken at temporal resolutions of 0.5 seconds, spanning a chi range of $0° - 90°$ and a phi range of $0° - 180°$. The detector is fixed at a diffraction angle ($2\theta_{Bragg}$) and the diffracted intensity is collected by varying angle psi ($\boldsymbol{\psi}$) (tilt angle from sample surface normal direction) and the phi (φ) angle which represents the rotation angle around the sample surface normal direction. The pole figure is plotted in polar coordinates $\boldsymbol{\psi}$ and φ with the center of the pole figure defined as $\boldsymbol{\psi}$ =0° (direction normal to the substrate) and the outer end $\boldsymbol{\psi}$ =90°(direction parallel to sample surface)

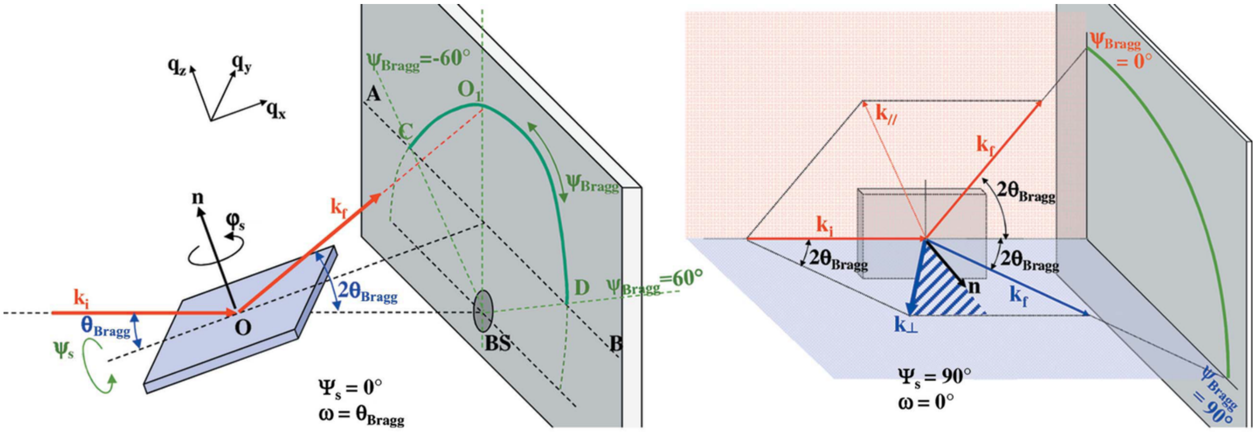

(*a*) (*b*)

Figure 4.7: Schematics of the sample geometry and angular movements for the pole figure measurements. The detector angle 2θ, and sample rotation angles (the incident angle ω= θ_{Bragg}, the sample azimuth and the sample elevation s) are shown; BS denotes the X-ray beamstop (for the direct/transmitted beam) and AB the sample horizon. The cases s = 0 and s = 90 are, respectively, shown in (a) and (b). Figure reprinted from [16]

4.3.4 Transmission Electron Microscopy Measurements

Ernst Ruska invented the electron microscope in 1933 [1] and received the Nobel prize in physics in 1986 for his work in electron optics. Transmission Electron Microscopy (TEM) measurements employ a focused beam of high energy electrons to examine the crystal structure, orientation and chemical composition of material specimen through electron diffraction pattern analysis. TEM has profound application in structural investigation of materials because it allows for studies to take place at the micron and nanometer scale with high resolution and high magnification imaging ~10^6 x. Images are produced by illuminating the samples with an electron beam ~200kV in a high vacuum environment and focusing the electrons transmitted through the specimen on a fluorescent screen for observation. The TEM data in this work was collected using the JEOL 3100R05 and JEOL 2100F machine setups at the Michigan Center for Materials Characterization and films were prepared by mechanical polishing followed by argon ion milling.

4.3.5 Rapid Thermal Annealing

Rapid Thermal Annealing is a processing step used widely in the semiconductor industry. Wafers are heated to either activate dopants, facilitate interfacial reaction of the metal contacts, change the states of grown films, drive dopants into different films or to repair damage from ion implantation. The working principle of this technique involves heating a wafer rapidly to temperatures as high as 800°C – 900°C, holding it there for a certain amount of time and quenching it as quickly as possible. The wafer is heated either by using an indirect IR lamp, a hot plate or a hot chuck which is brought near the substrate and the temperature is measured using a thermocouple or a pyrometer. Unlike conventional furnace anneals, the annealing times are short, with each anneal lasting from a few seconds to a few minutes. The small quench times help to effectively control the diffusion of dopants inside the wafers but can lead to issues like wafer stress and loss of process uniformity. The $ZnSnN_2$ films in this work were subjected to Rapid Thermal Annealing treatment at 700°C for 30 seconds and their structural properties were studied using x-ray diffraction techniques.

Bibliography

[1] C. M. Schleputz, R. Herger, P. R. Willmott, B. D. Patterson, O. Bunk, Ch. Bronnimann, B. Henrich, G. Hulsen, and E. F. Eikenberry: Improved data acquisition in grazing-incidence X-ray scattering experiments using a pixel detector." Acta Crystallogr. A 61, 418{425 (2005), doi: 10.1107/S0108767305014790.

[2] Ch. Bronnimann, E. F. Eikenberry, B. Henrich, R. Horisberger, G. Huelsen, E. Pohl, B. Schmitt, C. Schulze-Briese, M. Suzuki, T. Tomizaki, H. Toyokawa, and A. Wagner: \The PILATUS 1M detector." Journal of Synchrotron Radiation 13 (2), 120{130 (2006), doi:10.1107/S0909049505038665.

[3] A. Bergamaschi, Ch. Br□onnimann, E. F. Eikenberry, B. Henrich, M. Kobas, P. Kraft, and B. Schmitt: \Experience and Results from the 6 Megapixel PILATUS System." PoS 057 , 049 (2007).

[4] P. Kraft, A. Bergamaschi, Ch. Br□onnimann, R. Dinapoli, E. F. Eikenberry, H. Graafsma, B. Henrich, I. Johnson, M. Kobas, A. Mozzanica, C. M. Schlep□utz, and B. Schmitt: Characterization and Calibration of PILATUS Detectors." IEEE Trans Nucl Sci (2009). Accepted.

[5] P. Kraft, A. Bergamaschi, Ch. Bronnimann, R. Dinapoli, E. F. Eikenberry, B. Henrich, I. Johnson, M. Kobas, C. M. Schleputz, P. R. Willmott, and B. Schmitt: \Performance of single photon counting pixel detector modules." J. Synch. Rad. 16 (3), 368{375 (2009), doi: 10.1107/S0909049509009911.

[6] H. You, “Angle calculations for a ‘4S+2D’ six-circle diffractometer,” J. Appl. Crystallogr. 32, 614 (1999).

[7] W. R. Busing and H. A. Levy, “Angle calculations for 3- and 4-circle X-ray and neutron diffractometers,” Acta Crystallogr. 22, 457 (1967).

[8] Certified Scientific Software, “SPEC,” http://www.certif.com/.

[9] You, H. Angle calculations for a `4S+2D' six-circle diffractometer. Journal of Applied Crystallography 32, 614-623, (1999).

[10] Banchoff, T. & Wermer, J. Linear algebra through geometry. (Springer Science & Business Media, 2012).

[11] Bloom, D. M. Linear algebra and geometry. (CUP Archive, 1979).

[12] Kostrikin, A. I., Manin, Y. I. & Alferieff, M. E. Linear algebra and geometry. (Gordon and Breach Science Publishers, 1997).

[13] Shafarevich, I. R. & Remizov, A. Linear algebra and geometry. (Springer Science & Business Media, 2012).

[14] C. M. Schlepütz, S. O. Mariager, S. A. Pauli, R. Feidenhans’l, and P. R. Willmott, “Angle calculations for a (2+3)-type diffractometer: focus on area detectors,” J. Appl. Crystallogr. 44, 73 (2011).

[15] Yongsoo Yang, PhD Thesis, Synchrotron X-ray Diffraction Studies on Oxide Surfaces and Interfaces, 2014

[16] C. Mocuta, Marie-Ingrid Richard, J. Fouet, S. Stanescu, A. Barbier, C Guichet, O. Thomas, S. Hustache, A. V. Zozulyaa and D. Thiaudie`rea, Fast pole figure acquisition using area detectors at the DiffAbs beamline – Synchrotron SOLEIL, J. Appl. Cryst. (2013). 46, 1842–1853, ISSN 0021-8898, doi:10.1107/S0021889813027453

CHAPTER V

$ZnSnN_2$ Structural Studies

5.1 Introduction

$ZnSnN_2$ has been explored widely in a theoretical context, with calculations performed by density functional theory (DFT) to predict its stable crystal structure and optoelectronic properties including the bandgap. The motivation for this work hinges on three major questions of interest. 1) Can we structurally characterize and validate the theoretically predicted ordered orthorhombic and disordered wurtzite phases in single crystal $ZnSnN_2$ films? 2) What is the influence of MBE growth conditions on the crystal structure of $ZnSnN_2$ films as it relates to order and disorder on the cation sublattice? 3) Is there a structural phase transition from the wurtzite to the orthorhombic phase? What is the nature of this phase transition and at what temperature does it occur? We sought to determine the influence of growth conditions such as substrate temperature and nitrogen flow rate on the crystal structure of $ZnSnN_2$ and hence disorder on the cation sublattice via x-ray diffraction techniques. Through annealing treatment via rapid thermal annealing, we investigated the structural phase transition from the disordered wurtzite phase to the ordered orthorhombic phase. The experimental results and discussion about the $ZnSnN_2$ films grown on lithium gallate (LGO) and Yttria stabilized zirconia (YSZ) substrates have been published in a peer-reviewed journal [1]. A significant part of this chapter consists of the text and figures from that article.

5.2 $ZnSnN_2$ Films Grown on Lithium Gallate ($LiGaO_2$) Substrates

5.2.1 Measurements

Synchrotron x-ray diffraction experiments were carried out at beam lines 13-BM-C, 33-ID-D, and 33-BM-C of the Advanced Photon Source. A monochromatic X-ray beam at 15 keV was used to probe the crystal structure of each film and its epitaxial relationship with the substrate. The beam spot size was optimized at 270 μm x 30 μm in the horizontal and vertical directions respectively. To resolve the symmetry of the $ZnSnN_2$ films, high-resolution three-dimensional reciprocal space maps (3D RSMs) were measured around high-order film Bragg peaks. Using a PILATUS 100K area detector, [2,3] the intensity distribution around each peak was measured in a series of single scans along the L-direction as a set of two-dimensional reciprocal space slices. These were then used to reconstruct the 3D RSMs. [4]

5.2.2 Results

We performed extensive x-ray diffraction (XRD) measurements on the epitaxial films using synchrotron radiation at the Advanced Photon Source. Unit-cell refinement measurements for the $ZnSnN_2$ films were performed by fitting a minimum of twenty (20) film reflections using film Bragg-peak positions obtained from Kappa diffractometer angle calculations. For $ZnSnN_2$ films grown on (001) $LiGaO_2$, measurements revealed lattice-constant values of a = 5. 9557(3) Å, b = 5. 5778(3) Å and c = 6.8852(3) Å, with off specular Bragg peak extinctions corresponding to the $Pn2_1a$ symmetry [space group (33)]. Figure 5.1 shows the relationship between the $Pn2_1a$ and $Pna2_1$ symmetries. The $Pn2_1a$ symmetry has a 2_1 screw axis parallel to the y direction with an n-glide plane perpendicular to the x axis and an a-glide plane perpendicular to the z axis. This symmetry also represents the sixth setting in space group (No. 33) with permutation ($a\bar{c}b$) relative to the $Pna2_1$ symmetry with permutation (*abc*). The $Pn2_1a$ space group is also characterized by a

90° rotation of the y and z axes about the in plane x axis relative to the Pna2_1 symmetry. To preserve the right-hand rule during the conversion from Pna2_1 to Pn2_1a, all the atomic positions along the z axis in the Pna2_1 symmetry are first inverted before making the 90° rotation of the b and c-axes about the a-axis.

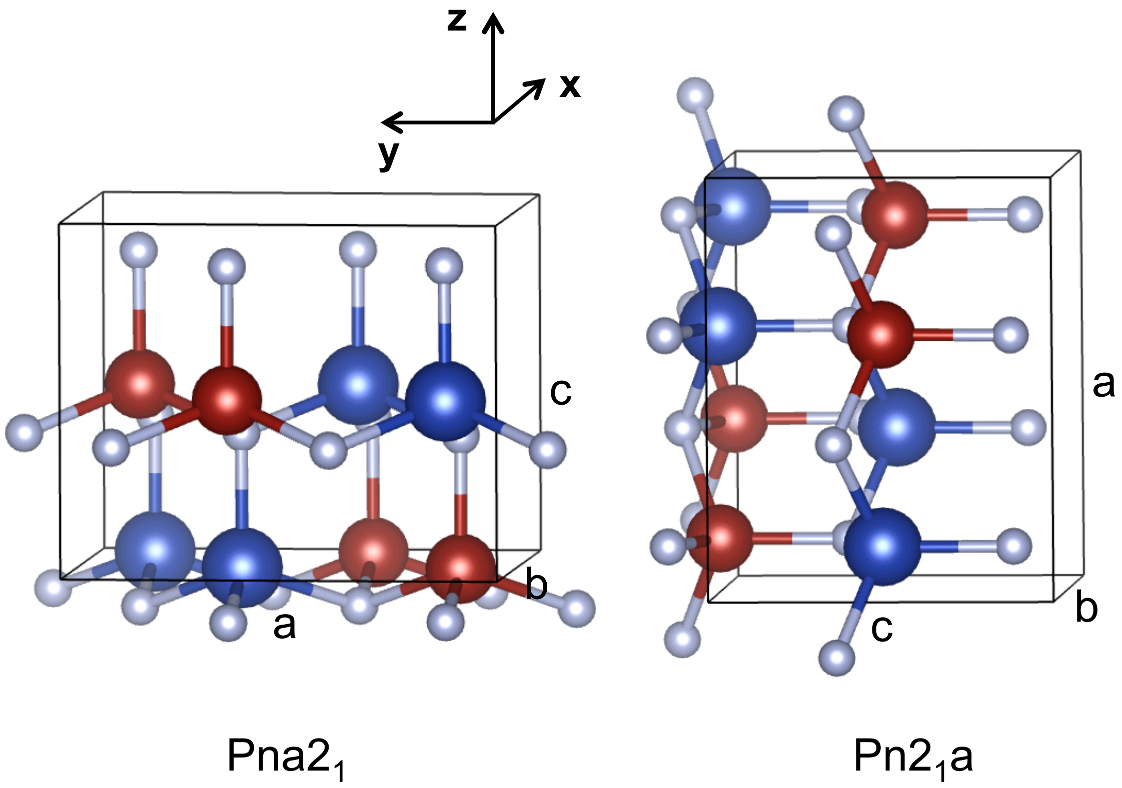

Figure 5.1: Space group 33 permutations Pna2_1 and Pn2_1a, where Zn, Sn, and N atoms are depicted in red, blue, and gray, respectively. The z-axis points along the out-of-plane growth direction. We found that $ZnSnN_2$ grows in the Pna2_1 structure on YSZ (111) substrates and in the Pn2_1a structure on LGO (001) substrates. Pn2_1a differs from Pna2_1 by a 90˚ rotation around the x-axis. Lattice constants are labeled in order of decreasing length, and the b lattice constant is along the x-axis. The values of the lattice constants are included in Table 5.1.

We note that the unit cell lattice parameters of orthorhombic films, P56 and P57 are, on average, within 2% and 1%, respectively, of the results on polycrystalline $ZnSnN_2$ films. [5] It is also clear from Table 5.1 that the unit-cell volume of P56 shows a difference of less than 3% with respect to the DFT predictions, while P57 has a less than 1% difference with DFT. We attribute the variation in unit cell parameters between these two orthorhombic films to the differences in growth conditions. The films were deposited at Sn effusion-cell temperatures of 1040 °C and 1050 °C for

P56 and P57, respectively. The unit-cell lattice parameters obtained from XRD measurements and DFT calculations are compared in Table 5.1. Our first-principles calculation studies based on DFT were used to determine the optimized structure of the 16-atom orthorhombic $ZnSnN_2$ unit cell, with projector-augmented waves [6] and a cutoff of 350 eV as implemented in the Vienna Ab initio Simulation Package (VASP). [7] The calculations use the Perdew-Burke-Exchange (PBE) [8] functional for the exchange correlation potential. DFT-computed lattice parameters were found to be a = 5.914 Å, b =6.812 Å, and c = 5.542 Å, referenced to the $Pna2_1$ symmetry group [space group (33)]. Comparing the experimentally determined lattice constants for single-crystal $ZnSnN_2$ films grown on LGO, referenced to the $Pbn2_1$ symmetry with results from DFT calculations (Table 5.1) we note that there are 1.1%, 0.7% and 0.65% differences between the experimental and the calculated lattice constants a, b and c, respectively. These differences can be attributed to the significant compressive epitaxial strain in the $ZnSnN_2$ films induced by the substrate (the DFT model assumes a fully relaxed bulk $ZnSnN_2$ structure), as well as the typical 1% accuracy of DFT in predicting lattice constants. The film lattice constants obtained are also in good agreement with LDA calculations [9] showing differences with our experimental results of 1.9% and 1.8% in a and b lattice constants, respectively, while the out-of-plane lattice constant, c, of P56 is in good agreement (~ 0.04% difference).

Table 5.1: Experimentally determined lattice parameters for our orthorhombic single-crystal $ZnSnN_2$ (ZSN) films referenced in the $Pbn2_1$ symmetry compared with experimentally determined lattice constants for polycrystalline $ZnSnN_2$ films and results from different computational methods. Ideal axial ratios are b/aw = 1.732 and c/aw =√(8/3) = 1.633, aw = a/2

	Orthorhombic (Experiment)			Orthorhombic (Calculated)	
	P56[a] (ZSN/LGO)	P57[a] (ZSN/LGO)	[b]Polycrystalline-ZSN	PBE, this work	[c]LDA
a (Å)	6.8852(3)	6.8115(3)	6.753	6.812	6.76
b (Å)	5.9557(3)	5.9544(3)	5.842	5.914	5.85
c (Å)	5.5778(3)	5.4583(3)	5.462	5.542	5.58
a_w (Å)	3.4426	3.4059	3.3765	3.406	3.38
b/a_w	1.730	1.748	1.73	1.736	1.731
c / a_w	1.620	1.603	1.618	1.627	1.651
Volume ($Å^3$)	228.724	221.380	215.48	223.3	220.667

[a] Lattice constants given are referenced to the $Pbn2_1$ structure with lattice constants in order of decreasing length

[b] from Ref [5].

[c] from Ref [9].

Punya et al. [9] suggested that the orthorhombic unit cell of II-IV-N_2 compounds can be viewed as a 2 x √3 superstructure of the wurtzite structure along orthohexagonal axes. The orthorhombic unit cell in this instance is defined by choosing $a_{ortho} = 2a_W$ and $b_{ortho} \approx \sqrt{3}a_W$ with axial ratio b/ a_W referenced to the orthorhombic structure equal to 1.732 and $c/a_W = 1.633$. The wurtzite structure is assumed to have an underlying hexagonal Bravais lattice from which the orthorhombic superstructure is derived. The comparison to the ideal axial ratios in the hexagonal close packed (hcp) structure is made to illustrate the analogy between the cation-sublattice ordering in the orthorhombic structure and the ABAB stacking in the hcp structure. Our measurements show a less than 1% difference between the ideal axial ratios and experimental values in the orthorhombic films. The b/a_W ratio is slightly overestimated in the experimental results for P57 and the calculated DFT results, while the c/a_W ratio is underestimated in the experimental results by less than 2%.

To understand the epitaxial relationship between the $ZnSnN_2$ films and $LiGaO_2$ substrates, and hence the role of strain on the structure of the films, 3D reciprocal space maps (RSMS) were reconstructed around high-order-specular and off -specular film Bragg peaks. Figure 5.2 shows a high-resolution, XRD reciprocal space map around the (004) reflection of the orthorhombic phase. The (004) RSM shows clear evidence of single domain $ZnSnN_2$ epitaxy, indicated by the absence of any splitting in both film and substrate reflections.

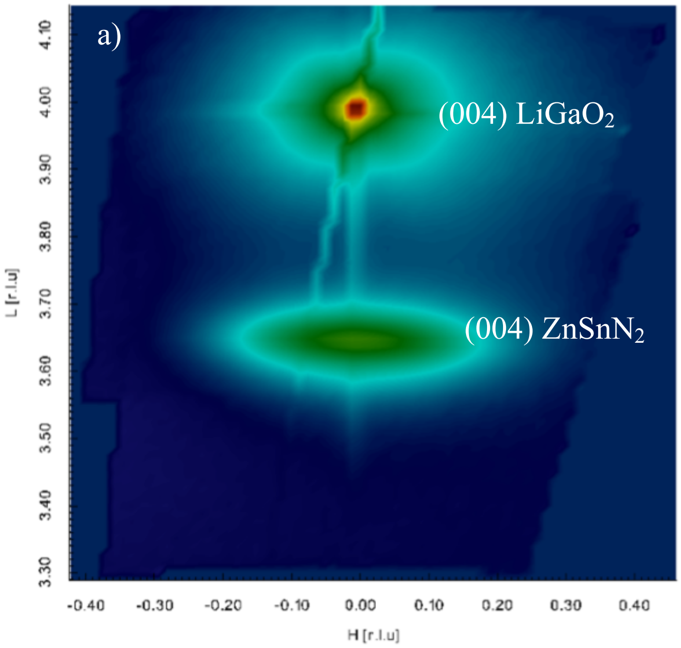

Figure 5.2: RSM taken around the (004) Bragg peak of $ZnSnN_2$. H and L are given in reciprocal lattice units of the LGO substrate.

The reciprocal space maps of the (102) and $(\bar{1}02)$ film Bragg peaks in Figures 5.3(a) and 5.3(b) respectively show partial substrate-induced strain in the film with the bulk of the film relaxed. The center of the film Bragg peak occurs at $H = \pm 0.93$ in substrate reciprocal lattice units, indicating ~ 97% in-plane relaxation. This relaxation is consistent with film lattice constants approaching the bulk values that have been predicted through our DFT calculations and published theoretical lattice constants, as shown in Table 5.1. The maximum compressive strain along the

[100] direction needed for the film to be in registry with the substrate (lattice mismatch) is ~ 7.4% based on calculations from fitted $ZnSnN_2$ and $LiGaO_2$ lattice parameters.

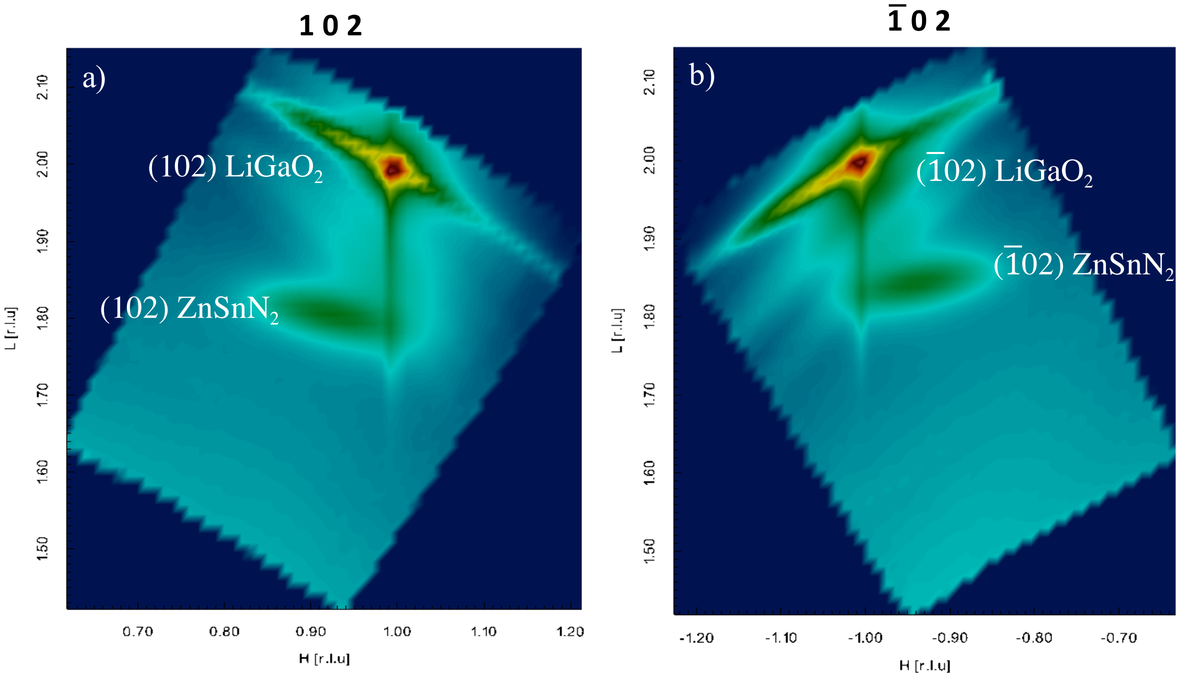

Figure 5.3: RSMs taken around the $ZnSnN_2$ (102) and ($\bar{1}$02) film symmetry equivalent Bragg peaks. H and L are given in reciprocal lattice units of LGO substrate.

We attribute the film relaxation to having relatively thick films (~ 125nm), which may reduce the substrate-induced strain effect on the film. We also note here that the (102) and ($\bar{1}$02) $ZnSnN_2$ symmetry-equivalent Bragg peaks in Figure 5.3(a) and 5.3(b) appear at slightly different positions along the L direction due to the significant substrate miscut of, ~ 1.2°. Pole figure measurements were carried out to verify the two-fold symmetry of the orthorhombic films and the results are shown in Figure 5.3 below where clear two-fold symmetry is shown for the (302) peak. The two-fold symmetry of orthorhombic films is evident from the pole figure as seen in Figure 5.4 with the (302) $ZnSnN_2$ film Bragg peak showing up at the same χ value of ~60° as the ($\bar{3}$02) $ZnSnN_2$ peak and out of phase by ~180°.

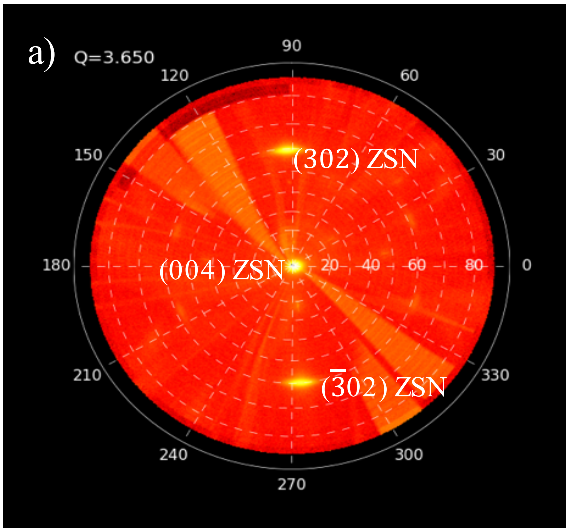

Figure 5.4: Pole figure showing two-fold symmetry of (302) peak in $ZnSnN_2$ film

The $ZnSnN_2$ (004) Bragg peak is shown in projection parallel to the surface normal direction at $\chi = 0°$, as expected for a [001]-oriented orthorhombic film epitaxial with a [001]-oriented substrate. [001] is the direction coming out of the page while [010] is parallel to $\phi = 0°$ and [100] is parallel to $\phi = 90°$. The darker regions in the pole plots represent regions where filters were inserted to protect the detector from strong substrate Bragg peak radiation. Pole figure measurements were carried out with the Pilatus 100K area detector fixed at a diffraction angle (2θ) and the diffracted intensity was collected by varying angle chi (χ) (tilt angle from sample surface normal direction) and the phi (ϕ) angle which represents the rotation angle around the sample surface normal direction. The pole figure for any given (*hkl*) plane is viewed by projecting a reconstructed image from the hemisphere onto a flat surface (stereographic projection) showing the crystallographic distribution of the orientation of the normal to this plane. Pole figures are plotted in polar coordinates χ and ϕ with the center of the pole figure defined as $\chi=0°$ (direction normal to the substrate) and the outer end $\chi=90°$(direction parallel to sample surface).

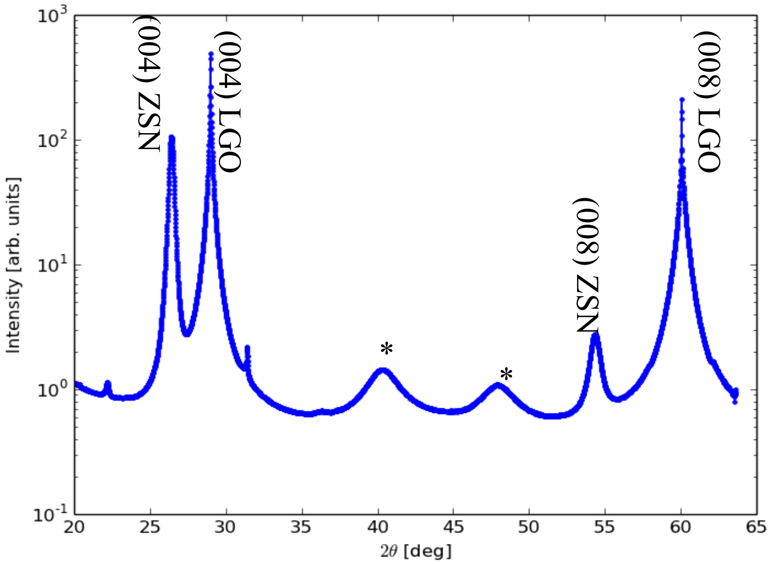

Figure 5.5: (00L) rodscan measurement of the orthorhombic film of $ZnSnN_2$

Figure 5.5 displays a typical θ–2θ x-ray diffraction (XRD) scan of a $ZnSnN_2$ film on a $LiGaO_2$ substrate. Intense 00L reflections of the orthorhombic phase were observed at the (004) and (008) $ZnSnN_2$ peak positions, suggesting that this $Pn2_1a$ orthorhombic phase can be stabilized when $ZnSnN_2$ films are grown on $LiGaO_2$. The (002) and (006) Bragg peaks though allowed in this symmetry have negligible structure factor and are not clearly visible in this rodscan measurement. The rodscan measurement result also demonstrates that the film is phase-pure without any detectable Zn or Sn impurity. The chalcopyrite (004) peak of $ZnSnN_2$ is expected to be more intense than the (008) peak due to the larger contrast in atomic factors between each sublattice that is a result of ordering on the cation sublattice. Additional peaks in this scan showing up at $2\theta \approx 40°$ and $2\theta \approx 47°$ are powder rings originating from silver paste used during the sample mounting process in the experimental setup. From Figure 5.3, we can deduce that $ZnSnN_2$ films deposited on LGO are under compressive strain. Judging from its diffraction pattern, and from asymmetric reflections, the strain is accommodated by deformation of the unit cell.

5.2.3 Discussion

To the best of our knowledge, we have grown the first reported case of single crystal $ZnSnN_2$ films grown on $LiGaO_2$ substrates. X-ray diffraction experiments and resulting analysis shows definitive evidence of $ZnSnN_2$ films exhibiting the ordered orthorhombic structure with $Pn2_1a$ symmetry, a consequence of being grown on a substrate with like symmetry. The $ZnSnN_2$ films grew in the $Pn2_1a$ orientation to match the symmetry of the underlying $LiGaO_2$, which had the effect of minimizing the in-plane lattice constant mismatch with this orientation of LGO. Experimental values are found to be in good agreement with results from polycrystalline films and theoretical calculations. Our work demonstrates that the orthorhombic phase of $ZnSnN_2$ can be stabilized by growing $ZnSnN_2$ films on an orthorhombic substrate such as $LiGaO_2$.

5.3 $ZnSnN_2$ Films Grown on Yttria Stabilized Zirconia Substrates

5.3.1 Monoclinic Distortion in Wurtzite Films

Table 5.2 shows the lattice constants for films initially grown at low values of substrate temperature ~ 400°C by Nathaniel Feldberg at the University at Buffalo, The State University of New York. Unit cell refinement for these films was performed with at least seventeen specular and off specular reflections. These films clearly have a hexagonal lattice with c/a ratios within less than 1% of the ideal value of 1.633 and the unit cell volumes within 1% of each other.

Table 5.2: Experimentally determined lattice constants in Å and unit cell volume in $Å^3$ for disordered $ZnSnN_2$ films. Note that the ideal wurtzite ratio $c/a_w = \sim 1.633$

Film	**a(Å)**	**b(Å)**	**c(Å)**	**c/a**	**β (°)**	**α(°)**	**γ (°)**	**Volume ($Å^3$)**
p36	3.3792(17)	3.3795(19)	5.5155(14)	1.632	89.986(25)	90.017(27)	120.007(36)	54.545(48)
p50	3.3846(16)	3.3852(16)	5.5645(30)	1.644	89.928(53)	90.042(53)	119.982(26)	55.224(50)
p58	3.3900(23)	3.3895(25)	5.4800(18)	1.617	90.011(39)	90.010(41)	119.990(45)	54.537(63)
p59	3.3902(24)	3.3906(25)	5.4720(16)	1.614	89.986(23)	90.008(20)	120.011(18)	54.471(25)
p60	3.3840(22)	3.3850(24)	5.4804(19)	1.620	89.984(41)	89.998(42)	120.004(47)	54.364(61)
p64	3.3867(19)	3.3867(20)	5.4762(18)	1.617	90.022(38)	89.992(37)	120.001(36)	54.395(52)

Reciprocal space maps reconstructed around high order film Bragg peaks revealed very diffuse and broad Bragg peaks indicative of defect prone films with the possibility of monoclinic distortion. This is shown in Figure 5.6 with reciprocal space maps taken at the (114) $ZnSnN_2$ hexagonal Bragg peak position for films P36, P60 and P58. Q_x-Q_z, Q_y-Q_z and Q_x-Q_y reciprocal space map cuts were made from a 3-dimensional volume and the 2D projections are analyzed below.

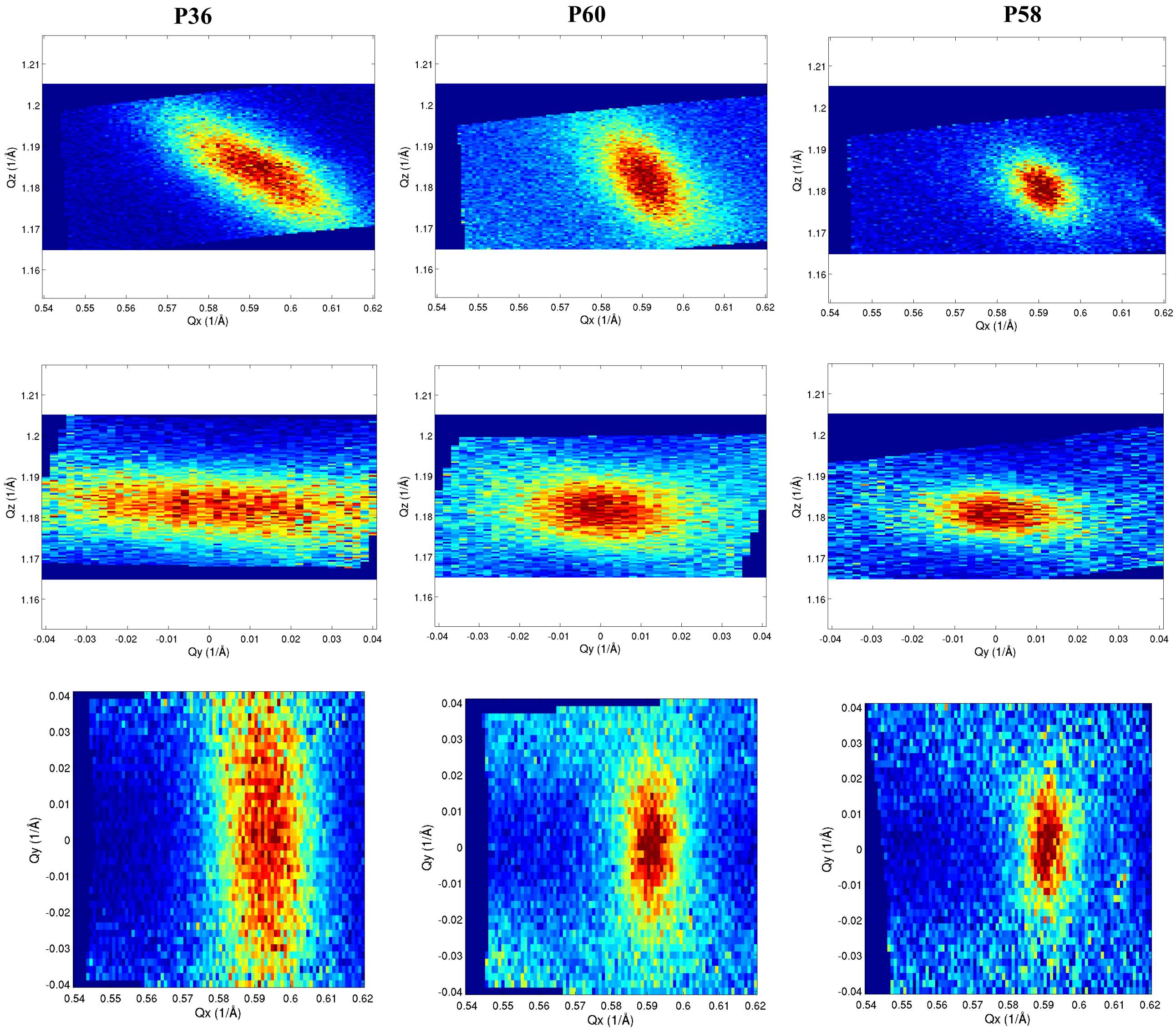

Figure 5.6: 3DRSMs taken around the (114) peak of $ZnSnN_2$

Film p58 shows the narrowest peak width in Q_x, Q_y and Q_z compared to films p36 and p60. We find that for all samples, Bragg peaks are much broader in the Q_y direction compared to Q_x. This proportionate broadening means that the peaks are broadened in such a way as to maintain the magnitude of the Q vector and indicates that the broadening is mainly due to discrepancies in unit cell angles and not lattice vector lengths which induces monoclinic distortion in the films. For all the samples, the peaks are broader in Q_y compared to Q_z meaning that the distortion i.e. defects and tilted domains are mostly limited to the in-plane direction. Since our $ZnSnN_2$ films are grown on the (111) surface of YSZ, they assume a hexagonal symmetry. Below we illustrate the six possible versions of monoclinic distortion in the $ZnSnN_2$ films due to growth on (111) YSZ.

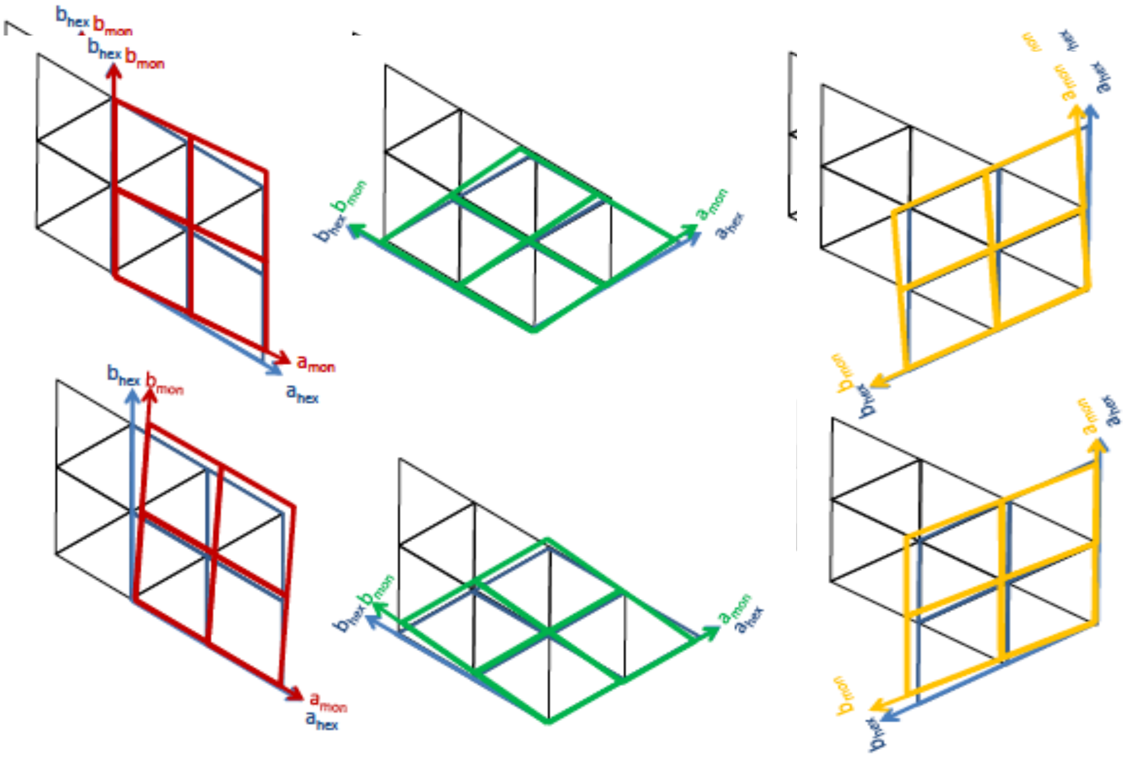

Figure 5.7: Six equivalent monoclinic domains possible in $ZnSnN_2$ films grown on a hexagonal substrate like YSZ. Figure courtesy of Dr. Yongsoo Yang

In this case, six equivalent domains with monoclinic distortion are possible when the film is grown on a hexagonal substrate (Figure 5.7). Unfortunately for x-ray measurements, the Bragg peaks from the six different domains overlap and appear at the same Bragg peak position, hence we obtain a broad (smeared out) peak at the hexagonal peak position giving us a hexagonal unit cell in the unit cell refinement calculations. An example of the six-fold diffraction pattern resulting from the orientation of the various monoclinic domains is shown in Figure 5.8

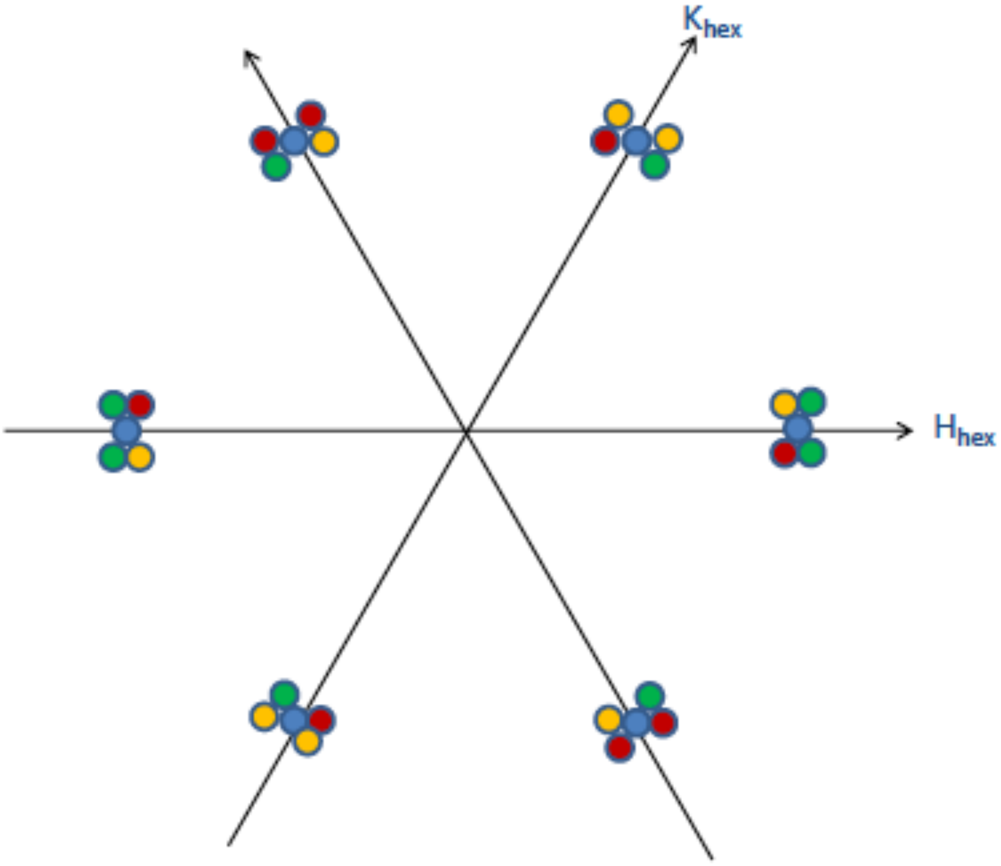

Figure 5.8: Six-fold diffraction symmetry resulting from monoclinic distortion. Figure courtesy of Dr. Yongsoo Yang

5.3.2 Characterization of Wurtzite Phase of $ZnSnN_2$ films

The disordered phase of $ZnSnN_2$, associated with random distribution of Zn and Sn atoms on the cation sublattice, has been studied in multiple reports. Feldberg et al. [10] reported a unit cell of a = 3.383 Å, b = 3.379 Å and c = 5.567 Å in monoclinic films (they ascribed small angular distortions to monoclinic symmetry). Subsequent growth at substrate temperatures between 420°C and 550°C resulted in the formation of single crystal wurtzite $ZnSnN_2$ films. It is important to note that these films were grown at an excess of 20:1 Zn: Sn flux based on QCM calculations. [13] The resulting RHEED pattern exhibits 60° rotational periodicity characteristic of wurtzite films. An orthorhombic film would have exhibited a 180° rotational periodicity with 90° spacing between the RHEED streaks. X-ray diffraction measurements on $ZnSnN_2$ films grown on (111) YSZ substrate revealed a wurtzite unit cell with lattice constants in good agreement with experimental results reported in Feldberg et al. [10] Table 5.3 shows the experimentally determined lattice constants for disordered films obtained by fitting at least twenty off specular reflections.

Table 5.3: Experimentally determined lattice constants in Å and unit cell volume in $Å^3$ for disordered $ZnSnN_2$ films. Note that the ideal wurtzite ratio $c/a_w = \sim 1.633$

Film	a(Å)	b(Å)	c(Å)	c/a	α(°)	β (°)	γ (°)	Volume ($Å^3$)
p72	3.390(1)	3.389(1)	5.476(2)	1.615	90.01(3)	89.99(3)	120.00(2)	54.3920(5)
p75	3.3880(3)	3.3874(3)	5.4865(3)	1.619	89.9941(4)	89.986(4)	119.9983(4)	54.5285(5)
85c	3.3995(3)	3.3882(2)	5.5776(3)	1.641	89.124(3)	90.283(3)	120.5448(3)	55.637(3)
88d	3.3827(2)	3.3700(3)	5.4949(3)	1.624	90.3457(3)	89.9783(3)	119.6007(3)	54.248(3)

The film lattice parameters given in Table 5.3 are all consistent with the wurtzite structure to within margin of error. The unit cell volumes of films are also very similar with discrepancies of less than 2%. Since the wurtzite crystal is a result of a disordered cation sublattice, this would suggest that all these films have a degree of disorder in the cation sublattice. The pole figure shown in Figure

5.9 shows a six-fold diffraction pattern taken at Q = 2.424 for a disordered wurtzite film, consistent with hexagonal symmetry. It shows the plane symmetry with a preferential 60° orientation with respect to each other.

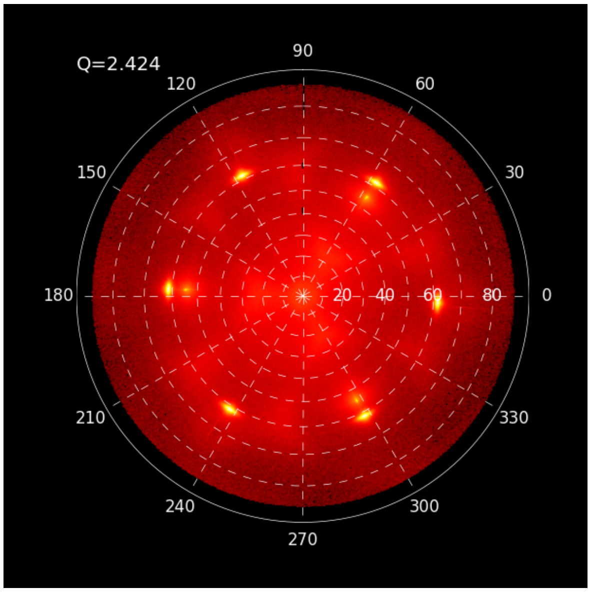

Figure 5.9: Pole figure of a wurtzite $ZnSnN_2$ film grown on (111) YSZ substrate showing a six- fold diffraction pattern

The disordered films also show preferential growth in the c direction as seen from the specular rod scan measurement in Figure 5.10. This is a result of the film trying to maintain an epitaxial relationship with the substrate by depositing with it's a and b lattice parameters ~ 3.38 Å in plane since they are relatively matched to the substrate lattice constant ~ 3.638 Å in the (111) projection of YSZ. This means that the (001) plane of the film is parallel to the (111) plane of the substrate. In the disordered wurtzite phase like the sphalerite phase of the related material $ZnSnP_2$, we expect the (002) peak to be more intense than the (004) peak and (006) peak due to the large atomic factor contrast caused by the presence of Zn and Sn atoms in each sublattice. We also note the large lattice mismatch between $ZnSnN_2$ and YSZ of approximately 7% resulting in tensile strain at the film-substrate interface since the epilayer has a larger in-plane lattice parameter than the substrate.

Strain values this high are expected to induce a significant number of defects in the film and could have a negative effect on the optoelectronic properties of $ZnSnN_2$.

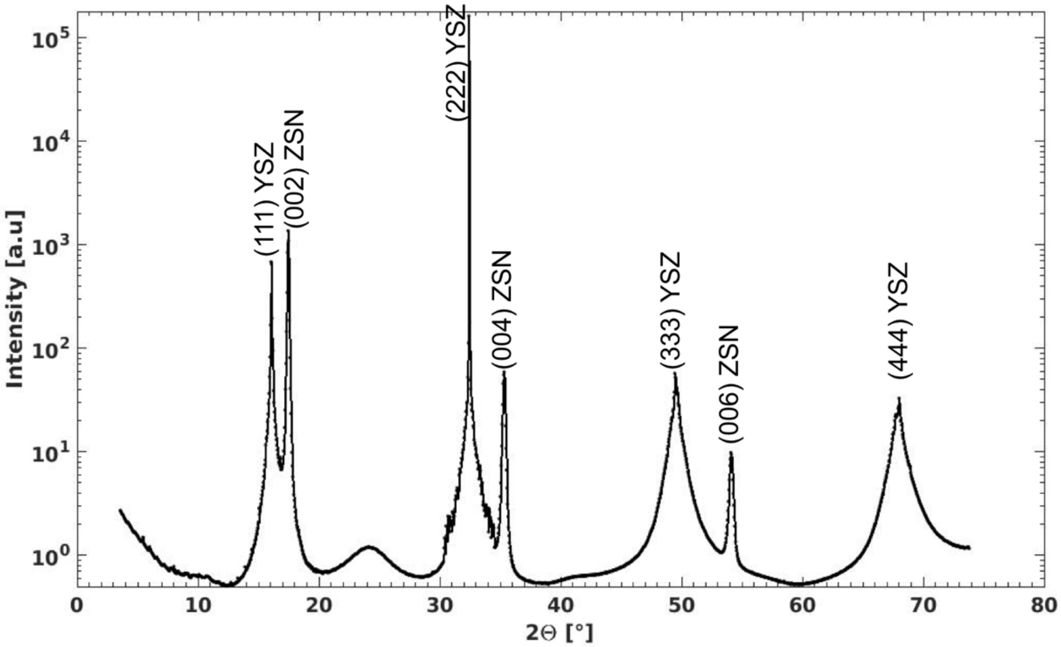

Figure 5.10: Specular rod scan measurement of disordered $ZnSnN_2$ film showing [001] oriented film

Reciprocal space maps taken around symmetry equivalent (102), $(0\overline{1}2)$ and $(1\overline{1}2)$ film Bragg peaks shown in Figure 5.11 show peaks representative of a single crystal film with no formation of domains. The symmetry equivalent peaks also appear at the same $Q_z \sim 2.18$ (1/Å) hence validating the symmetry equivalent hexagonal structure of these $ZnSnN_2$ films.

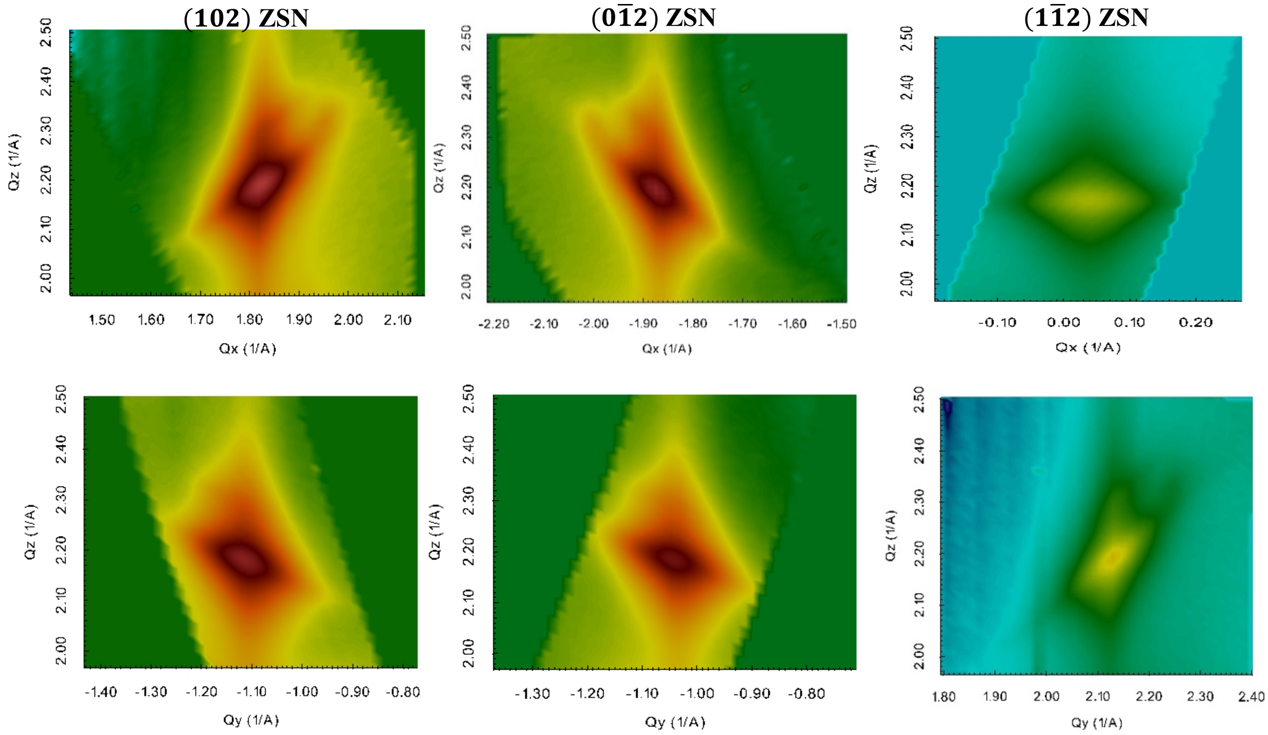

Figure 5.11: Reciprocal space maps taken around symmetry equivalent (102), (0$\bar{1}$2) and (1$\bar{1}$2) Bragg peaks in the hexagonal symmetry. Q_x, Q_y, Q_z are given in units of YSZ substrate.

5.3.3 Substrate Temperature Induced Wurtzite to Orthorhombic Phase Transition

Systematic variation of the growth conditions i.e. substrate temperature and nitrogen flux resulted in a structural phase transition from the wurtzite to orthorhombic structure as observed in Table 5.4.

Table 5.4: Experimentally fitted lattice constants for $ZnSnN_2$ films deposited on (111) YSZ substrate referenced in the wurtzite structure.

Film	a(Å)	b(Å)	c(Å)	c/a_w	V (Å^3)	Growth Temperature (°C)
P64	3.3882(3)	3.3832(3)	5.5274(3)	1.631	54.872	450
P71	3.366(2)	3.366(2)	5.842(3)	1.736	57.322	550

Film P64 was deposited under a substrate temperature of 450 °C and a nitrogen pressure of 10^{-5} Torr while film P71 was deposited under a substrate temperature of 550 °C and a nitrogen pressure of 10^{-5} Torr. There is a contraction in the basal plane of ~ 0.65% and a relatively large expansion in the out-of-plane direction of ~ 5.7% for film P71 grown at higher substrate temperatures and a lower value of nitrogen pressure. This phase transition as shown in Figure 5. 10(b) is associated with peak splitting along the [10L], [01L] and [11L] directions. The splitting is a direct result of the breaking of symmetry in the basal plane of the wurtzite unit cell and the occurrence of unequal in-plane axes characteristic of the orthorhombic structure with $a \neq b \neq c$. The six-fold diffraction pattern in Figure 5.12(a) shows the (102), (112) and (012) peaks of wurtzite $ZnSnN_2$; these three respective Bragg peaks are shown doubly split in Figure 5.12(b) with a corresponding twelve peak diffraction pattern observed.

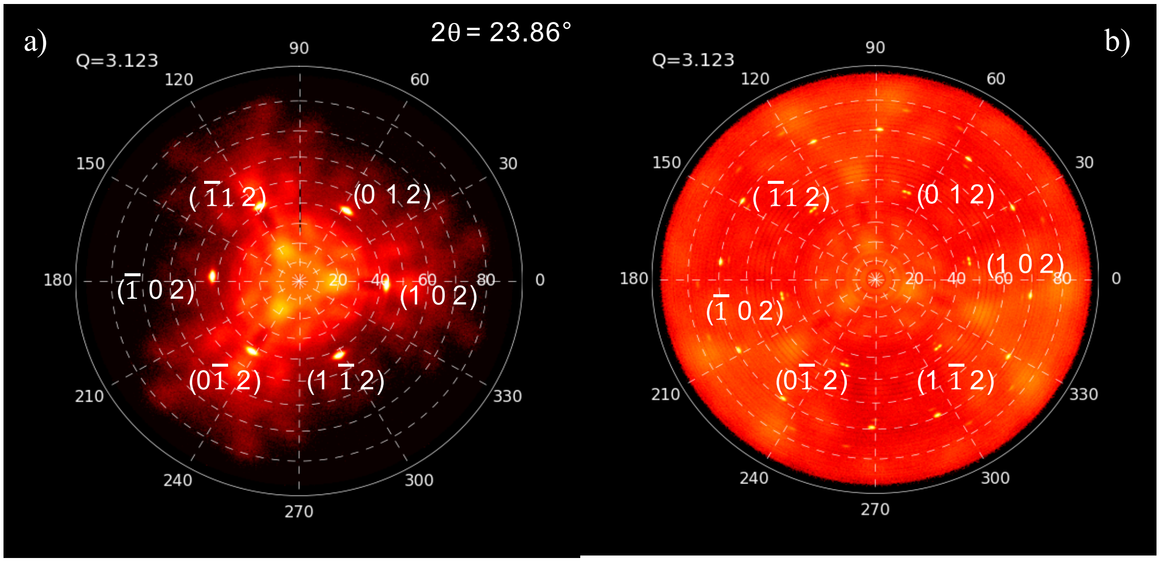

Figure 5.12: (102), (112) and (012) pole figure of $ZnSnN_2$ films grown on (111) YSZ substrate. (a) Wurtzite film (P64) grown at a substrate temperature of 450 °C. (b) Orthorhombic $ZnSnN_2$ film (P71) grown at a substrate temperature of 550 °C.

We also note that the in-plane lattice constant a ~6.732 for film P71 when referred to the orthorhombic lattice, is in good agreement with the in-plane lattice constant given in Ref. [11] for the orthorhombic $Pna2_1$ symmetry. Interestingly, the value of the c/a_w ratio of the orthorhombic P71 film when referenced in the hexagonal lattice frame is ~ 1.736, a value 6.3% larger than the "ideal" wurtzite axial ratio of 1.633 and in good agreement with the b/ a_w ratio given in our DFT calculations for the orthorhombic $Pna2_1$ symmetry. Similar studies in ordered chalcopyrite materials for example $ZnSnP_2$ have shown that the first order phase transition from a disordered sphalerite phase to an ordered chalcopyrite phase is accompanied by a tetragonal distortion associated with elongation of the c axis. No noticeable variation in the in-plane lattice constants was observed for our $ZnSnN_2$ films for the wurtzite and orthorhombic lattice constants defined in the hexagonal lattice. The $ZnSnN_2$ films in this study are under a tensile strain, so per Poisson's equation, we don't expect an elongation in the c-axis in the wurtzite to orthorhombic phase transition. This means that a phenomenon other than strain is responsible for inducing this phase transition. It is possible that a form of tetragonal distortion i.e. Jahn Teller distortion in $ZnSnN_2$ films associated with elongation of the axial Sn-N or Zn-N bond in the ordered cation sub lattice is responsible for the c axis elongation. This tetragonal distortion is associated with a reduction in symmetry from the hexagonal to the orthorhombic structure. This sample (P71), which is evidently of higher crystal quality than the films grown on LGO shows a clear distortion from the wurtzite phase and suggests that the large expansion in the c-axis spacing may be associated with the ordering of the heterovalent cations in the orthorhombic phase. These findings are consistent with studies on the related material $ZnSnP_2$ showing that higher growth temperatures are more likely to produce a more ordered film than lower growth temperatures. [12] This is a result of the dominance of kinetic processes in low-temperature MBE. [12]

These results show that by tuning growth conditions e.g. the substrate temperature, a structural phase transition from the wurtzite to orthorhombic phase can be achieved in $ZnSnN_2$ films grown on (111) Yttria stabilized zirconia substrates.

5.3.4 Temperature Induced Wurtzite to Orthorhombic Structural Phase Transition

Ordering in heterovalent ternary semiconductors is usually detected through XRD. For ternary semiconductors derived from both zincblende and wurtzite lattices, there is a lattice distortion associated with the cation lattice ordering. In chalcopyrite structures, which are derived from the zinc blende structure by a doubling of the cubic unit cell along the z axis, c/a can deviate from the zincblende value of 2 [11]. In wurtzite-derived orthorhombic structures with space group P $na2_1$, where $a_o = 2a_w$, $b_o = a_w \times \sqrt{3}$, $c_w=c_o$. The a parameter increases and the b parameter decreases, causing the a/b ratio to become greater than the ideal wurtzite value of $(2 \times\sqrt{3})/3$. These distortions, if large enough, can be detected using XRD through the splitting of Bragg peaks.

$ZnSnN_2$ films in this work were subjected to rapid thermal annealing (RTA) ex-situ at 700 °C for 30 seconds in 1000 sccm of nitrogen (N_2) (at atmospheric pressure) using the rcollinoGaAsN700 recipe. θ-2θ measurements shown in Figure 5.13(a) and (b) show the as grown and annealed $ZnSnN_2$ films respectively with obvious differences between the two crystal structures. The (111) super lattice reflection of the $Pna2_1$ symmetry found in the orthorhombic film is seen in the Figure 5.13(b) for the $ZnSnN_2$ film annealed in nitrogen at 700°C. Also, the (102) Bragg peak in the wurtzite film in Figure 5.13(a) does not appear in the orthorhombic phase but rather has split into the (130), (031) and (131) Bragg peaks. The (300) Bragg peak in the wurtzite phase is not allowed in the orthorhombic phase since only peaks with h=2n are allowed in the h00 plane. Subsequently we see the appearance of the (062), (206) and (624) reflections in the orthorhombic phase shown in Figure 5.13 (b). The superstructure Bragg peaks seen in Figure 5.13 (b) are consistent with allowed reflections for the $Pna2_1$ orthorhombic symmetry. This θ-2θ measurement shows a definitive structural phase transition from the wurtzite to orthorhombic phase in $ZnSnN_2$ films subjected to rapid thermal annealing at 700°C in nitrogen at atmospheric pressure.

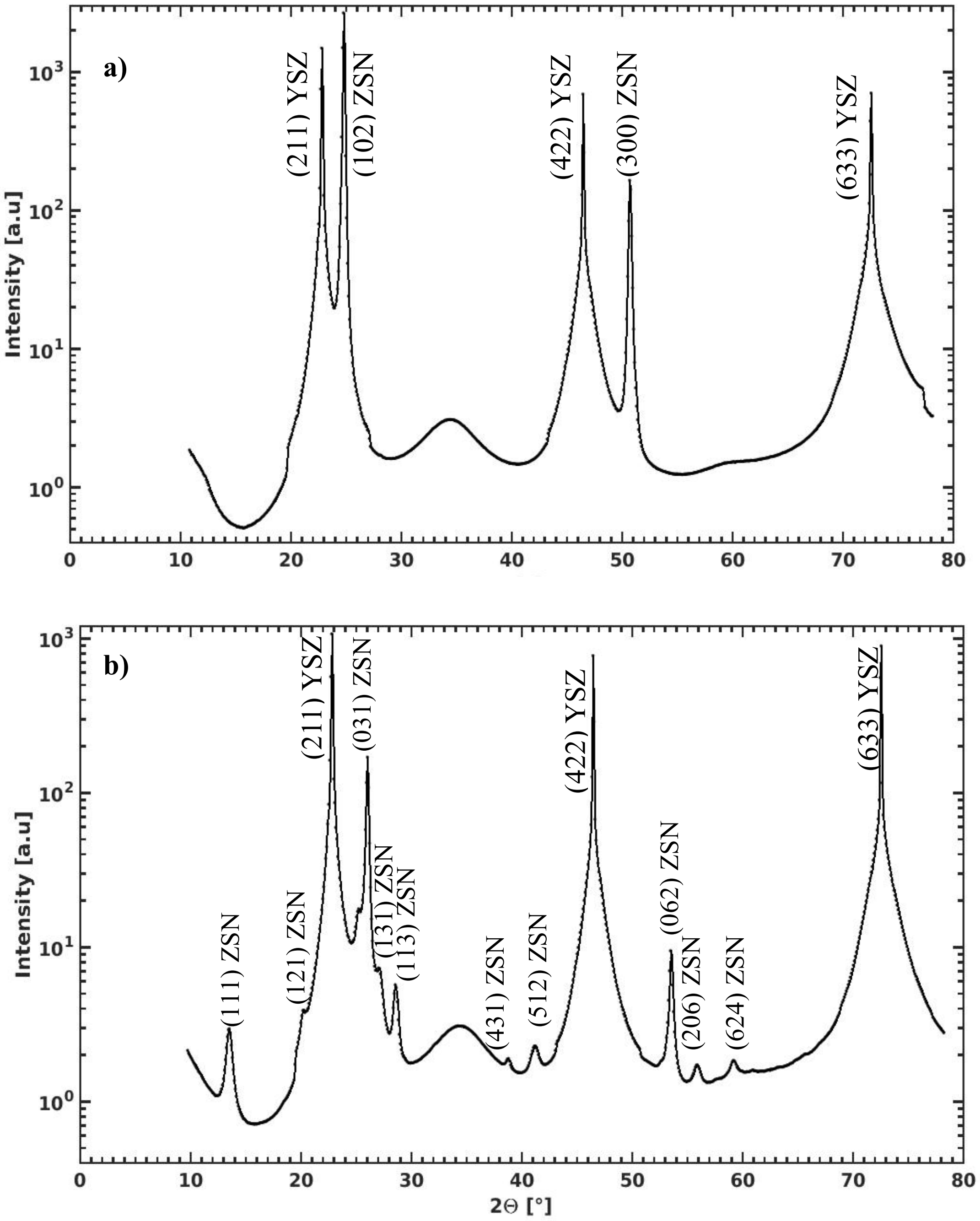

Figure 5.13: θ-2θ measurement for a) As-grown wurtzite $ZnSnN_2$ film and b) $ZnSnN_2$ film annealed in nitrogen at 700°C

After performing RTA on known wurtzite $ZnSnN_2$ films ex-situ, it was important to determine the actual temperature at which the structural phase transition from the wurtzite to orthorhombic phase takes place. $ZnSnN_2$ films were heated from 500°C to 800°C in 50°C increments and θ-2θ measurements were taken at each of those temperatures to investigate the structural phase transition temperature. Figure 5.14 (a) to 5.14 (c) shows the evolution of the $ZnSnN_2$ crystal structure from the wurtzite phase to the orthorhombic $Pna2_1$ phase. The $ZnSnN_2$ film in Figure 5.14 (a) was heated to 500°C, the θ-2θ measurement shows the (211), (422) and (633) Bragg peaks of YSZ together with the (102), (300) and (404) wurtzite Bragg peaks of $ZnSnN_2$. Further heating of the film to 550°C did not yield any change in the crystal structure as shown in Figure 5.14 (b) although there is a noticeable decrease in the magnitude of the intensity of the wurtzite film Bragg peaks from Figure 5.14(a) to Figure 5.14(b) and the YSZ structure remains the same. This is likely the result of the suppression of disorder in the cation sublattice and the subsequent onset of ordering. Upon further annealing of the film to 600°C, there is a complete disappearance of all the wurtzite film peaks and a discontinuous jump in lattice parameters accompanied by the emergence of orthorhombic peaks- (122), (031), (113), (160), (062) and (160) consistent with the $Pna2_1$ symmetry of $ZnSnN_2$. This discontinuity in the lattice parameters from the wurtzite to orthorhombic phase signals the occurrence of a first order wurtzite to orthorhombic structural phase transition.

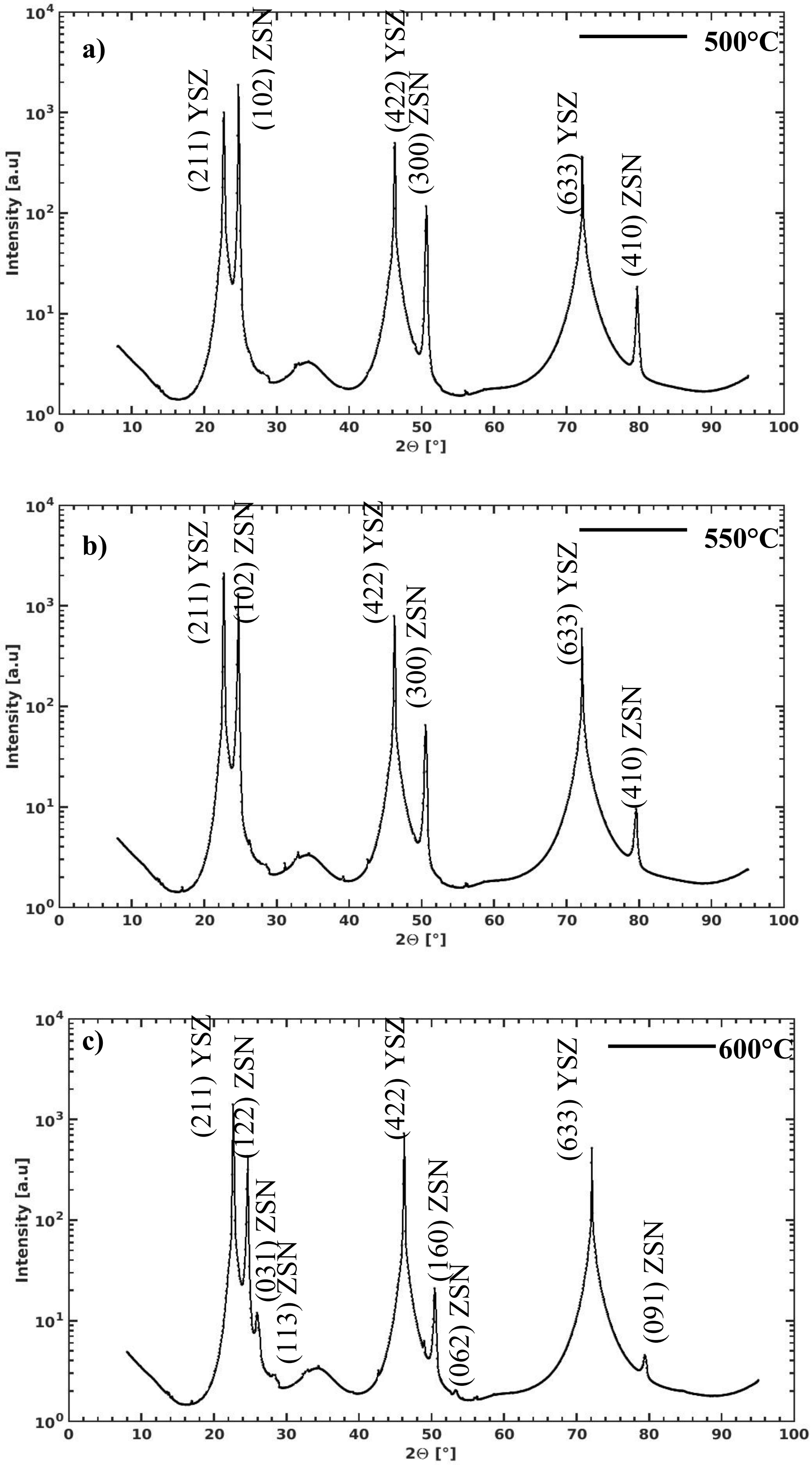

Figure 5.14: θ-2θ measurements of $ZnSnN_2$ films annealed at a) 500°C b)550°C and c) 600°C

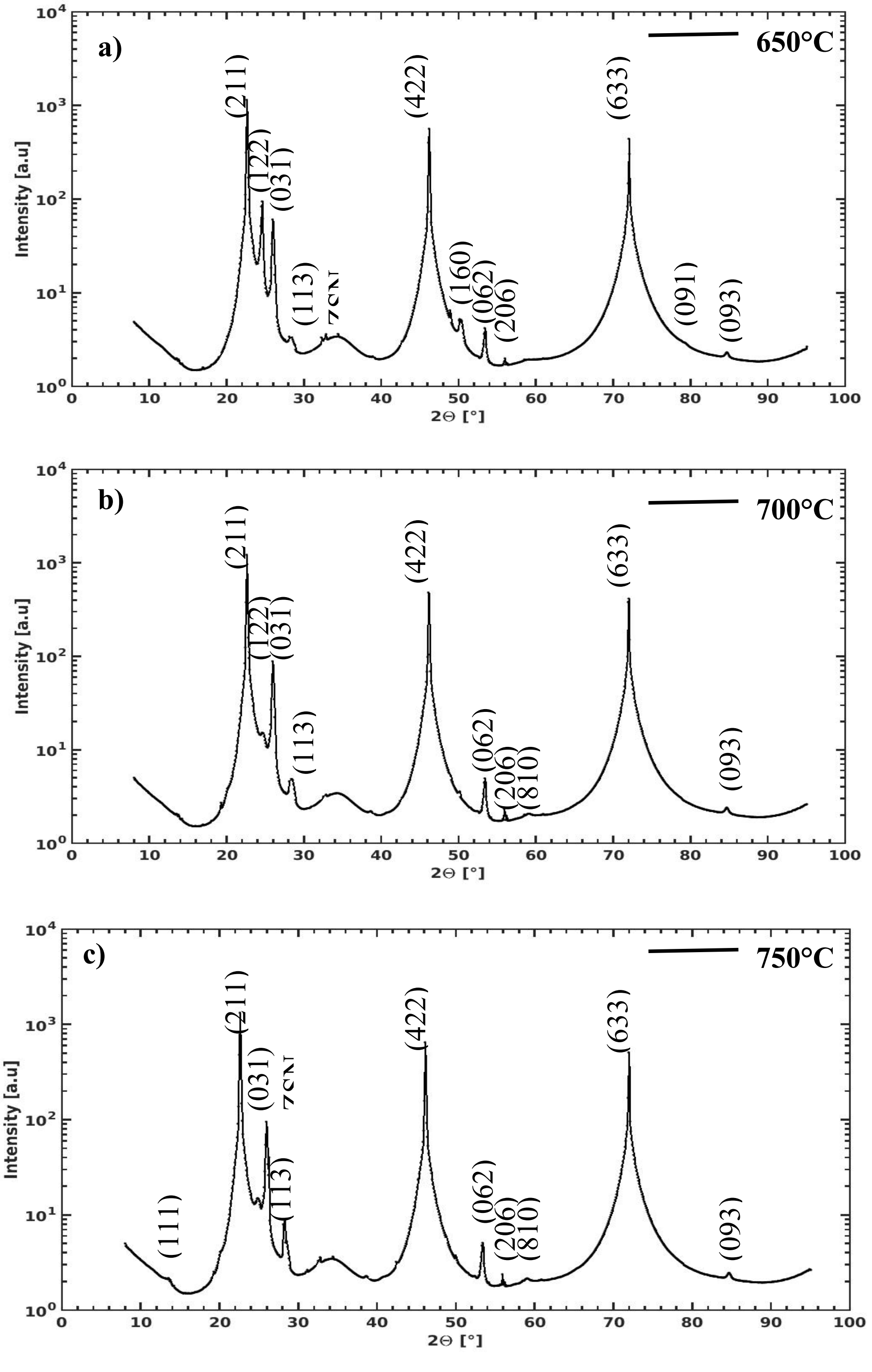

Figure 5.15: θ-2θ measurements of $ZnSnN_2$ films annealed at a) 650°C b)700°C and c) 750°C

The film Bragg peaks were computed using a wurtzite unit cell of a = b = 3.39 Å ± 0.000814, c = 5.472 Å ± 0.000878 and an orthorhombic unit cell of a = 6.78 Å ± 0.000814, b = 5.8715 ± 0.000814 and c = 5.472 Å ± 0.000878. Further annealing of the $ZnSnN_2$ film past the phase transition temperature to 650°C shows a phase pure orthorhombic film in the $Pna2_1$ symmetry. Figure 5.15(a), taken at 650°C shows a clear decrease in intensity of some superstructure reflections, particularly the (122), (160) and the (091) Bragg peaks and the sudden increase in intensity of the (031), (113), (062), (206) and (093) superstructure reflections. This is likely a result of increasing order on the cation sublattice. Heating the $ZnSnN_2$ film further to 700°C as shown in Figure 5.15(b) shows continued decrease in intensity for the (122), (160) and the (091) and increase in intensity for the (031), (113), (062), (206) and (093) super lattice reflections while the (810) film Bragg peak also appears. Figure 5.15(c) shows the θ-2θ measurement at 750°C. While the (031), (113), (062), (206), (093) and (810) reflections show an increase in intensity, the (111) superstructure reflection characteristic of the $Pna2_1$ symmetry of orthorhombic $ZnSnN_2$ emerges.

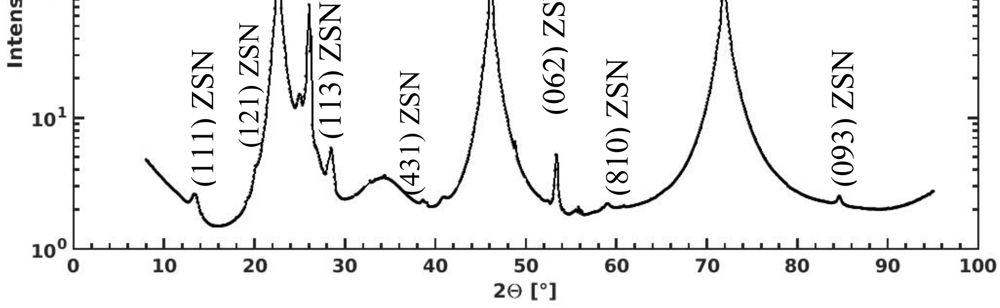

Figure 5.16: θ-2θ measurement of $ZnSnN_2$ film annealed at 800°C

Further annealing to 800°C as shown in Figure 5.16 above indicates an increase in the intensity of the (111) superlattice reflection of the orthorhombic phase and no noticeable change in the intensity of the other superlattice reflections. This likely signifies the completion of ordering on the cation sublattice.

The very distinct changes and continued vanishing of the intensity of superlattice reflections coupled with the emergence of high order superstructure reflections observed in the temperature dependent θ-2θ patterns of $ZnSnN_2$ show that these films undergo a first order phase transition as a function of temperature. These results show that $ZnSnN_2$ films undergo a wurtzite to orthorhombic structural phase transition between 550°C and 600°C that is characterized by systematic ordering on the Zn-Sn cation sublattice.

Post growth annealing studies [14] on polycrystalline $ZnSnN_2$ films grown by reactive radio frequency (RF) magnetron sputtering on c plane sapphire and (0001) GaN substrates, showed a significant decrease in the electron carrier concentration from 10^{21}cm^{-3} to 10^{19} cm^{-3} between 325°C and 450°C. This was attributed to the reduction in the concentration of Zn-Sn anti-sites which are a major reason for the high carrier concentration in $ZnSnN_2$. Annealing studies on the same polycrystalline films also showed a marked increase in mobility, reaching 15.3 cm^{2}V^{-1}s^{-1} at 450°C attributed to improvement in crystallinity. Another study found that annealing reduced electron carrier concentration to as low as 3x10^{16} cm^{-3}. [15] The ability to tune the structure of $ZnSnN_2$ films through annealing hence altering the optoelectronic properties by controlling the amount of disorder on the cation sublattice makes $ZnSnN_2$ an interesting alternative as an earth abundant semiconductor material.

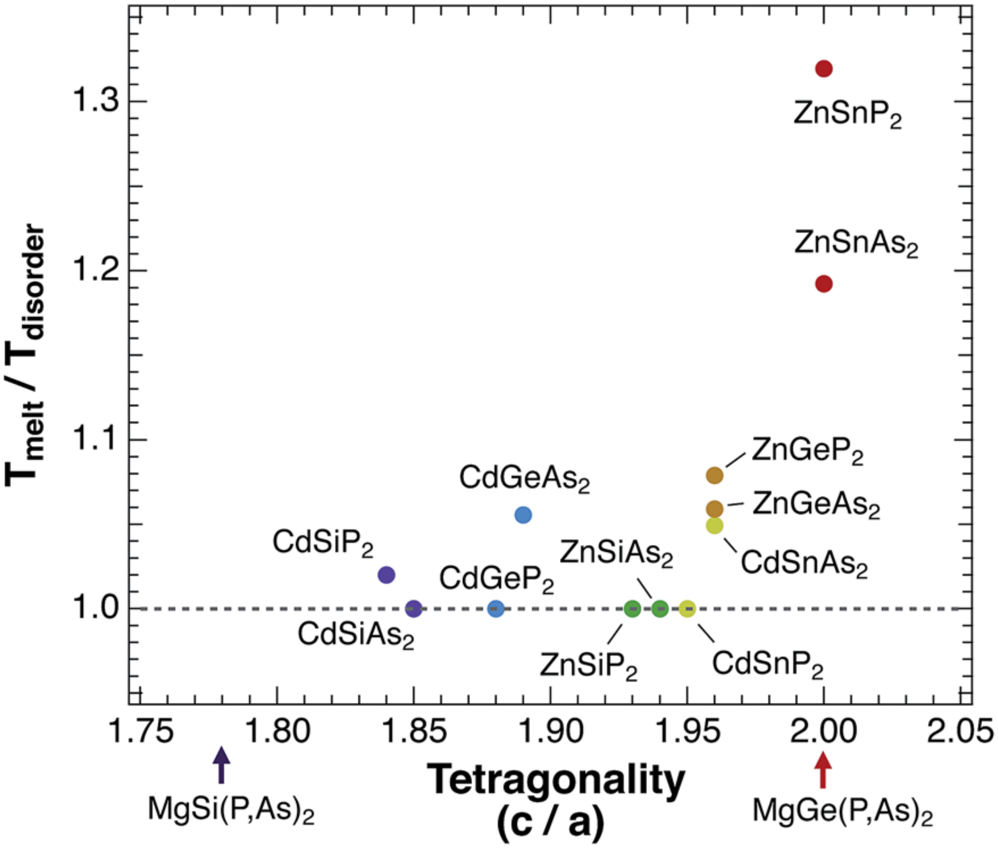

Figure 5.17: Ratio of melting point to disorder transition temperature plotted as a function of tetragonality. Materials with less tetragonal distortion (c/a ~2) more easily form in either the ordered or disordered phase while materials with a large tetragonal distortion (c/a ≪ 2) tend to primarily form as fully ordered structures. Figure reprinted from [18].

The primary determining factor in the tendency of a material to disorder is its tetragonal distortion or (c/a) ratio. [16] Figure 5.17 shows the tendency of a material to disorder as a function of its tetragonal distortion for arsenide and phosphide containing II-IV-V$_2$ materials. Masumoto et.al discovered that the tetragonal distortion varies per the product of the electronegativity difference between the two cations or in our case (Zn, Sn) and the difference in ionic radii of the two cations. [17] Figure 5.17 is reproduced from [18]. Although the data points for the tetragonality of ZnSnN$_2$ films in this work are outside the range plotted, we can still infer some very useful information. In this plot, materials with c/a closest to 2 i.e. (least tetragonal distortion in chalcopyrite materials) have the highest likelihood of a disorder transition temperature below their melting point

($T_{melt}/T_{disorder} > 1$). The melting point of $ZnSnN_2$ is not known with certainty but the $ZnSnN_2$ films in this work have been annealed to 700°C without melting. We have also identified the disorder/order transition temperature for single crystal $ZnSnN_2$ films to be between 550°C and 600°C. Assuming a phase transition temperature of ~ 575°C and a melting point ~ 750°C. ($T_{melt}/T_{disorder} = 1.3$), a value greater than one, meaning that $ZnSnN_2$ films follow a similar trend as the related phosphides and arsenides with an order/disorder transition temperature well below their melting point. This also means that there is a large temperature region between the two transition temperatures; T_{melt} and $T_{disorder}$ in $ZnSnN_2$ films where the order parameter may be controllably varied. Per tetragonal distortion, the $ZnSnN_2$ films in this work have c/a ratios of ~ 1.614, 1.738 for disordered and ordered films indexed in the hexagonal symmetry respectively. The c/a ratio values are within 1.2% and 6.4% of the ideal wurtzite axial ratio for the wurtzite and orthorhombic structure respectively. The c/a ratio of the ordered film is closer to the ideal value for tetragonal distortion in chalcopyrite materials, (2) and far from the ideal c/a ratio in hexagonal structures of 1.633. According to Figure 5.17, it would mean that $ZnSnN_2$ films with c/a close to 1.633 i.e. less tetragonal distortion, can form in either the ordered or disordered phase which is in good agreement with our annealed $ZnSnN_2$ results discussed above which showed wurtzite $ZnSnN_2$ films transform into orthorhombic ordered films without elongation in the c axis. On the other hand, ordered $ZnSnN_2$ films that exhibited large c/a ratios ~ 1.738, 6.4% larger than the ideal c/a ratio in the wurtzite structure tend to form as fully ordered structures. This is also consistent with our findings that show all $ZnSnN_2$ films grown on (111) YSZ with an elongated c axis tend to be ordered.

5.3.5 Characterization of the Orthorhombic Phase of $ZnSnN_2$

Lattice constants obtained for orthorhombic films grown on (111) Yttria stabilized zirconia substrates are given in Table 5.5 indexed in the hexagonal symmetry with the wurtzite domain unit cell parameters in red. All the films exhibited one orthorhombic domain characterized by an elongated c axis and splitting of Bragg peaks and one wurtzite domain. The elongated c axis lattice parameter~ 5.8 Å in the orthorhombic phase is approximately 6.5% larger than the c axis lattice parameter for wurtzite films. We note that the orthorhombic domain in the films discussed below has smaller in plane lattice constants ~ 0.7%, 0.8% and 0.4% compared to the wurtzite domain lattice constants, all within the experimental margin of error. These films were all grown at a substrate temperature of 425°C and Sn and Zn fluxes of $3.72 \text{ X } 10^{13}$ and $2.01 \text{ X } 10^{15}$ atoms/cm^{2}s respectively. Table 5.5 shows the variation in the nitrogen flow rate for the films.

Table 5.5: Lattice constants for orthorhombic (red) and wurtzite (black) domains of $ZnSnN_2$ films indexed in the hexagonal frame of reference

Film	**a (Å)**	**b (Å)**	**c (Å)**	**α (°)**	**β (°)**	**ɣ (°)**
92c	3.362 (3)	3.362(3)	5.841 (3)	90.025(2)	89.98(2)	119.780(2)
92c	3.385(3)	3.382(3)	5.523(3)	89.976(2)	90.019(2)	119.830(2)
95b	3.359(3)	3.357(3)	5.837(3)	90.3250(3)	89.8502(3)	119.995(4)
95b	3.387(3)	3.385(4)	5.453(3)	89.993(5)	90.0606(4)	119.577(4)
90c	3.376(4)	3.373(4)	5.818(3)	89.8226(3)	90.1295(2)	120.250(3)
90c	3.388(5)	3.388(5)	5.478(4)	89.972(4)	89.973(5)	120.257(4)

Interestingly, film 90 which was grown at the highest value of nitrogen flow rate (1.0 sccm) had a heavily c-axis oriented wurtzite domain like the single domain wurtzite phase found in disordered $ZnSnN_2$ films discussed in the previous section. This finding suggests that high nitrogen flux may favor disorder in the cation sublattice.

Table 5.6: Variation in nitrogen flow rate for $ZnSnN_2$ films

Film	Nitrogen Flow rate (sccm)
wpi-90	1.0
wpi-95	0.875
wpi-92	0.5

Figure 5.18 shows a comparison between specular rodscan measurements taken from a single domain wurtzite $ZnSnN_2$ film (91a) and a multi-domain $ZnSnN_2$ film (90c) which was growth at a nitrogen flow rate of 1.0sccm. Figure 5.18(a) shows the multi-domain film- 90c, with a c – axis oriented wurtzite domain with peaks (002), (004) and (006) appearing at wurtzite peak positions as in the single domain phase in disordered $ZnSnN_2$ films grown on (111) YSZ shown in Figure 5.10.

Additional peaks, (110), (011) and (112) in Figure 5.18(a) are orthorhombic peaks consistent with the $Pna2_1$ symmetry of $ZnSnN_2$. We note that the orthorhombic planes are not preferentially

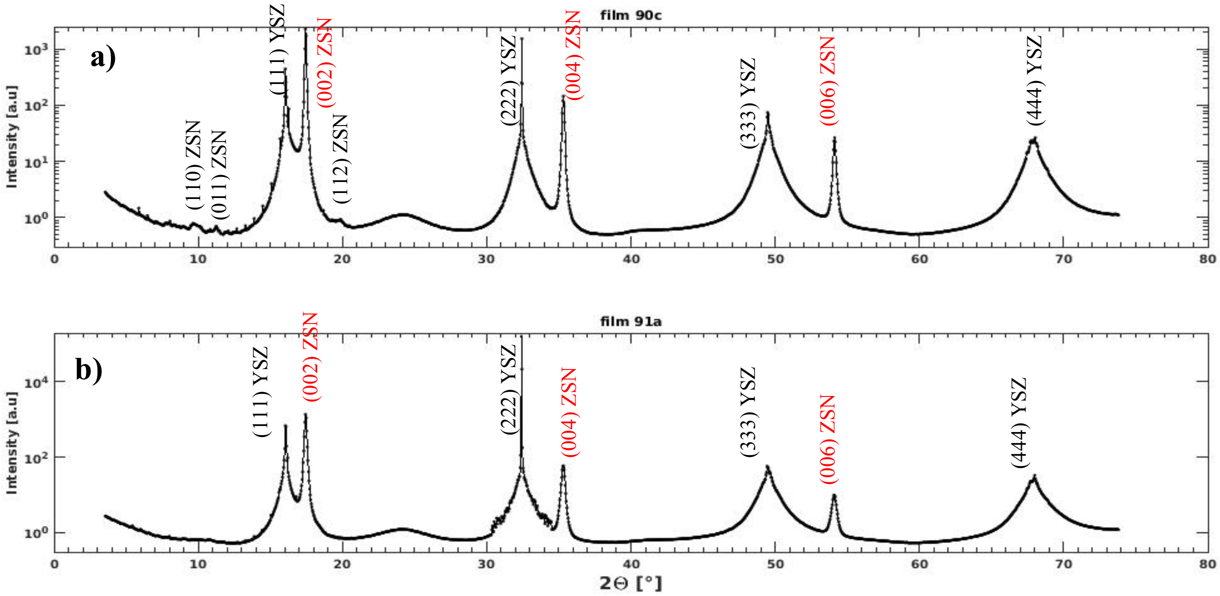

Figure 5.18: Specular rodscan measurement showing evidence of c-axis oriented wurtzite domain in orthorhombic $ZnSnN_2$ film grown at a nitrogen flow rate of 1.0 sccm

ordered in any high symmetry orientation along the c-axis, likely the result of a partially ordered film. This result shows that by varying the nitrogen flow rate, it is possible to tune the order/disorder on the cation sublattice which could have a direct impact on the tuning of the bandgap in these $ZnSnN_2$ films, thus eliminating the need for alloying.

Subsequently, films 95b and 92c that were grown at lower values of nitrogen flow rate; 0.875sccm and 0.5 sccm respectively show a [010]-oriented orthorhombic phase together with the [001] oriented wurtzite phase as seen in film 90c. Overall we did not find a direct correlation between nitrogen flow rate and resulting crystal structure of grown $ZnSnN_2$ films although we must note the difference in intensities of the (00L) Bragg peaks of the wurtzite phase for the various films. Specular diffraction measurements in Figures 5.19(a) and (b) show that the intensity of wurtzite specular Bragg peaks diminishes for films 95b and 92c that were grown at lower values of nitrogen flow rate, 0.875sccm and 0.5 sccm respectively compared to film 90c grown at a nitrogen flow rate of 1.0sccm. Although not theoretically substantiated, this may signal the suppression of disorder at low values of nitrogen flow rate and the subsequent onset of ordering on the cation sublattice. This study shows that nitrogen flow rate may have an impact on the crystal structure of $ZnSnN_2$ films. The [010] oriented orthorhombic domain can also be explained as resulting from the film unit cell being oriented in such a way as to minimize the amount of strain in the material system. The orthorhombic $Pna2_1$ unit cell for the films in this study is a = 6.724(3) Å, b = 5.8229(3) Å and c = 5.841(3) Å. The shortest lattice constant b rotates out of plane so that the two longest lattice constant a and c form the epitaxial relationship with the (111) YSZ substrate. This is a direct result of the doubling of the wurtzite unit cell along the [100] direction and the √3 factor multiplication along the [010] direction needed to form the orthorhombic unit cell of this II-IV nitride material system.

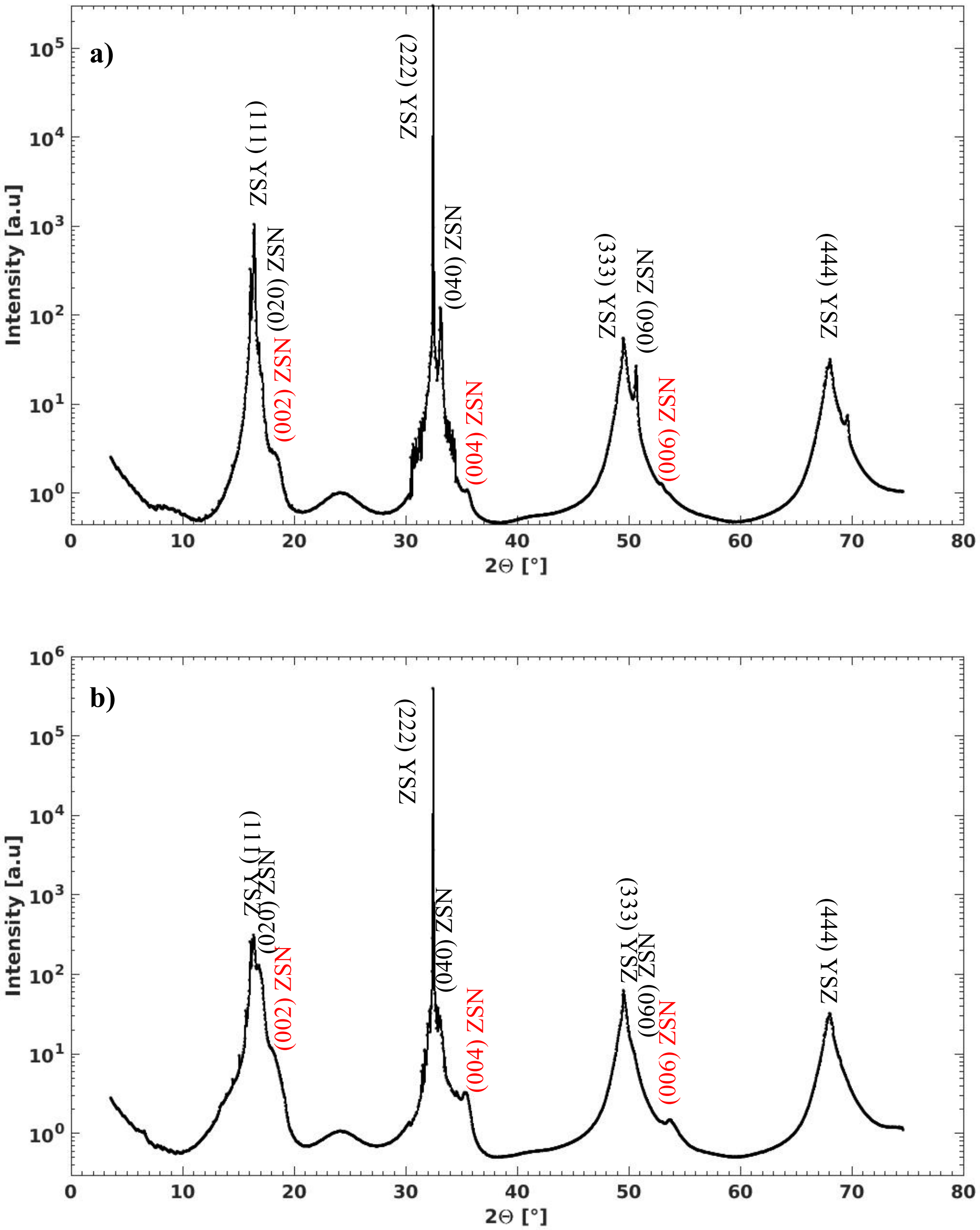

Figure 5.19: Specular rodscan measurement showing [010] oriented orthorhombic phases for $ZnSnN_2$ films a) $ZnSnN_2$ film grown at a nitrogen flow rate of 0.875 sccm b) $ZnSnN_2$ film grown at a nitrogen flow rate of 0.5 sccm

The strain values along the [100] and [010] crystal directions of the orthorhombic unit cell are ~ 8.6% and 8.2% respectively calculated by using $a_o = 2a_w$ and $b_o = a_w \sqrt{3}$ and $c_w = c_o$.

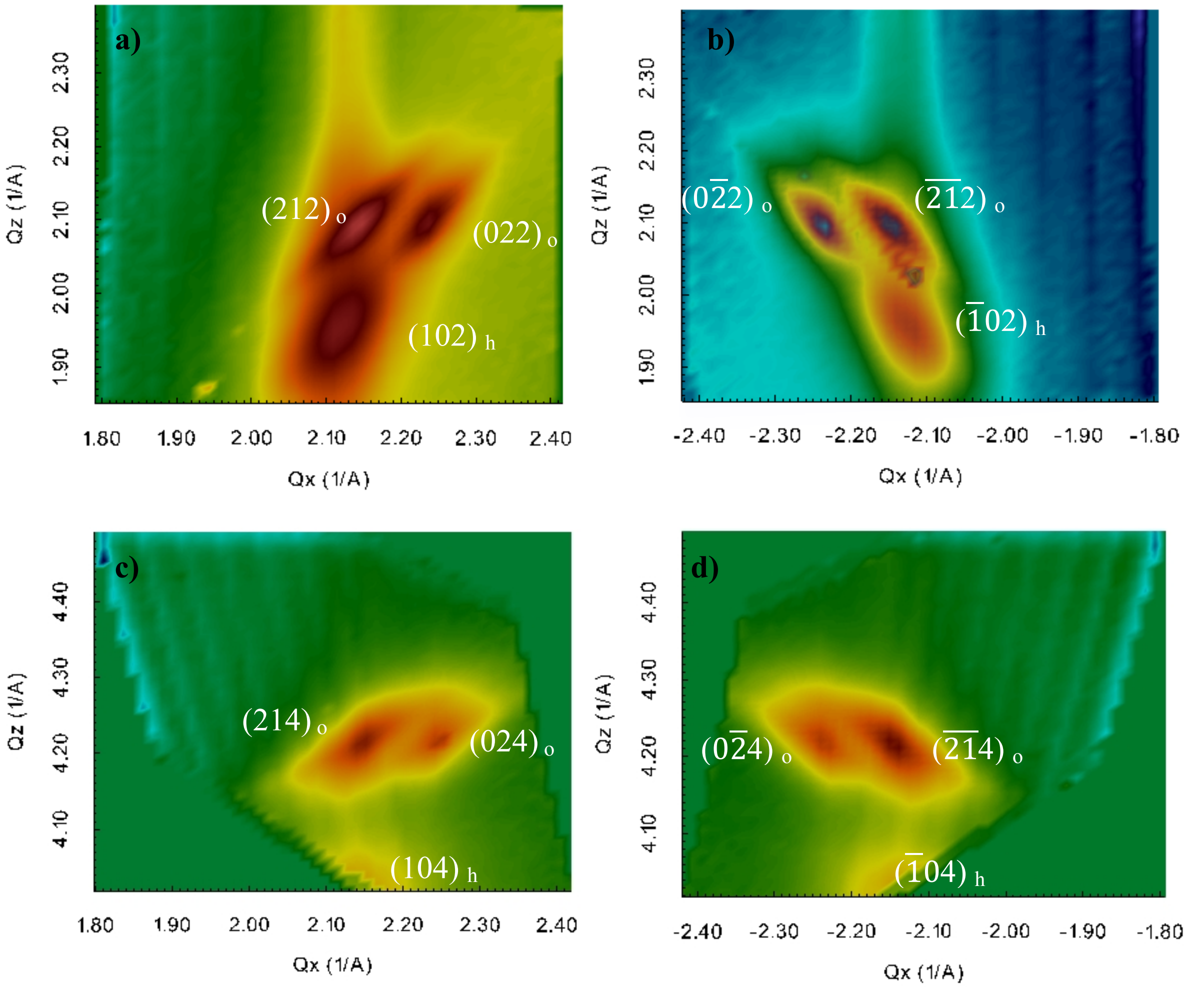

Figure 5.20: RSMs taken around the (212), (022), (214) and (024) orthorhombic peak positions showing symmetry equivalent peaks and the presence of twinning. Orthorhombic peaks are denoted by “o” and hexagonal peaks are denoted by “h”

Figure 5.20(a) – (d) shows 3D reciprocal space maps (3DRSMs) taken around the (212), (214), (022) and (024) split orthorhombic Bragg peak positions showing symmetry equivalent Bragg peaks appearing at the same values of in plane and out of plane momentum transfer vector. The orthorhombic (212) and (022) Bragg peaks are split at the hexagonal (102) Bragg peak position. The hexagonal (102) Bragg peak shown in Figure 5.20(a) and (b) is for the wurtzite domain present in the film. The orthorhombic and wurtzite domains are oriented 180° with respect to each other and have dissimilar values of out of plane momentum transfer Q_T owing to the difference in out of plane lattice constant c. This shows the obvious difference between the two crystal structures. Figure 5.20 (c) and (d) shows an increase in separation between the orthorhombic phase Bragg peaks (022) and (212) and the wurtzite phase (102) peak together with their symmetry equivalents along the out of plane direction at higher $Q_{z.}$ This is the result of twinning likely induced by the substrate.

5.4 Transmission Electron Microscopy Measurements

Characterization of the domain structure of wurtzite and orthorhombic $ZnSnN_2$ films was performed by transmission electron microscopy (TEM) using a JEOL 3011 and JEOL. Samples were mechanically polished and then subjected to argon ion milling before taking the TEM and electron diffraction measurements. Figure 5.21 (a) shows the high resolution TEM micrographs for single domain wurtzite $ZnSnN_2$ film grown on (111) Yttria stabilized zirconia.

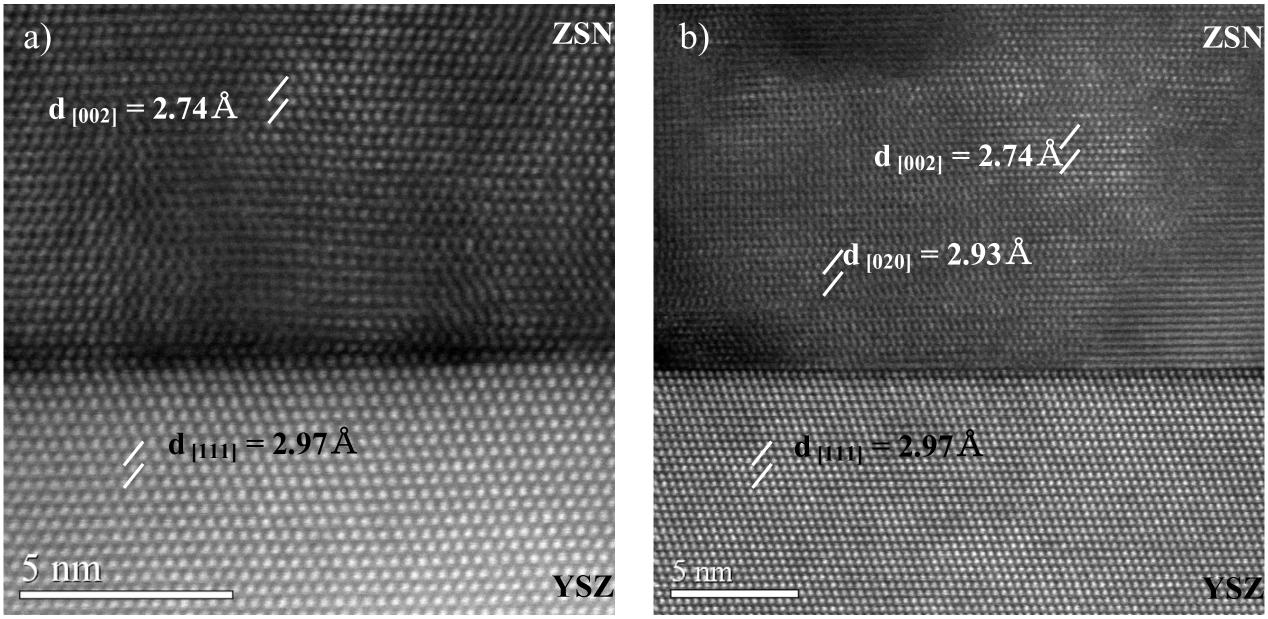

Figure 5.21: TEM micrographs for a) wurtzite and b) orthorhombic-wurtzite $ZnSnN_2$ film grown on (111) Yttria stabilized zirconia

Per the TEM micrograph, the atomic d-spacing in the film was calculated to be 2.74 Å which corresponds to the d-spacing of the wurtzite (002) plane. The [002] $_{ZSN}$ and [111] $_{YSZ}$ interface shows a good epitaxial relationship between the film and the substrate with noticeable defects in the atomic planes close to the interface. These defects are expected due to the large tensile strain the film is under ~ 8%. Figure 5.21 (b) on the other hand shows the high resolution TEM micrograph for a multi domain $ZnSnN_2$ film having both the orthorhombic and wurtzite phases. Note that the orthorhombic and wurtzite phases in this film are both single crystal and calculations of the d-spacing yielded values of 2.74 Å and 2.93 Å for the wurtzite [002] plane and orthorhombic [020] plane respectively. The orthorhombic phase is [010] oriented with respect to [111] YSZ while the wurtzite phase is [001] oriented as confirmed by θ-2θ measurements in the previous section. The multi domain nature of the film is also obvious from the different contrasts in the TEM micrograph. The orthorhombic and wurtzite domains are oriented 180° with respect to each other.

5.5 Discussion

We have characterized using synchrotron x-ray diffraction techniques, thin films of stoichiometric $ZnSnN_2$ grown on (111) Yttria stabilized zirconia and (001) lithium gallate substrates that exhibit both the disordered wurtzite phase and the predicted $Pna2_1$ wurtzite-derived orthorhombic crystal structure. The unit cell refinement measurements for both the orthorhombic and wurtzite films are in good agreement with both theoretically calculated structures and experimentally determined lattice constants for polycrystalline films in related work on $ZnSnN_2$. We find that the wurtzite films have preferential [001] orientation and single crystal, growing with the [001] $ZnSnN_2$ // [111] YSZ and the orthorhombic films have preferential [010] orientation to (111) YSZ. Films grown on LGO exhibit the orthorhombic $Pn2_1a$ crystal structure, a consequence of being grown on $Pn2_1a$

symmetric substrates. While the orthorhombic films grown on YSZ have multiple domains and in some cases a wurtzite domain, RHEED patterns show the formation of single crystal films as do electron diffraction measurements. Through a controlled variation of molecular beam epitaxy growth conditions, we find that higher substrate temperatures ~ 550°C and low nitrogen flow rate favor orthorhombic film growth and likely ordering on the cation sublattice. Rapid thermal annealing studies showed a structural phase transition from the wurtzite phase to the orthorhombic phase between 550°C and 600°C accompanied by the appearance of orthorhombic superstructure reflections in the θ-2θ diffraction spectrum. This study suggests that annealing can be used to control disorder on the cation sublattice and has a direct impact on bandgap tuning in $ZnSnN_2$ films since theoretically, the bandgap has been shown to vary from 1.0eV in wurtzite films to about 1.8eV in orthorhombic films. The abrupt change in the diffraction spectrum from the wurtzite crystal structure to the orthorhombic $Pna2_1$ structure at the transition temperature, suggests that this phase transition is first order in nature. This annealing treatment study has direct consequences on the carrier concentration, mobility and electrical resistivity in single crystal $ZnSnN_2$ films that would likely result in improved material properties in the ordered orthorhombic films compared to the disordered wurtzite films as shown in related work on polycrystalline films.

Bibliography

[1] Stabilization of orthorhombic phase in single-crystal $ZnSnN_2$ films, Nancy Senabulya, Nathaniel Feldberg, Robert. A. Makin, Yongsoo Yang, Guangsha Shi, Christina M. Jones, Emmanouil Kioupakis, James Mathis, Roy Clarke, and Steven M. Durbin, AIP Advances 6, 075019 (2016); doi: 10.1063/1.4960109

[2] P. Kraft, A. Bergamaschi, C. Broennimann, R. Dinapoli, E. F. Eikenberry, B. Henrich, I. Johnson, A. Mozzanica, C. M.Schleputz, P. R. Willmott, and B. Schmitt, J. Synchrotron Radiat. 16, 368 (2009).

[3] C. M. Schlepütz, R. Herger, P. R. Willmott, B. D. Patterson, O. Bunk, C. Bronnimann, B. Henrich, G. Hülsen, and E. F. Eikenberry, Acta Cryst. A 61, 418 (2005).

[4] C. M. Schlepütz, S. O. Mariager, S. A. Pauli, R. Feidenhans'l, and P. R. Willmott, J. Appl. Crystallogr. 44, 73 (2011).

[5] Paul C. Quayle, Keliang He, Jie Shan, and Kathleen Kash, "Synthesis, lattice structure, and band gap of $ZnSnN_2$," MRS Communications 3, 135–138 (2013, doi:10.1557/mrc.2013.19.

[6] G. Kresse and D. Joubert, "From ultrasoft pseudopotentials to the projector augmented-wave method," Physical Review B 59, 1758–1775 (1999).

[7] G. Kresse and J. Furthmüller, "Efficient iterative schemes for ab initio total-energy calculations using a plane-wave basis set," Physical Review B 54, 11169–11186 (1996).

[8] J. Perdew, K. Burke, and M. Ernzerhof, "Generalized Gradient Approximation Made Simple," Physical Review Letters 77, 3865 (1996).

[9] Punya et al., Phys. Rev. B 84, 165204 (2011).

[10] Feldberg, N., et al., Growth, disorder, and physical properties of $ZnSnN_2$. Applied Physics Letters, 2013. 103(4): p. 042109.

[11] Paul C. Quayle, Keliang He, Jie Shan, and Kathleen Kash, "Synthesis, lattice structure, and band gap of $ZnSnN_2$," MRS Communications 3, 135–138 (2013, doi:10.1557/mrc.2013.19.

[12] S. Francoeur, G. A. Seryogin, S. A. Nikishin, and H. Temkin, Appl. Phys. Lett. 76, 2017 (2000).

[13] Nathaniel Feldberg, $ZnSnN_2$: Growth and Characterization of An Earth Abundant Element Material with Order Dependent Properties, PhD thesis, UMI 3714590 Published by ProQuest LLC (2015).

[14] Korlam Sudheer, Deposition and Characterization of Post-growth annealed $ZnSnN_2$ thin films, PhD thesis, UCLA electronic theses and dissertations, http://escholarship.org/uc/item/7389f2kg

[15] A. N. Fioretti, E. S. Toberer, A. Zakutayev and A. C. Tamboli, 42nd IEEE Photovoltaic Specialist Conference (PVSC), 2015, pp. 1–5.

[16] S. Nakatsuka and Y. Nose, J. Phys. Chem. C, 2016, 121(2), 1040–1046.

[17] K. Masumoto, S. Isomura and W. Goto, J. Phys. Chem. Solids, 1966, 27, 1939–1947.

[18] Martinez et. al Synthesis, structure, and optoelectronic properties of II–IV–V2 materials, Journal of Materials Chemistry A, DOI: 10.1039/c7ta00406k

CHAPTER VI

Conclusions and Outlook

The work presented here provides an understanding of the structural properties of single crystal $ZnSnN_2$ films that have only recently been synthesized via molecular beam epitaxy in collaboration with Professor Durbin's group at Western Michigan University. A major new finding presented in this dissertation is the observation of a novel structural phase transition between the hexagonal (wurtzite) and orthorhombic structural form of $ZnSnN_2$ as a function of thermal annealing. The significance of this result is that the observation of a structural phase transition reveals its origin to be related to ordering of the heterovalent cations (Zn and Sn). Moreover, the ordering of the system due to annealing is consistent with the results of Density Functional Theory showing that the ordered structure is the lowest energy phase of this system. We have shown that this lowest energy state can be achieved via thermal annealing. This is the first time that this connection between ordering and a structural transition has been demonstrated.

Although some major strides have been made in this work, such as demonstrated synthesis and characterization of $ZnSnN_2$ in both the predicted wurtzite and orthorhombic phases and tuning of cation sublattice disorder through annealing, there are still many aspects of semiconducting properties and device design that need to be considered for $ZnSnN_2$ and related earth abundant materials. The growth of $ZnSnN_2$ on lattice matched substrates like LGO and YSZ and the systematic control of the growth parameter space in MBE has gone a long way in improving the crystal structure of these films and continued exploration of the cation sublattice ordering phenomenon. Our x-ray measurements for example, suggest that the cation arrangement in the measured wurtzite films, is consistent with the disorder due to random placement of Zn and Sn atoms on the cation sublattice, rather than the disorder arrangement proposed by Quayle et al. characterized by stacking of alternating layers of $Pna2_1$ and $Pmc2_1$ polytypes. These findings suggest that the disorder phenomenon in $ZnSnN_2$ needs to be further investigated. In the ordered orthorhombic films, only the $Pna2_1$ ordering has so far been experimentally verified.

Future work on this material is warranted and much needed. Since the annealing study in this work has shown a structural phase transition from the wurtzite to orthorhombic phase, Hall measurements on annealed $ZnSnN_2$ films are needed to understand the influence of annealing treatment on single crystal films as it relates to electron concentration, mobility and electrical resistivity. Additional steps need to be taken towards lowering the free electron concentration. This could be achieved through growing at high temperature or exploration of bulk $ZnSnN_2$ films to reduce threading dislocations that arise in epitaxial systems. Theoretical and experimental work on Zn (Sn, Ge) N_2 alloys has shown that bandgap tunability in these II-IV nitrides is possible without the occurrence of a miscibility gap. This may enable functionality such as red and green emitters and multijunction solar cells. Enabling these future applications requires that additional work be invested in understanding doping, band offsets and carrier concentration in alloys to move towards device integration. Growing $ZnSnN_2$ on zinc oxide substrates is worth considering though expected to be expensive. ZnO is rapidly declining in price and it would mean that the entire device including substrate would be non-toxic and earth abundant and hence easily recyclable.

The single crystal films investigated in this study were synthesized via molecular beam epitaxy and while MBE offers many benefits for research purposes, commercial scalability for PV applications is limited. The growth rate for nitride MBE for example is less than 10nm per hour making it less attractive for scalability. Although the corporate sector uses MBE, it is generally for smaller devices such as chips, whose potential value per cm^2 is relatively high. PV applications, require much lower production cost. For this reason, investigation into other growth techniques and growth optimization may be warranted once the viability of $ZnSnN_2$ films in devices has been demonstrated. The ability to grow $ZnSnN_2$ films at relatively low growth temperature offers a hint that there might be value in investigating the use of printing methods currently being used for PV and flexible solid-state systems. Sputter deposition for example is the most industrially scalable method and best suited for Zn-IV nitride growth due to the ability of these materials to tolerate microstructural defects due to ionic bonding.

In conclusion, the work presented here suggests that $ZnSnN_2$ has tremendous potential as an earth abundant semiconductor material to be used as an absorber layer in solar cells and other optoelectronic device applications with tunable wavelength. Further work to develop controlled n and p-type doping in $ZnSnN_2$ films is required to truly realize the potential of this material plus integration of $ZnSnN_2$ films into heterostructures and devices.